eman ta zabal zazu

Universidad del País Vasco
Euskal Herriko Unibertsitatea

Department of Material Physics

Charge and spin transport in graphene devices

Luca Pietrobon

Supervised by
Dr. Luis E. Hueso

June 2015


CIC
nanoGUNE
nanoscience cooperative research center

Contents

Part I

Graphene and Experimental techniques: an introduction

1

Graphene and its electric transport properties

Graphene is the thinnest (and yet, among the strongest) material known. It consists of "a flat monolayer of carbon atoms tightly packed into a two-dimensional (2D) honeycomb lattice, as sketched in Figure 1.1.

This remarkable material currently holds record high characteristics in a variety of physical measures, from room temperature electrical mobilities (2.5×10^5 $cm^2V^{-1}s^{-1}$) [1] to intrinsic strength (130 GPa) [2], from exceptional impermeability to gasses [3] to record high thermal conductivity κ (~2000 to 5300 W m^{-1} K^{-1}) [4].

Graphene is only one of the ways carbon can crystallize in nature: this exceptional collection of allotropes spans from 0D to 3D structures, from quantum-behaving particles to the more familiar graphite in our pencils.

1.1 Carbon in nature: graphene's allotropes

Carbon is among the most abundant elements on Earth. It is the sixth entry in the periodic table with the electronic configuration $1s^2\,2s^2\,2p^2$, thus allowing for 4 valence electrons. In carbon structures, *s*- and *p*-orbitals will typically hybridize (sp, sp^2 or sp^3 configurations) and realize strong covalent bonds between atoms, allowing for a number of stable configurations in different di-

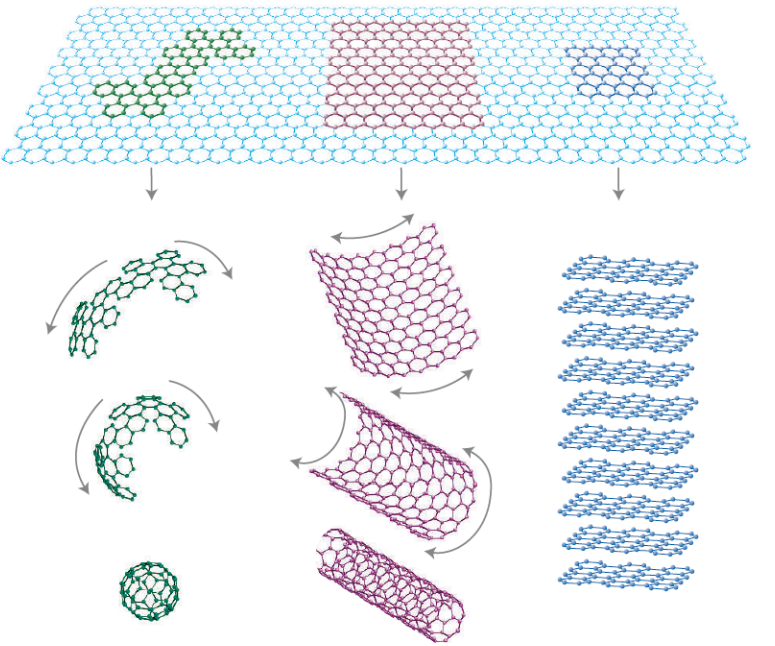

Figure 1.1: Graphene is a 2D crystal structure made entirely of carbon. Atoms are arranged in a honeycomb lattice, with an interatomic distance of 1.42 Å (top). Different ways of folding or stacking the graphene sheet lead to different carbon structures, such as buckyballs, carbon nanotubes or graphite. Image adapted from [5].

mensionalities. Such a versatility, resulting in the series of carbon allotropes, is unique to this element.

3D: Diamond and graphite

The most famous carbon structure is diamond, one of the 3D allotropes of graphene, together with graphite. On the atomic scale, diamond differs from graphite for its sp^3 hybridized orbitals, which bond the ions in a rigid crystal structure and give diamond its exceptional hardness and chemical stability.

Graphite, on the other hand, is made of the stacking of individual monolayers of carbon, with an inter-planar distance of about 3.35 Å (see Figure 1.2). Van der Waals forces keep the layers together: as these forces are relatively week ones, the layers can be easily mechanically separated (for instance, by the simple handwriting while using a pencil).

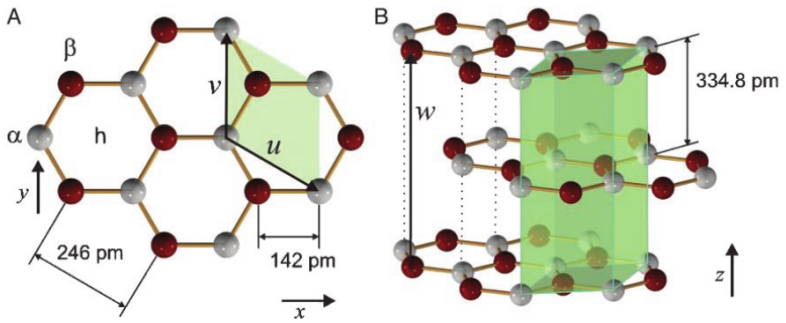

Figure 1.2: Crystal structure of graphite, top view to the left and 3D layered structure to the right. The unit cell is highlighted in green. Image adapted from [6].

2D: Graphene and nanoribbons

Isolating a single monolayer of graphite is one of the ways to obtain graphene, which may be thought as a planar, honeycomb arrangement of carbon atoms. There are several ways to obtain this 2D structure, the ost common ones probably being mechanical cleavage [7], epitaxial growth [8], liquid exfoliation [9,10] and chemical vapor deposition (CVD) [11].

Interestingly enough, graphene was not expected to exist at all. On the theoretical side, long range crystalline order in 2-dimensions had been ruled out by invoking the Mermin-Wagner theorem [12], therefore concluding that a crystalline system like graphene would not be a stable one. In addition, experimentally "it remained unclear whether free-standing atomic layers could exist in principle [thin films become thermodynamically unstable (decompose or segregate) below a certain thickness, typically, of many dozens layers]" [13]. Once free-standing single layer graphene had actually been isolated and characterized, the debate grew in the literature on what mechanisms allowed graphene to bend Mermin's severe rule. Eventually graphene was shown to *ripple* [14], therefore not being exactly planar[1]. Although not atomically flat, graphene has been shown now to be stable both when supported by some other material (e.g. silicon dioxide) and when suspended. Electrically, graphene is a gap-less semimetal, with a linear dispersion relation for low charge carrier densities.

Graphene nanoribbons (GNR) are a similar 2-dimensional carbon allotrope and may be thought as "thin stripes" of graphene. The width of these stripes and the particular shape of their edges (zig-zag or armchair) have shown to play a significant role in tuning graphene's electrical properties, in some cases even opening a band-gap [15].

1D: Carbon nanotubes

Nanotubes are easily pictured as the rolling up of a graphene sheet into a tube. Exceptional features of this material span mechanical, thermal and electronic properties: as an example, they can reach length to width ratio of 10^8 and they range from metallic to semiconductor depending on the particular way they are rolled up (*chirality*) with respect to the lattice vectors. Their cylindrical symmetry makes them a truly periodic system around the axis of symmetry: the only possible steady-state wave functions in the transverse plane are standing waves, leaving only the axial direction as a possible direction of propagation. Curiously, nanotubes were experimentally realized and investigated well before graphene [16].

[1] Moreover, the Mermin-Wagner theorem questions *perfect* periodicity on an *infinite* 2D systems: one could argue whether this applies to a graphene flake, but this goes well beyond the scope of this work.

0D: Buckyballs

The family of carbon structures reaches 0D with the buckyballs, the closest-to-spherical arrangement for this series of allotropes. It is a molecule of 60 carbon atoms with a diameter of $\approx$ 1 nm. Among the most interesting experiments done with these "huge" objects is certainly the one reported in [17], where wave-particle duality is observed despite the large dimensions of these objects, which allows the authors to investigate further the physics of decoherence.

1.2 Obtaining an atomic sheet of carbon

Several methods have been developed for graphene production, from mechanical to chemical to epitaxial ones. We will briefly overview the most common ones by summarizing the contents relevant to us from [18], focusing primarily on three techniques (mechanical exfoliation, chemical vapor deposition and epitaxial growth) and briefly introducing other emerging ones. We will use the electrical mobility as our primary figure of merit for electronic performance (as it is typically done in the literature). Other relevant ones - at least at this general level - are the typical lateral dimensions of graphene films attainable and the production costs that each technique implies.

Graphene by exfoliation

Graphene is made to date in quite a number of different ways, the simplest one being mechanical exfoliation: in fact, separating graphite's atomic layers from one another is as easy as writing with a pencil. To improve the size and the yield of single layer flakes, the technique is usually slightly more elaborate and involves exfoliating graphene with adhesive tape from natural graphite or Highly Ordered Pyrolytic Graphite (HOPG). Graphite and graphene flakes are then typically transferred to a SiO_2 wafer by laying the tape over the oxide. This method, typically referred to as *micromechanical cleavage/exfoliation*, often yields ~100 µm × 10 µm single layer graphene flakes randomly distributed on a SiO_2 substrate (typically $\gtrsim$ 25 mm^2 area): easy to make, impossible to find by means of serial measurements, *e.g.* AFM. The reason the typical substrate for exfoliated graphene is a 90 or 300 nm SiO_2 is the (small) optical contrast that graphene shows when placed over it, making the atomically thin flake slightly

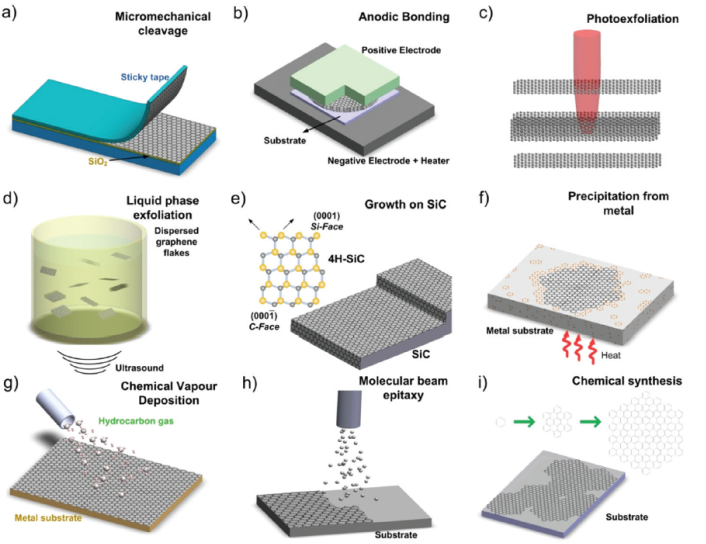

Figure 1.3: Schematic illustration of the main experimental setups for graphene production. (a) Micromechanical cleavage (b) Anodic bonding (c) Photoexfoliation. (d) Liquid phase exfoliation. (e) Growth from SiC. (f) Precipitation from carbon containing metal substrate. (g) CVD process. (h) Molecular beam epitaxy. Different carbon sources and substrates (i.e. SiC, Si, etc.) can be exploited. (i) Chemical synthesis using benzene as building blocks. Adapted from [19].

less then invisible. Optical scan of the SiO_2 becomes then a (tedious, but) viable possibility for locating graphene [13]. More recently, polymers have been used instead of the adhesive tape, along with Atomic Force Microscopy and Scanning Tunnelling Microscopy techniques, to exfoliate and manipulate the individual flakes.

To date, this is still the method delivering samples with the highest mobilities. Values up to ~20 000 $cm^2V^{-1}s^{-1}$ have been measured in as-prepared single layer graphene (SLG) devices [20] at room temperatures, with exceptional performances up to 10^6 $cm^2V^{-1}s^{-1}$ on suspended, current-annealed samples [21,22] and 10^7 $cm^2V^{-1}s^{-1}$ for de-coupled SLG on the surface of bulk graphite [23]. Encapsulating SLG in hexagonal boron nitride (h-BN) has also proved to be a very successful strategy, yielding mobilities $>10^5$ $cm^2V^{-1}s^{-1}$ [1].

There are similar methods for the production of graphene flakes that take advantage of non-mechanical forces, such as *anodic bonding* [24,25]. Graphite is first pressed onto a glass substrate and a high voltage of few KVs (0.5–2 kV) is applied between it and a metal back contact to promote the electrostatic adhesion of few layer graphene flakes to the glass [24,25]. *Photoexfoliation* is a technique where a laser beam induces the compleate or partial detachment of a graphene layer from a graphite surface. Tuning the energy density permits the accurate patterning of graphene [26], and it is best implemented in inert or vacuum conditions [27,28]. However, this is still a method in its infancy [26,29] and needs further development.

Graphite can also be exfoliated in liquid environments exploiting ultrasounds to extract individual layers, either in aqueous [30–33] or non-aqueous solvents [9,10,32,34–36]. A "purification" step follows the ultrasonication in order to isolate the thinnest flakes, typically through centrifugation [37]. Flakes are typically limited in size ($\lesssim$1 μm^2) [9,30–32,35,36,38], but highly relevant to for industrial applications such as graphene inks, where mobilities ~90 $cm^2V^{-1}s^{-1}$ have been demonstrated [36].

In spite of the abundance of options, the methods relying on exfoliation are ultimately sharing a common line: they are all a very low on production costs and yield small flakes, randomly localized over a substrate surface, which need to be tackled individually. For a scalable production of large, single layer graphene samples we have to turn to other methods.

Graphene by epitaxial growth

Almost perfect crystal structures can be obtained by exfoliation, but there is a need for a more scalable system that would allow, for instance, to grow graphene over a substrate. One possible approach consists in epitaxial growth of graphene on SiC: by heating the material to temperatures >1100 °C in ultra high vacuum [8,39,40], the Si sublimates and graphitization occurs on both the Si- and the C-terminated surface [41,42]. This method, generally referred to as epitaxial growth, was reported as early as 1896 [43] for the production of graphite for lubricant applications. However, this is not a self-limiting process and careful optimization must be considered in order to obtain SLG. The carbon rich layer obtained can be decoupled from the Si-face by hydrogen intercalation [44] becoming a quasi-free-standing SLG with typical linear π bands [44], in contrast to the interaction between the graphene and the C-face, which is much weaker [45].

Typically the larger graphene domains are produced on the C-face (~200 nm, multilayered, rotationally disordered) [46,47]. On the Si-face, relatively high graphitization rates [48] typically lead to small domains (~30–100 nm [47]). Different strategies have been proposed to control the speed of the process, including using Ar in a furnace at near ambient pressure (1 bar) to reduce the Si sublimation rate [8]. In this case, temperature needs to rise above 1500 °C [8], enhancing surface diffusion, with complete surface restructuring before graphene formation and achievement of ~50 μm domains [8].

To date, graphene grown on the Si-face has a room temperature mobility up to ~500–2000 $cm^2V^{-1}s^{-1}$ [48], with higher values on the C-face (~10 000–30 000 $cm^2V^{-1}s^{-1}$) [46,48,49].

Exceptionally high values have recently been reported for a 40-nanometre-wide GNR grown on the Si-face, with ballistic conductance (at 4 K) on a length scale >10 μm and a mobility of 6×10^6 $cm^2V^{-1}s^{-1}$ [50]. A final remark making this technique attractive is the possibility of shaping the graphene devices without need of etching methods: electron beam lithography can be done on the SiC before graphene growth, resulting in the production of etching-free graphene ribbons.

This technology has benefited from the familiarity of the electronics industry with SiC, and wafer-scale production of transistors has been reported [51,52] and graphene on SiC has been developed as a resistance standard based on the

Quantum Hall Effect [53–56]. The drawback here is typically the cost of the SiC material, and attempts to lower the costs are currently being optimized [57]. Ultimately, the transfer of SLG from a SiC surface to a target substrate is still an open point, where the difficulty arises from the strong binding of graphene to the SiC surface [45,48,49].

Graphene by precipitation

In the chemical vapor deposition (CVD) method, carbon atoms are precipitated on to a substrate, for instance Ni [58] or Cu [59]. The metal is exposed to a hydrocarbon gas at high temperatures (typically 800-1000 °C, which catalyzes on the (cooled) substrate and the number of atomic layers grown varies with the reaction parameters.

CVD is only one of a larger family of methods for growing carbon by precipitation, which includes flash evaporation, physical vapour deposition (PVD), and spin coating. The carbon source can be a solid [60,61], liquid [62–64] or gaseous [65]. Flash evaporation [66] and PVD can be used when the source is pure carbon directly on the substrate of interest. Polymers can be spun on a metal substrate at RT, followed by high temperature annealing and growth [61] and finally segregation from carbon-containing metal or inorganic substrates can also yield graphene layers [67,68].

CVD is a widely used method in the semiconductor industry [69]. Different types of CVD processes have been developed (*e.g.* thermal, plasma enhanced (PECVD), cold wall, hot wall, reactive), the thermal CVD on metals being the oldest [65] and our reference one for this work. The first CVD growth of uniform, large area (~cm^2) graphene on a metal surface was reported in 2009 by Li and coworkers [11] on Cu foils, in a self-limited[2] process [11,70]. Following, large grain (~20–500 µm) graphene grown on Cu and transferred to a SiO_2 substrate was reported, showing mobilities ranging from ~16 400 to ~25 000 $cm^2V^{-1}s^{-1}$ at room temperature [71] and from ~27 000 to ~45 000 $cm^2V^{-1}s^{-1}$ on h-BN at 1.6 K [72].

The growth process starts from the decomposition of hydrocarbons generating carbon atoms, which nucleate on Cu. The nuclei density is principally a

[2] Almost self limited, as about 5% of the area will typically be covered with bi-layer and tri-layer graphene [11,70].

function of temperature and pressure, and from these initial seeds large domains are eventually formed [71,73], up to ~1 cm [74] under appropriate conditions. However, when the Cu surface is fully covered, the films become polycrystalline, since the nuclei are are mis-oriented or incommensurate with respect to each other, even on the same Cu grain [11,73,75,76]. Current efforts are being taken to suppress the nucleation density by Cu pre-treatments, electrochemical polishing [77,78] and highpressure annealing [76].

Some difficult issues arise when growing graphene on most metal substrates due to the difference in thermal expansion coefficient between the later one and graphene [79], resulting in significant wrinkle density upon cooling [70]. These wrinkles may cause significant device degradation through defect scattering, similarly to the detrimental effect grain boundaries have on mobility in semiconducting materials [71]. Finally, CVD growth can also be achieved at lower temperatures on Ni(111) (500-600 °C [80]),Fe (650 °C [81], mobility ~100 $cm^2V^{-1}s^{-1}$) and Cu foils (300 °C using a benzene precursor [82], mobility ~100 $cm^2V^{-1}s^{-1}$) .

Several attempts have been made to grow CVD graphene on SiC [83], sapphire [84] and Si_3N_4/Si [85] as well as on metal oxides such as MgO [86] and ZrO_2 [87], since graphene growth on insulating substrates would be ideal for electronics. However the best performances achieved are limited to mobilities $\lesssim$10 000 $cm^2V^{-1}s^{-1}$ (2K [84]). Far higher quality can be achieved by CVD growth over h-BN [88–90], an atomically smooth substrate with few dangling bonds and charge traps [91].

Ordinary CVD-grown graphene samples generally show mobilities up to the order of 10^3 $cm^2V^{-1}s^{-1}$, a lower quality than what has proven to be achievable with exfoliated or epitaxial graphene. On the other hand, this approach is definitely a scalable, less expensive one that could use quite a large pool of sources for carbon atoms (graphite, of course, but also organic material): an optimal candidate for future industrial applications.

Other methods

Other methods for graphene production include Molecular beam epitaxy on insulating surfaces [92], and chemical synthesis. Graphene can be chemically synthesized assembling benzene building blocks [93,94] at temperatures <200 °C, with the potential of chemical precision over the control of edges an

molecular shapes. This approach is presently limited to structures smaller than 1 µm in size, with objects closer to the 1D and 0D carbon allotropes than to graphene.

General properties of graphene

A number of typical values for graphene's physical properties are reported in Table 1.1. Among them, let us outline the exceptional mobility (which is what makes graphene so appealing for nanoelectronics applications) and Young modulus (particularly for in-plain stresses, graphene is an extremely strong material).

Table 1.1: Typical values for graphene's physical properties. In Ref. [95], $\bar{n} = n/(10^{10}\ \text{cm}^{-2})$, the sheet conductivity σ is measured in units of e^2/h (typically near the Dirac point $n \approx 10^{12}\ \text{cm}^{-2}$ and $\sigma \approx e^2/h$)

Quantity	Values		Ref.	Comparison
Fermi wave vector k_F	$1.77 \times 10^5\ \sqrt{\bar{n}}$	cm^{-1}	[95]	
Fermi Energy E_F	$11.65\ \sqrt{\bar{n}}$	meV	[95]	$\propto n$ in 2DEG
DOS at E_F	$1.71 \times 10^9\ \sqrt{\bar{n}}$	$\text{meV}^{-1}\text{cm}^{-2}$	[95]	const. in 2DEG
Mobility μ	2.5×10^5	$\text{cm}^2\text{V}^{-1}\text{s}^{-1}$	[1]	$\leqslant$ 1400 Si
Sheet conductivity[3]	$\sim e^2/h$		[1]	
Max current density	$\sim 10^8$	A/cm^2	[96]	Cu wire $\sim 10^6$
Thermal conductivity	~ 5	kW/mK	[97]	~ C-nanotube
Young modulus	1.02	TPa	[2]	~ Diamond

1.3 Graphene's structure

The honeycomb structure in graphene is a truly 2-dimensional lattice[4] with an interatomic distance d_0 = 1.42 Å. Strong covalent bonds hold each atom to its 3 nearest neighbors: these σ-bonds, arising from an sp^2 hybridization of the

[3] Near Dirac point

[4] In contrast, for instance, to *quasi*-2D structures, such as 2D electron gasses in GaAs-AlGaAs heterostructures.

$2s$ and $2p$ orbitals, are similar to the ones to be found in diamond and give graphene outstanding mechanical properties.

This structure leaves only one electron per carbon atom available for conduction. Its p_z-orbital stands perpendicularly to the graphene plane and "can bind covalently with neighbourign carbon atoms, leading to the formation of the π-band" [98]. Since there is no overlap between the π band and the in-plane sp^2 orbitals, electrons can not hop between π-orbitals and σ-orbitals, thus transport in graphene can only take place through the 2D π-band.

The Brillouin zone counts two carbon atoms. The real-space coordinates of the two atoms correspond in momentum space to two points of particular interest for the band structure of graphene, usually referred to as the *K* and *K'* points.

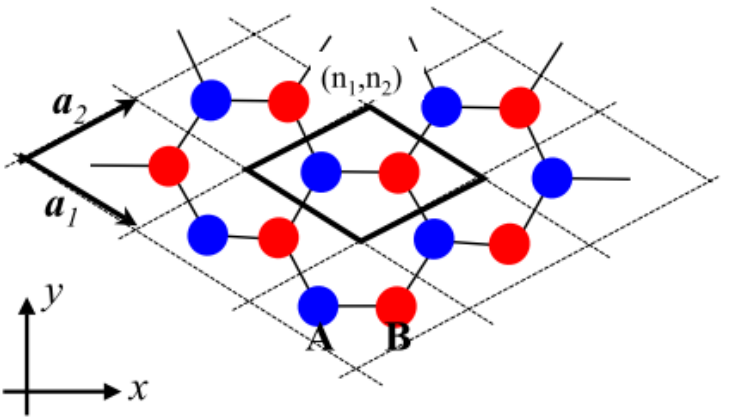

Figure 1.4: The graphene lattice. The unit cell (in thick black line), the A- and the B-sublattice (in red and blue) have been highlighted. Image adapted from [99].

Graphene's band structure and DOS

A complete derivation of graphite and graphene's band structure (within the Tight Binding approximation) was first done by Wallance [100]. Considering hopping only between first nearest neighbours, the eigenvalues of energy may be expressed [99] as:

$$E(\mathbf{k}) = \pm V_{pp\pi}\sqrt{3 + 2\left[\cos(\mathbf{k}\cdot\mathbf{a}_1) + \cos(\mathbf{k}\cdot\mathbf{a}_2) + \cos(\mathbf{k}\cdot(\mathbf{a}_1 - \mathbf{a}_2))\right]} \tag{1.1}$$

where $\mathbf{a}_1$ and $\mathbf{a}_2$ are the graphene lattice vectors and $V_{pp\pi}$ is the overlapping integral between p_z-orbitals. Figure 1.5 shows the shape of the $E(\mathbf{k})$ surfaces: the points in momentum space where the upper and lower band meet are called the *Dirac* points and are in direct correspondence with the A- and B-lattices shown in Figure 1.4. Close to these points the bandstructure becomes linear in energy, as one can see by expanding Eq. 1.1 around $\mathbf{k} = \mathbf{K}+\mathbf{q}$, for $|\mathbf{q}| \ll |\mathbf{K}|$, obtaining, to first order [99]:

$$E(\mathbf{q}) \approx \pm\hbar v_F|\mathbf{q}| \qquad v_F = \frac{3}{2}\frac{V_{pp\pi}d_0}{\hbar}$$

Remarkably:

1. graphene's bandgap is a set of measure zero [95], also described as a gap-less semiconductor: by doping the graphene it is possible to continuously change between electrons and holes carriers;

2. The energy value for $\mathbf{q} = 0$ is the intrinsic Fermi Level energy of graphene. We will refer to this as to the *energy of the Dirac point*: $E_D \equiv E(\mathbf{q} = 0)$

3. the charge carriers' velocity $v = \frac{1}{\hbar}\frac{\partial E}{\partial k}$ is independent of energy: all carriers move with the same velocity. This quantity is estimated to be ~10^6 m/s;

4. the presence of two non-equivalent Dirac-points introduces a new degeneracy, analogous to the spin one, often referred to as *pseudospin*, which is a good quantum number for $|q| \ll |k - K|$;

5. the effective mass $m^* \propto \frac{\partial^2 E}{\partial k^2} \to 0$ for values of k close to the Dirac points: the low-energy excitations for graphene [98].

The Density of States (DOS) for graphene may then be easily computed considering the number N of available states for a given $k(E)$ and the volume in

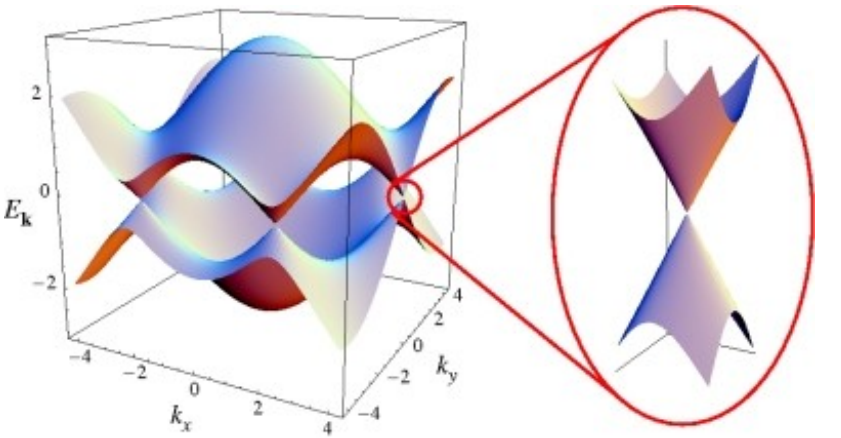

Figure 1.5: Graphene's bandstructure, adapted from [98].

the reciprocal space for a single state (*i.e.* $(2\pi/a_x \cdot 2\pi/a_y)/s$, where a_x and a_y are the lattice vectors in real space and s accounts for degeneracies):

$$D(E) = \frac{\mathrm{d}N}{\mathrm{d}E} = \frac{\mathrm{d}}{\mathrm{d}E}\left(\frac{\pi q^2}{\frac{1}{s}\frac{2\pi}{a_x}\frac{2\pi}{a_y}}\right) = s\frac{a_x a_y}{2\pi} q \frac{\mathrm{d}q}{\mathrm{d}E} = s\frac{a_x a_y}{2\pi}\frac{q}{\hbar v} = s\frac{a_x a_y}{h}\frac{q}{v} \tag{1.2}$$

where we have used the fact that $v = \frac{1}{\hbar}\frac{\partial E}{\partial k}$. The factor s should account for spin degeneracy and, in the particular case of graphene, also for valley degeneracy, yielding $s = 4$. The fact that v is a constant in graphene[5] shall also be considered, from which we obtain:

$$D(E) = \frac{4a_x a_y}{h}\frac{q}{v} \propto q \tag{1.3}$$

1.4 Graphene for electron transport

It is possible to shift the energy of the Dirac Point E_D with respect to the Fermi Enerfy E_F by realizing Field Effect Transistor (FET) geometries where

[5] At least for values of k close to the Dirac point, which is the only regime investigated in this work.

the graphene serves as conduction channel (see Section 3.4). In such a geometry, an electrostatic coupling is established between the graphene and a gate-electrode, allowing for a direct correspondence between the applied gate voltage V_g and the energy $E_D - E_F$. This effectively allows the experimenter to tune the filling of the graphene bands, and therefore the surface density of charge carriers, n_s and the conductivity of the graphene, by controlling V_g.

In order to understand how this tunability reflects in the electric transport through graphene, let us consider the Fermi functions $f_1(E)$ and $f_2(E)$ of two electrical contacts with chemical potentials μ_1 and μ_2, driving a current through a graphene sheet; let $D(E)$ be the graphene's DOS and $v(E)$ the velocity of its charge carriers. In a ballistic description, with a low bias applied between the electrodes, we can write [101]:

$$\begin{aligned} I \propto n_s e v_x &\propto \int \mathrm{d}E[f_1(E) - f_2(E)]D(E)\mathbf{v}_x(E) \\ &\approx \int \mathrm{d}E \frac{\partial f(E)}{\partial E}[\mu_1 - \mu_2]D(E)\mathbf{v}_x(E) \\ &\approx [\mu_1 - \mu_2]D(\epsilon_F)\mathbf{v}_x(\epsilon_F) \end{aligned}$$

where ϵ_F is the Fermi energy of the charge carriers in the graphene and $\mathbf{v}_x(E)$ is the average velocity a carrier with energy E will have in the transport direction. We can use this [101], to extract the dependence of the conductance over the carrier density: for low bias, the carrier velocity in graphene is constant, therefore by using Eq. 1.3 we conclude that the conductance $G = I/V_{sd}$ will be:

$$G \propto D(\epsilon_F) \propto q$$

From Eq. 1.2 we have $n_s \propto N(E) \propto q^2$, therefore:

$$G \propto \sqrt{n_s} \tag{1.4}$$

Scattering

Experimental evidence is not always in agreement with $G \propto \sqrt{n_s}$: in fact it is more common to see $G \propto n_s$ away from the Dirac point and $G \propto n_s^2$ at the Dirac point, as shown in Figure 1.6. The impossibility of reaching zero conductivity may be thought as an effect of the thermal spreading of the Fermi function,

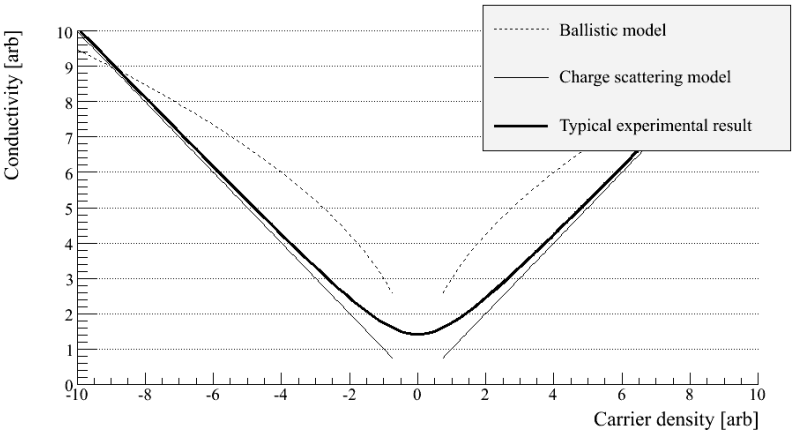

Figure 1.6: Dependence of the conductivity over the charge carriers. The different curves refer to the ballistic expectation, the charge impurity scattering model and a typical experimental result.

but measurements have been reported [102] where a finite minimum conductivity was observed even at temperatures as low as 5K. On the other hand, [103] showed how "electron-hole puddles", which would cause local variations of the charge neutrality point, are a possible explanation to the phenomenon. Similarly, the most probable explanation for the $G \propto n_s$ behavior away from the Dirac points is scattering: the presence of charge impurities between the graphene and the insulator can indeed give rise to such a linear relation [104] and is the most largely accepted interpretation.

A convincing argument for this interpretation can be found in [105], where a detailed calculation on the mean scattering time τ is carried out. The authors confront the dependence on the carriers density of τ for the different mechanisms of Coulomb and short-range scattering[6]. The scattering times are found to be $\tau_c \propto \sqrt{n_s}$ for the former and $\tau_s \propto 1/\sqrt{n_s}$ for the later, implying that, for small carrier densities, Coulomb scattering would dominate over the short range one.

Experimental evidence also suggests that charged impurities may be playing a relevant role. Chen *et al.* [106] have doped graphene samples with potassium ions: on increasing K-doping, $\sigma(n_s)$ becomes systematically more and

[6]For the Coulomb scattering, the assumption is that the scatterers are randomly distributed in a plane close to the graphene sample.

more linear, suggesting this linearity to be a signature of Coulomb scattering in graphene.

Although some discussion is still active, the general outcome in the literature is the perception that scattering mechanisms in graphene play a quite relevant role. Pristine graphene's electronic features, particularly at the charge neutrality point, are masked to such an extent that "the Dirac point physics" is "experimentally inaccessible, at least for current graphene samples" [107][7].

Typical values of graphene conductivity reported in the litterature [103] are on the order of 10^{-4} S and show a minimum value $\sim 4e^2/h$. The origin of this minimum conductivity are experimentally found in charge-hole puddles forming in the graphene at low carrier densities, most likely a result of charge impurities in the substrates [22,95,103]. The ultimate ballistic limit is expected to be a conduction $\sigma = e^2/\pi h$ per spin per valley [108], however experimental evidence for this is still lacking and the reference value to date for the expected minimum conductivity of graphene is not more precise than "of the order of $4e^2/h$" [18].

Mobility

Recalling graphene's linear dispersion relation, which implies $\hbar v = \partial E/\partial k$ being a constant, it is easy to see how the the classical definition $v_{drift} = \mu E$ implies μ not being a constant any more. One can still use $\sigma = n|q|\mu$ as a definition for the mobility and measure it as the derivative of the conductivity with respect to the gate voltage (which is what is controlling the number of charges induced on the graphene), but keeping in mind that the mobility will generally depend on the gate voltage [109]:

$$\sigma = n|q|\mu \qquad \Rightarrow \frac{1}{|q|}\frac{\partial \sigma}{\partial n} = \frac{1}{C_g}\frac{\partial \sigma}{\partial V_g} = \mu + V_g \frac{\partial \mu}{\partial V_g}$$

where C_g is the gate capacitance. As noted in [109], "the last term is not insignificant at low densities", therefore one should consider:

$$\boxed{\mu_b = \frac{\sigma - \sigma_{min}}{C_g(V_g - V_{g_{min}})} \qquad \text{instead of} \qquad \mu_a = \frac{1}{C_g}\frac{\partial \sigma}{\partial V_g}} \tag{1.5}$$

[7] In this particular quote, [107] refer to the relativistic physics in graphene for energies asymptotically close to the Dirac point.

where V_g is the gate voltage and $V_{g_{min}}$ is the gate voltage where the minimum conductance is found.

A different suggestion was made by [110], namely to fit the resistivity measurements by using

$$\boxed{\rho = \frac{1}{\mu_c e \sqrt{n_{imp}^2 + n^2[V_g - V_{g_{min}}]}}} \tag{1.6}$$

where n_{imp} is the density of charged impurities and $n(V)$ is the gate-induced carrier density. One the one hand, this function generally fits the experimental data very well; at the same time though, it has a substantial difference with μ_a and μ_b: the mobility is a *constant* value, a parameter for the fit procedure, rather than a quantity depending on the carrier density.

At this point three ways to measure mobility have been introduced: the usual differential definition μ_a, the expression μ_b in Eq. 1.5, and the fitting parameter μ_c in Eq. 1.6. The differences between these three options are outlined in Figure 1.6: while the three tend to the same mobility value for large carrier density, near the Dirac point the differences can be substantial and a natural question arises on which one is the value of mobility. The answer probably stands in the particular context being considered: if the concern is simply to use the order of magnitude of the mobility to roughly characterize the electrical quality of the sample, then μ_c is a valid measure of mobility. On the other hand, if there is an interest in the transport properties of the graphene flake very close to the Dirac point, one might want to consider μ_b instead. Generalizing is not trivial, but clearly in the case of fabrication and testing of graphene devices, one would have to relate these quantities to the actual performance of the sample, to understand which one is the more meaningful in that context.

Experimental realizations: state of the art

Requirements and achievements in the academic and industrial world differ significantly. For the industry, the high mobility and high current density make graphene ideal as a replacement for Cu interconnects [111], with projections for digital graphene electronics on a longer timescale. The long-term target plan (>20 years) is to transform graphene transistors, from being excellent tools to probe the transport properties of this material, to viable devices

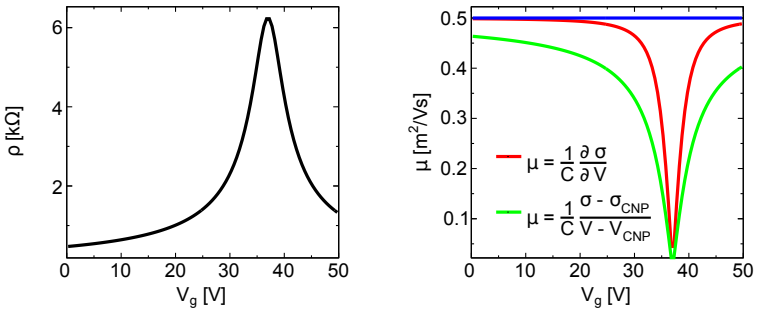

Figure 1.7: Different approaches to estimating mobility. Kim's function (Eq. 1.6) is plotted the left graph for a particular choice of the fitting parameters (μ_c = 5000 $cm^2V^{-1}s^{-1}$, $n_{imp} = 2 \times 10^{11}$ cm^{-2}, $V_{g_{min}}$ = 37 V). Mobility is then computed from this curve and shown in the graph to the right. Shishir's limit for large voltage is Kim's mobility, although near the charge neutrality point the the two estimations differ significantly.

to compete with state-of-the-art Si semiconductor electronics. Top-gated graphene field effect transistor (GFET) have been made with graphene produced by mechanical exfoliation [112–116], carbon segregation [117] and CVD [118], with high perfomances reached by utilizing ultra-thin AlO_x gate dielectrics [119,120]. Remarcable high frequency electronics has been demonstrated, with cut-off frequency of 427 GHz for a 67 nm channel length graphene transistor [121].

For more fundamental research, graphene samples are most typically realized by micromechanical cleavage or by CVD, the later followed by transfer on insulating substrates (most commonly SiO_2 or h-BN). Various protocols have been developed for the transfer, and can be categorized in either "wet" or "dry" ones. The former consists in covering the graphene with a sacrificial polymer, immersing the sample in a solution that would etch the substrate and transfering the polymer-coated graphene on a different substrate, where the polymer can eventually be dissolved, releasing the graphene [122]. The later aims at achieving cleaner interfaces by avoiding liquids, for example by exploting the Van der Waals interaction between 2d materials to assemble heterostructures: an isolated few layer BN flake can be used as a stamp to successively pick up alternating layers of monolayer graphene and few-layer BN [123]. Thermal

annealing in H_2/Ar is normally used to remove polymer residuals [1,123,124].

Annealing in vacuum has proven to reduce both doping and hysteresis [103,106,125]. Furthermore, the particular choice of the substrate (which can dope, deform the graphene or introduce unwanted scattering effects) can make a quite relevant impact on the graphene sample: hysteresis effects are strongly suppressed when graphene is laid over a thin layer of hexamethyldisilazane (HMDS) [125] or on h-BN [91], where it can reach mobilities almost an order of magnitude greater than on SiO_2.

2

Fabrication techniques for graphene devices

Graphene comes in different sizes and forms, as discussed in Chapter 1. However, when it comes to making an electrical device out of it, be it for charge or spin transport, the main fabrication steps are quite commonly the same ones: lithography, etching and metal depositions. This section provides an overview on these fabrication techniques and on the details used for the specific devices of this work.

2.1 Lithography

Lithography (EBL) is a well established technique in micro- and nano-fabrication for controlling the physical dimensions of devices and their components across a wide range of sizes, from millimeters to few tens of nanometers. It is often used in conjunction with other fabrication techniques, such as etching and metal deposition, as a means to transfer the desired geometrical patterns to the sample (as opposed to, for instance, a homogeneous etching or metallization of the whole surface of the sample).

The lithographic process

In micro- and nano-fabrication, lithography typically refers to a process where a pre-determined pattern is transferred to a (particular) polymer called *resist*. Most commonly, this is either an electron-beam or a photo sensitive polymer, so that the exposure of the resist to such radiation will locally change its solubility in a characteristic chemical (the *developer*). Photo-sensitive resists lack the resolution required in the details of the devices we fabricated thus, for the purpose of this work, we focus on the electron beam lithography technique.

A typical lithographic process is sketched in Figure 2.1. An electron-beam sensitive polymer, diluted in a solvent, is spun over the sample surface and subsequently baked to form a homogeneous, solid film over the sample's surface. The exposure of a selected area of this film to a high voltage beam of electrons causes the solubility of the polymer to change locally: upon immersion in the corresponding developer, the exposed area will dissolve leaving the unexposed intact, which can then be used as a mask for an etching or a metal deposition step.

What we have just described is a *positive* resist, a polymer such that its solubility increases upon exposure, as opposed to *negative* resists, which feature polymers with a lower solubility upon exposure. Photo-sensitive resists are also commercially available where the solubility of the polymer changes with exposure to ultra violet light instead of electron beams. However photoresists lack the resolution required in the details of the devices we fabricated thus, for the purpose of this work, we focus on the electron beam lithography technique.

Electron beam lithography

The Electron Beam Lithography (EBL) technique consists in scanning a focused beam of electrons over an electron-sensitive polymer (often called *resist*) in order to induce very local, controlled irradiation of the later. The patterns written over the resist can then be transferred to other materials, achieving spacial resolutions well below 100 nm.

The main body of an EBL equipment is composed can typically be broken down into four sections. The *column* system, where the beam of electrons is generated focused and directed. A high-precision stage positioning system, which controls the positioning of the sample-holder in the three spacial coordinates

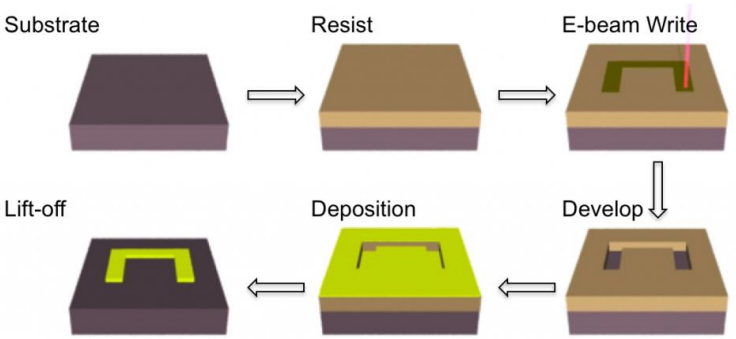

Figure 2.1: Sketch of a typical fabrication process using EBL and metal deposition. Adpted from [126]

with interferometric precision. A lithography control system, which is the set of hardware controlling the former two. A vacuum control system, for ensuring (ultra) high-vacuum conditions in the different chambers of the column and stage system.

The column system (see Figure 2.2) is in turn constituted by an *electron gun* and a high voltage section to generate the beam, a number of beam blankers to rapidly switch the beam on and off, a set of electromagnetic lenses for sharpening and focusing. Finally the beam hits the specimen, ultimately less than 2 nm wide. The generation of beam is typically obtained through Field Emission, where a very high electric field ($\sim 10^9$ V/m) is applied normal to a metal surface, causing electrons to leave the metal and project into vacuum. The metal tip of the cathode can be left at room temperature (*cold* emission) or heated up to 1500 °C when used (*hot* emission) . Electrons are then accelerated by a high voltage, which can span from 10 kV to 100 kV depending on the particular system in use. The electromagnetic lenses deflect the beam in order to correct for alignment (*i.e.* the axis of the beam not overlapping the axis of the column), astigmatism (*i.e.* the ellipticity of the apparent beam-form on the specimen changes with small deflections of the beam) and deflection (*i.e.* the positional accuracy in the stage plane for the pattern exposure). Additionally, blankers are introduced to rapidly interrupt the flux of electrons reaching the specimen, which is essential in order to draw unconnected patterns over the sample.

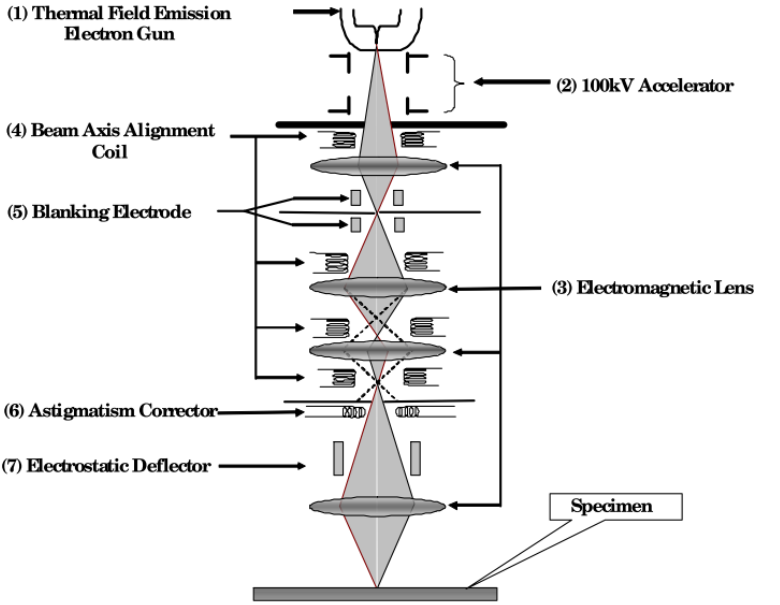

Figure 2.2: Cross-section drawing of an electron-optical control system along with a ray-trace of the electrons as they pass through a series of electron-optical components. [127]

The geometry of the pattern to be drawn (or *written*) is typically created in a CAD software, and can extend to wafer-size dimensions. The e-beam, however, can only be bent for small angles before issues with focus and resolution start to emerge. For this reason, the sample stage aids the process by displacing the sample. As illustrated in Figure 2.3, the design is divided into *write field* areas, of typical lateral dimensions between 100 µm and 1 mm. At first, the stage positioning system will position the sample so that one given write field sits precisely below the column. The electrostatic deflector will then bend the e-beam in order to write the pattern in the resist, but only within the boundaries of the given write field area, which will assure small bending angles. The write field is in turn subdivided into smaller areas, a fin grid of pitch size (also know as *step size*) ~10-100nm, which is used to discretize the areas in the drawing. The drawing is transferred to the resist by scanning the beam over such a grid, with a velocity regulated by the pre-determined amount of charge per unit area (or *dose*) to be delivered over the resist. Most commonly the beam will not scan the whole write field area (*raster* mode), but cover only the regions of interest (*vector* mode), as shown in Figure 2.3.

Finally, the stage will physically move the sample to the next write field, iterating the whole process. If the specimen contains physical marks within a write field (*e.g.* pre-fabricated metallic structures), additional precision can be achieved by scanning such marks, comparing their position in the stage plane with the one in the design and projecting a finely corrected pattern (*e.g.* correcting for rotation or translation misalignment), in order to match the two.

Optimizing the spacial resolution

The ultimate spacial resolution achievable with the EBL method varies considerably with the type of resist, substrate and lithographic machine. A critical parameter for comparing the quality of resists is their *contrast*, which is a measure of how abruptly the solubility of the polymer changes with an increasing exposure dose, as illustrated in Figure 2.4. A give resist will have a characteristic dose D_c: exposing the resist with a lower dose will leave it intact, whereas a higher dose will change its solubility compared to an unexposed sample. However, there always is a "grey zone" of dose values around D_c where the developed film will change in thickness: a higher resolution resist will have a more sharply defined clearing dose. The contrast for a positive (negative) resist is defined as $\gamma = \log_{10}(D_{100}/D_0)$, where D_{100} is the highest dose for which no

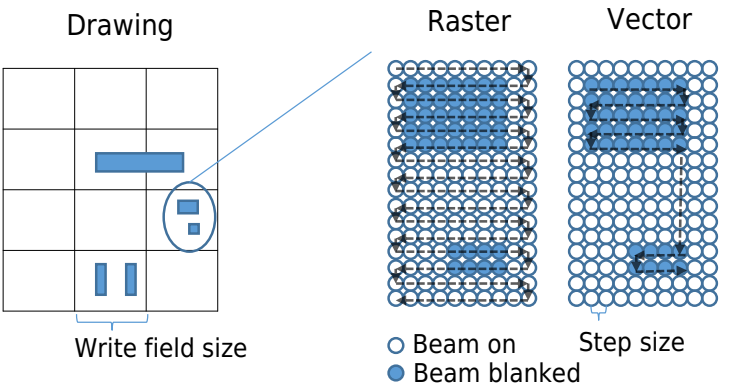

Figure 2.3: Schematics of different EBL writing strategies steps. Left, The initial drawing (typically created in a CAD environment) is divided into a number of *write fields*, which have typical dimensions of the order of 100 µm. The EBL will take advantage of the stage positioning to move the specimen with respect to the column, one write field at the time. Right, within a single write field the area is sub-divided into points, separted by a *step size* length. The beam can either scan the whole write field, opening and closing the blankers according to the initial drawing (raster mode) or scan over the regions of interest only (vector mode).

film thickness is lost (present) after development and D_0 the lowest dose for which the full film thickness is cleared (reached).

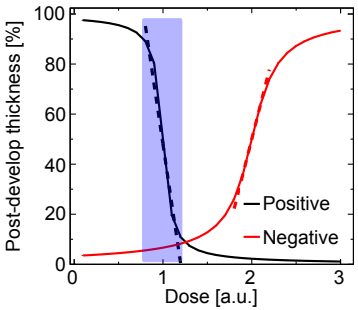

Figure 2.4: Example of a typical behavior for positive and negative resists, with different contrasts between the two. The steeper range of the dose curves is typically fitted to linear curve (dashed line) to extract the value of the contrast. The range between D_{100} and D_c is highlighted for the case of positive resist ($D_{100} \gtrless D_c$ for negative/positive resists, respectively). The diagonal across this region is what defines the contrast of the resist.

The lithographic equipment is typically the other major limiting factor for the spacial resolution. The electron beam used to expose the resist will always have a finite cross sectional size, typically with a gaussian radial distribution. Although this primary beam can be very tightly focused ($\sigma < 5nm$), the contributions from the secondary electrons backscattering from the substrate can extend up to distances of tens of microns, effectively exposing the polymer. A resist with a lower contrast will then see slanted cross-sectional profiles where a high contrast one will have very sharp ones.

The cross section profile of the resist is as well of crucial relevance in the fabrication process, particularly if a metal deposition is to follow: the sharpness and the height of the lithographic step compared to the thickness of the deposited metallic film can be critical to the success of the fabrication. As shown in Figure 2.5, an *overcut* profile - one where the area of the resist in contact with the substrate is larger than the free one at the surface - is highly unfavorable: the metallic layer on top of the resist will likely strip off the metal at the bottom during the liftoff step. At the opposite end, an *undercut* profile is much more favorable for a sharp definition of the metallic features. A typical way to

achieve this is to use two resist layers, a bottom one with a lower clearing dose and a top one with a larger resolution: the outcome is a slight undercut in the profile of the whole resist, as the bottom one will clear a larger area than the top one under the same EBL conditions.

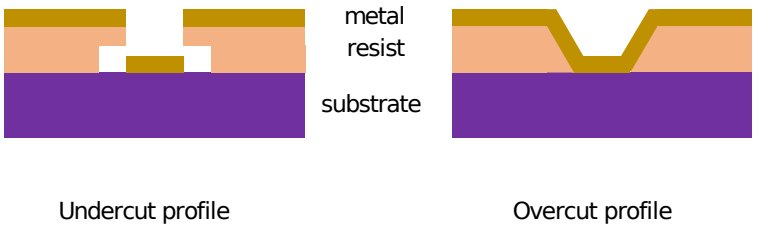

Figure 2.5: Undercut (left) and overcut (right) resist profiles at the metallization step

Our equipment

PMMA is one of the most common e-beam resist. It is commercially available and comes in a few different versions, where the molecular weight of the polymer is tuned to fit different fabrication requirements. Specifically to this work, two versions of the resist have been used: PMMA 495k and PMMA 950k (where the numbers refer to the molecular weights of the polymers). Staking the second over the first, one can take advantage of the different sensitivities (*i.e.* the difference in D_c values) and contrast of the two resists and obtain an undercut-profile. The double-layer approach is a great strategy to achieve an undercut profile and specific resists have been developed to promote it. Using LOR, a positive resist based on polydimethylglutarimide (PMGI), as a bottom resist and PMMA as a top one, for instance, can deliver impressive undercut profiles [127] (see Figure 2.6).

One other resists tested in this work is ZEP 520A, which compared to PMMA can deliver structures with higher aspect ratios, tends to be more resilient to etching steps and has a much smaller clearing dose (≈ 35 μC/cm^2, compared to the typical 100 μC/cm^2 for PMMA) - which translates to approximately three times shorter writing times in the lithography step.

Where resolution and mechanical stability seemed to favor, however, chemistry turned out to play against. For the specific fabrication over graphene, chemi-

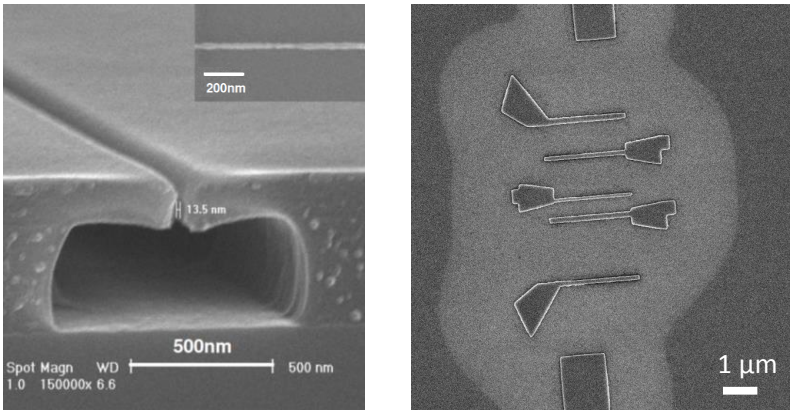

Figure 2.6: Left, SEM image of a double-layer-resist profile. Note the narrow linewidth in the top PMMA layer and the large undercut in the LOR bottom layer, 13.5 nm and 430 nm respectively. Adapted from [127]. Right, SEM image of a fabrication test for Co spin valve electrodes with a LOR/PMMA double layer resist. The large LOR undercut appears here as a contrast between the area covered by post-liftoff resist residues (darker grey, outer part of the image) and the area where the LOR undercut was developed (lighter grey, center of image). The Co structures at the center are sharply defined by the top PMMA layer, which bridges the LOR micro-meter-sized undercut during the metal deposition.

cal residues left on the surface can play a major role - especially as there is no physical way to etch them without etching the graphene itself. The developer and remover for the ZEP 520A, as it turns out, will leave the surface of the CVD graphene with a layer of residues visible simply by optical inspection. On the other hand, the developer for the LOR resist contains tetramethylammonium hydroxide (TMAH), which will chemically etch AlO_x, a determinant component for a working spin valve on graphene (as we will see in Chapter). For these reasons, our resist of choice remained PMMA, which has proved more than sufficient in delivering the required spacial resolution.

For the samples presented in this work, two EBL writing systems have been used, a *RAITH* 150-TWO and a *RAITH* e-LINE PLUS, with 10kV acceleration voltage. The resist of choice was a PMMA 495k/950k double layer and a mixture of methylisobutylketone (MIBK) and isopropanol (IPA), with a ratio of 1 to 3, as a developer.

2.2 Etching

On a general account, miniaturization and integration of individual components is a fundamental aspect of the present electronic technology. At the same time, spin and charge transport are best modeled and understood when there is control over the physical shape and dimensions of the channel. For graphene, the most common way to achieve both miniaturization and shape-control is by etching: although it is possible to grow small nanoribbons [128] or to define graphene stripes on SiC [129], the most flexible and used strategy is to cover the graphene with a lithographically defined mask and etch away what is not needed. We will briefly introduce here the etching techniques explored for this work and refer to Chapter *3.Characterization of devices* for assessing their effectiveness on the fabrication process.

Oxygen plasma

Possibly the most common way to etch graphene is to use an oxygen plasma. As it is the etching of a carbon monolayer, the powers and times required to etch are quite small, with typical values ranging around 40 W and 20-30 s. At the same time, this process will etch any organic material as well, typically reducing the thickness of a masking resist or changing the lateral dimensions

defined by lithography, implies a lower control on the critical dimensions for nanoscale devices. We have used a plasma asher (typically 50 W power, 10 sccm of O_2 at 1 mbar, 30 s exposure) in a few fabrication processes.

Ion milling

An alternative way is to rely on a purely physical etch, instead of a chemical one like the oxygen plasma. In an Ion miller, an argon plasma is accelerated in the direction of the sample, where the Ar ions will impact the un-masked graphene. This method has the advantage of an enhanced directionality of the etching process, which can be critical when fabricating small structures. On the other hand, however, it involves the exposure of the masking resist to a beam of accelerated charged particles: depending on the kinetic energy of the ions and their spacial density, an ion milling can effectively result in a change of the polymeric structure of the resist, in a similar way to an electron beam exposure. In the context of this work, an ion beam milling machine by *4Wave* has been used for etching of graphene and removal of resist residues (20-30 s at 50 V accelerating voltage, Ar gas).

Reactive Ion Etch

A Reactive Ion Etch is the most versatile among the presented etching techniques. Depending on the gas specie and the plasma parameters used, it can deliver chemically driven etchings (which will tend to be more isotropic) or physically driven ones (generally more directional). It is a common tool in the micro and nano-fabrication industry and it has been the technique of choice for the etching of CVD graphene in the fabrication of the devices for this work. We have been using a mixture of Ar and O_2 with flows of 80 sccm and 5 sccm respectively, at a pressure of 40 mTorr and a power of 40 W, for an etching time of 30 s, in a Plasmalab machine by *Oxford Instruments*.

2.3 Metal deposition

Electrical contact to the graphene devices of this work is achieved by first defining the shape of the electrodes with electron beam lithography and then covering the surface of the whole sample with a metallic layer. Upon removal of

the resist (by immersion in a solvent), the metal covering the masked areas in between electrodes will lift (this step is referred to as the *liftoff*), leaving on the sample only the lithographically defined electrodes. The quality of the electrodes at the end of the process depends on the quality of the material that has been deposited in the first place, which is why typically metallization steps are done in Ultra High Vacuum chambers. At the same time, it also depends on the profile of the resist layer and how it is covered by the metal. This section deals with the technical aspects of the liftoff and metal deposition processes.

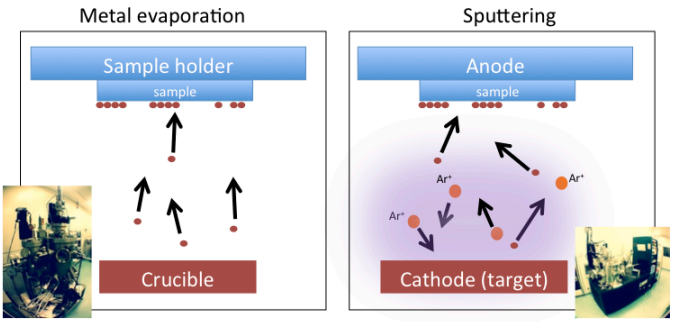

Figure 2.7: Sketches for the metal evaporation (left) and sputtering (right) depositions processes

Evaporation

One of the most common techniques for thin-film deposition in micro- and nanoelectronics is metal evaporation in a vacuum chamber. In a *thermal* evaporation, the material is molten in a metallic boat, which in turn is heated with an electrical current by Joule effect. Alternatively, in an *electron-beam evaporation* a beam of electrons is focused onto the metal, which then melts and evaporates (or sublimes). At sufficiently low pressures[1], the mean free path for the evaporated particles is order of magnitudes larger than the source-sample distance, which delivers a very directional deposition. Upon reaching the sample, the material condenses. The deposition rate is monitored through an oscillating quartz crystal, whose resonance frequency will diminish as metal is deposited over it. Typical deposition rates are of the order of 10^{-2}-1 nm/s, for

[1]Typical pressure levels in High and Ultra High Vacuum chambers are of the order of 10^{-3}-10^{-8} and 10^{-8}-10^{-11} Torr, respectively.

a total thickness ranging from ~1 nm (creation of AlO_x resistive interfaces) up to 40 nm (ohmic, low resistance contacts).

Characteristic of this method of deposition, as mentioned, is the directionality of the depositing material: the evaporated particles will reach the sample with little dispersion in their angle of incidence. This is typically used as an advantage. For instance, depositions done at different incidence angles can achieve sub-lithographic precision. Or again, depositing over carefully designed masks can ease the liftoff process by including an undercut profile (see Figure 2.5). On the other hand, this makes the final metallic layer very sensitive to the roughness of the substrate, thus in some occasions the sample is mounted on a rotating plate, to uniform the coverage.

For the fabrication of the devices presented in this work, several equipments have been used for metal deposition including an *Oerlikon* Univex system (thermal deposition of Au, e-beam deposition of Co and Py, 10^{-6} mbar), a *Kurt Lesker* evaporator (thermal deposition of Al, e-beam deposition of Co, 10^{-6} mbar), a *Theva* system (e-beam deposition of Cu, 10^{-8} mbar) and a *Createc* MBE evaporator (Al and Co, 10^{-9} mbar).

Sputtering

In a sputtering process, atoms are ejected from a solid target by bombarding it with highly energetic charged particles. Typically, in a High Vacuum chamber an Ar plasma is used as a source of ions, which are then electrically accelerated towards the target. Transfer of kinetic energy from the ions to the target results in physical sputtering of the later. The material then diffuses in the chamber, finally depositing on the sample's surface. Compared to the evaporation technique, particles sputtered from the target will typically have a wider angular distribution and reach the sample with higher kinetic energies (see Figure 2.7). At the same time, it tends to be a quicker and more reproducible process. In the fabrication described in the following chapters we have used an *AJA* sputtering system (Co and Al sputtering, 10^{-9} mbar base pressure) and a *4Wave* system (Pd deposition, 10^{-9} mbar base pressure).

3 Characterization of devices

"If you can't measure it, you can't manage it", says a famous quote. The electrical devices described in the following chapters are the result of a careful optimization of the fabrication process, which can be systematically improved only if supported by effective (and timely) characterization means. The selection presented is far from a complete review of characterization tools for graphene, limiting ourselves to those techniques that have been most heavily used in assessing the fabrication process and the performance of the devices.

3.1 Optical microscopy

As already introduced in the first chapters, the possibility of seeing graphene with an optical microscope brought a significant breakthrough to the field right from the very first Field Effect Transistors in 2004 [5,7,13]. Being able to locate atomic monolayers "at a glance" is an impressive advantage compared to the long acquisition times and expertise required for Atomic Force Microscopy mappings, to name one other option. At the time of writing, optical microscopy is still the fastest and most immediate characterization tool for few layer graphene, provided the right substrate: on 300 nm of SiO_2 (or optically equivalent) graphene appears with just about enough contrast to be seen with an optical microscope under white light illumination.

A typical inspection of a graphene sample with an optical microscope can be used for a number of characterization purposes, among which are:

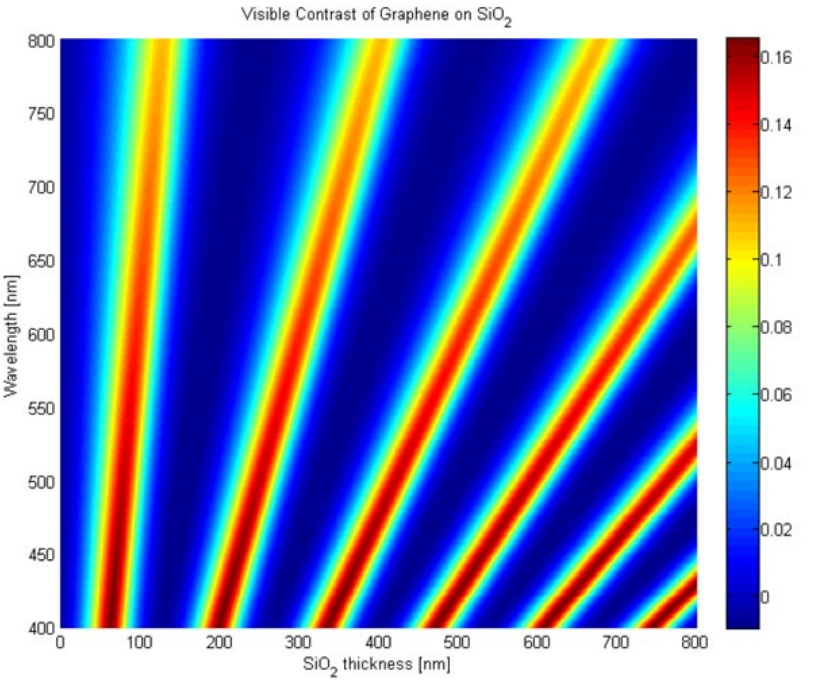

Figure 3.1: Optical contrast (color scale) for graphene on a SiO_2 substrate, as a function of SiO_2 thickness and light wavelength. Graphene is most visible (*i.e.* bests contrasts against the substrate) at particular values of substrate thickness, for instance for a yellow light ($\approx$ 590 nm, common in clean room facilities), graphene is most visible on a 90 nm or 300 nm thick SiO_2 substrate. Image adapted from [130].

- checking for occasional ruptures in the lattice or faulty transfer of the graphene onto the SiO_2 substrate;
- assessing the homogeneity of the lattice against grain boundaries, graphene folding or nucleation sites;
- trace residues after a lithographic step;
- asses the quality of an etching step (together with Raman);

Optical microscopy is the technique of choice for a rapid, qualitative assessment of the sample. Quantitative assessments can also be performed, comparing the absorption of green, red and blue light, but in our experience quantitative detail is more easily extracted from Raman measurements.

Dark Field (DF) imaging has proven to be a particularly useful one. DF is an illumination technique that excludes the un-scattered light from the final image [131], enhancing the contrast of edges and particles, with a sub-µm resolution. An example of a DF image is shown in Figure 3.2: ripples and nucleation sites are immediately visible, along with residues left from the fabrication processing. Most relevantly, the edges of the etched graphene clearly stand out against the black background.

We have used this, for instance, in assessing the effectiveness of various graphene-etching recipes, as un-etched graphene (or the edges of partially etched graphene) would be clearly visible in DF images. Raman mappings (see following section) can also be used for this purpose, but DF images have proven to be a sufficient[1] and far quicker method.

3.2 Scanning Electron Microscopy (SEM)

Electron microscopy is a very common technique in micro- and nanoelectronics. The images are produced by scanning a focused beam of electrons over the surface of the sample. Typically, the measured signal comes from collecting the secondary electrons emitted from the sample. An image is then formed by associating the position of the beam with the measured signal, as the beam raster-scans the specimen. This technique is often used to extract information about the topography and composition of the samples.

[1] We have experimentally verified that two devices that would appear disconnected in DF images would also appear disconnected in Raman mappings and in electrical measurements.

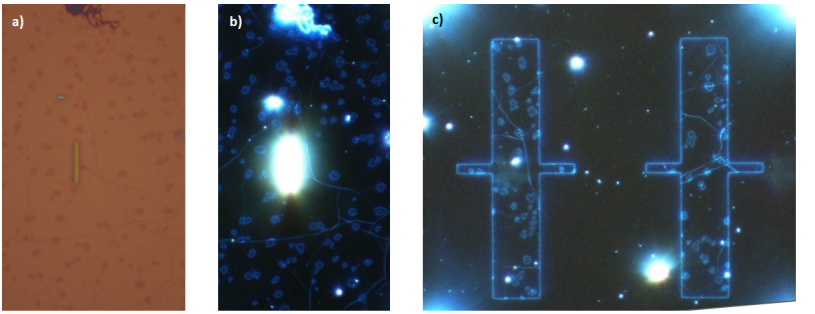

Figure 3.2: a) Optical Microscope image of a CVD graphene layer on a 300 nm SiO_2 substrate, with a PMMA over mask in the center for a following etching step; b) Dark field image of a), where we can see all the features of the CVD graphene (ripples, grain boundaries, eventual ruptures, *etc.*) with greater contrast than in a); c) dark field image after an etching process.

Compared to optical imaging, SEM has a great advantage in resolution. In the first place, there is no diffraction limit at the detection, since the detector is not a camera. In addition, the electron beam can be focused to probe much smaller areas than what is possible with white-light source typically available for optical microscopes. Resolutions below 100 nm are common, and nm resolutions attainable.

Information extracted from SEM images

Like in optical microscopy, contrast for extremely thin specimens requires a little carefulness can need a few attentions, specially when a thick substrates lies underneath. While a range of parameters is involved in optimizing an electron microscopy image, the acceleration voltage of the electron beam plays a major role in our context.

The secondary electrons that will eventually reach the SEM detector will typically originate within a few nanometers from the sample surface [132]. However, the majority of them will be produced deeper into the substrate for a more energetic beam (*e.g.* 30 kV), yielding lesser information on the first atomic layers. On the contrary, low-energy electron beams (*e.g.* 1 kV) will be more surface sensitive, albeit more difficult to focus. In our experience, graphene is almost completely transparent for acceleration voltages above 10 kV, but very

visible at 1-2 kV (see Figure 3.3), which is typically a low range for SEM.

We have been using SEM images for qualitative assessment of our devices, both of graphene and of metallic structures. For graphene we could extract information about lattice homogeneity and occasional ruptures, with much more details than what an optical image could tell. Particularly interesting in this context is that one of the sources for SEM contrast is a difference in electron density: granting all other things equal, an area with higher electron density has a higher probability of producing secondary electrons when exposed to an electron beam. In Figure 3.4 we show this effect on a graphene strip: the contrast between the upper half and the bottom one indicates that the two are not in electrical contact, which we then verified. Notably, from an optical image we could have not distinguished this from a ripple in the graphene.

On the other hand, when the interest lies on the metallic structures then higher acceleration voltages tend to be preferred: spacial resolution improves and material contrast is regained. We have used this type of imaging to asses different lithographic, metalization and liftoff techniques, particularly with respect to comparing geometries obtained to the designed ones and minimizing liftoff residues.

Long exposure to SEM can contaminate the graphene by covering it with polymerized hydrocarbons [133], so this technique has mostly been used after measurements.

3.3 Raman Spectroscopy

Raman spectroscopy has become a method of reference for graphene characterization. It analyzes the inelastic scattering of monochromatic light from the sample to infer information on the vibrational modes of the system, in a similar but complementary way to infrared spectroscopy [134], with differences that ultimately depend on the specific type of interaction between the molecule and the electromagnetic radiation. In Raman spectroscopy, the signal comes from analyzing the spectrum of the backscattered light: the elastically scattered light is filtered out and the inelastic component is sent to a spectrometer.

As explained in [135]:

> The two most intense features [in the Raman spectrum of graphene] are the G peak at ≈1580 cm^{-1} and a band at ≈2700

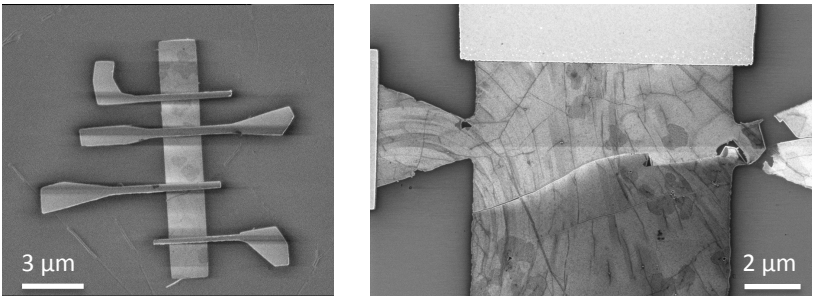

Figure 3.3: SEM images of graphene devices taken at different acceleration voltages. Left, a 30 kV acceleration-voltage image, good for contrasting different metals (for instance, the darker Co contacts at the center *versus* the lighter Au contacts branching to the outside of the image), but the graphene is invisible. Right, 1 kV acceleration-voltage image, where the material contrast is almost lost, but we gain a great surface sensitivity and can image graphene. We can also see points for improvement in the lithography, like horns and bubbles.

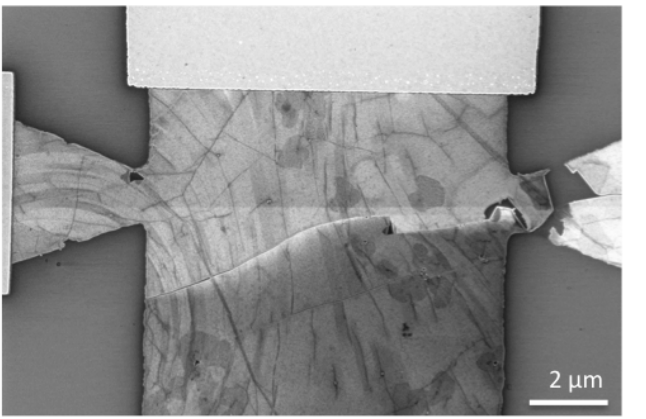

Figure 3.4: 1 kV acceleration-voltage SEM image of a graphene device contacted by Ti/Au leads. Notice the great surface detail we can extract and how the contrast between the lighter upper part of the graphene and the darker lower one further highlights the electrical disconnection.

cm^{-1}, historically named G' since it is the second most prominent peak always observed in graphite samples. The G peak is due to the doubly degenerate zone center E_{2g} mode [136]. On the contrary, the G' band has nothing to do with the G peak, but is the second order of zone-boundary phonons. Since zone-boundary phonons do not satisfy the Raman fundamental selection rule, they are not seen in first order Raman spectra of defect-free graphite [137]. Such phonons give rise to a peak at $\approx$1350 cm^{-1} in defected graphite, called D peak [136]. Thus, for clarity, we refer to the G' peak as 2D.

Information extracted from Raman measurements

The relative intensity of the 2D peak to the G peak can be used as an indicator of the number of graphene layers, the former being larger than the later for single layer graphene, while the opposite is true for graphite spectra. Additionally, single layer graphene has a single sharp 2D peak, while in a multilayer sample this is a band of (at least) two peaks [135,138], thus the width of the 2D feature can also be used to distinguish single layer graphene from thicker samples (a quite challenging task with other techniques such as, for instance, SEM), as shown in Figure 3.6.

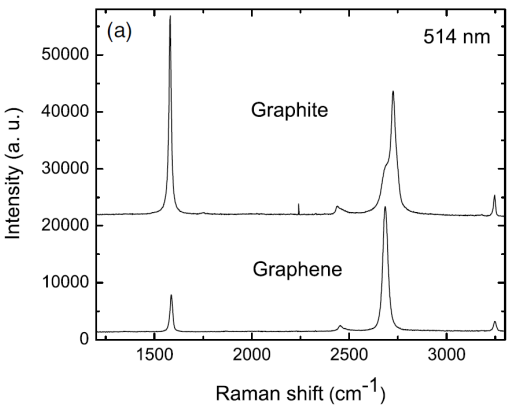

Figure 3.5: Comparison of Raman spectra at 514 nm for bulk graphite and graphene. Image adapted from [135].

Raman spectroscopy can also be used to monitor the doping and carrier den-

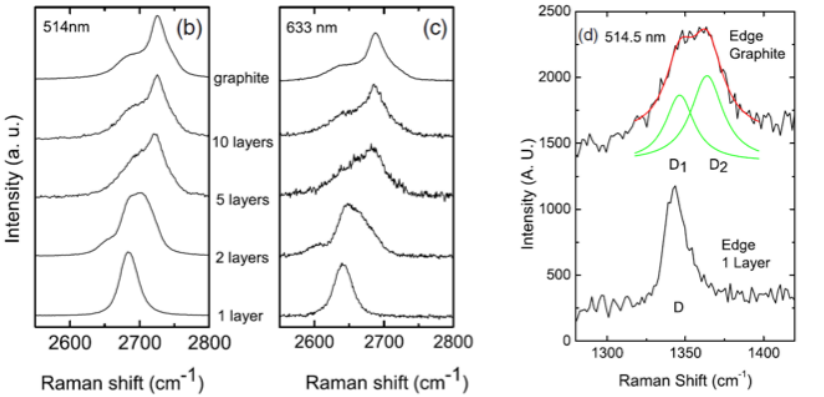

Figure 3.6: b) Evolution of the Raman spectra at 514 nm with the number of layers. c) Evolution of the Raman spectra at 633 nm with the number of layers. d) Comparison of the D band at 514 nm at the edge of bulk graphite and single layer graphene. The fit of the D1 and D2 components of the D band of bulk graphite is shown. Image adapted from [135].

sity in graphene samples. Casiraghi and coworkers first highlighted changes in graphene's Raman spectrum among samples with different doping [139], while Das *et al.* mapped systematic shifts in the Raman spectra of gated graphene as a function of the induced shift in electrochemical potential [140]. In both cases, Raman spectroscopy emerges as a promising tool for mapping the carrier density in graphene in a non-invasive way.

Summarizing, the literature on Raman spectroscopy suggests we can use this technique to extract the following information[2]:

- presence/absence of graphene
- number of layers (intensity of 2D to G peak)
- presence and density of defects (intensity of D to 2D peak)
- doping level in graphene [139,140]

Interestingly this information is a local one: the probed area is determined by the laser spot size and can be spatially mapped, provided a scanning sample-holder (see Figure 3.8).

[2]The list is not exhaustive, but tailored to the present work

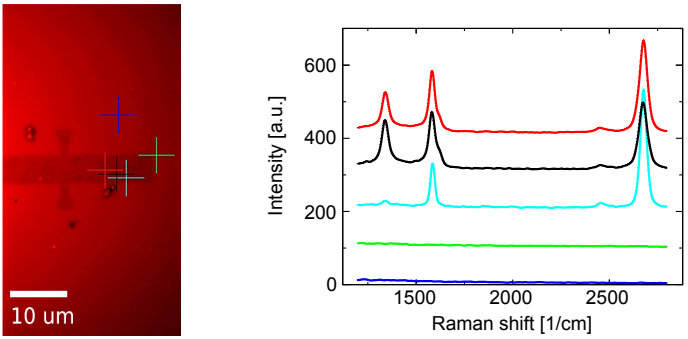

Figure 3.7: Raman spectra of graphene at different locations. Left, a detail of a graphene strip on a SiO_2 substrate (colors have been digitally modified to improve apparent contrast). Right, Raman spectra collected over the sample on the left, color-coded accordingly (offset in intensity, for clarity). The features in the Raman spectra vary significantly depending on location of sampling (for instance, confront the black curve with the cyan one). To better monitor these inhomogeneeties, several spectra can be collected to produce maps, see Figure 3.8.

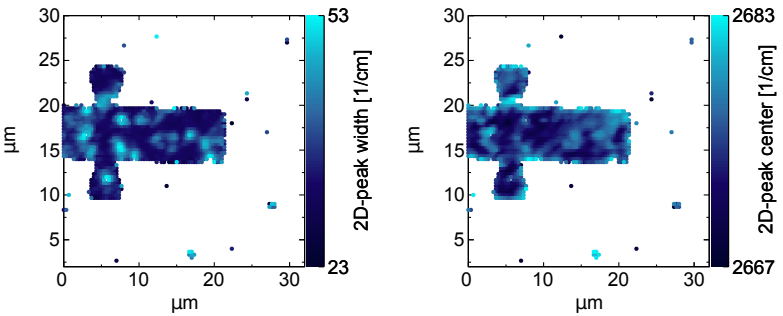

Figure 3.8: Spacial dependence of the Raman signal for a typical CVD graphene sample. The graphene in Figure 3.7 is scanned in a raster fashion and the 2D peak is fitted at each location. Width (left) and center (right) of the peak are mapped to their in-plane coordinates to produce these images. Significant variations can be appreshiated over a length of ~10 µm.

We use a *WiTec alpha300* confocal microscope with a laser wavelength of 532.2 nm. The equipment enables us to either collect a signal at a given location or automatically scan the sample and associate the spectra at each sampling position. Individual features in the signal (*e.g.* the intensity, position or width of a Lorentzian fit to a pre-selected peak) are then associated to the sampling position and plotted in 2D color maps, generating images like the ones in Figure 3.8. We checked the capabilities of this instrumentation on our samples and observed the following:

1. On a qualitative level, the expected features (D, G and 2D) are clearly visible: we can use Raman maps to determine areas covered by graphene and areas free from it (see Raman maps in Figure 3.8), particularly when monitoring the effectiveness of etching and annealing processes.
2. Distribution of key values (*e.g* mean and width of a given feature) within a sample is large. Histograms of the position of, say, the G peak measured across an area of the order of 10 μm^2 are quite broad ($\pm$ 2 cm^{-1}, see histograms in Figure 3.9). If we take the model in [140] to estimate the carrier density in graphene and consider a G peak at 1580 $\pm$ 3 cm^{-1} we can only say that $n \sim 10^{-12}$ cm^2/Vs, but this is too broad of a range to tell us where V_{Dirac} will fall in our Field Effect Transistor characterization (see section 3.4).
3. Comparing between samples is challenging. The position of a selected feature (not only its intensity) along the wavelength axis is significantly dependent on the distance d_{ob} between the objective lens and the graphene. We show in Figure 3.9 how the position of the G peak shifts easily $\pm$ 3 cm^{-1} for small changes in d_{ob}. These changes in d_{ob} are comparable to the precision of the focusing procedure[3] (~0.2 µm), therefore different measurement sessions can yield significantly different results (even on the same sample), if a precision $\lesssim$ 3 cm^{-1} is required.

From these observations we conclude that analyzing the Raman spectra is not a sufficiently accurate method for us to extract the carrier density in graphene or the absolute number of layers. That said, relative changes for a fixed d_{ob} are still visible and give us an assessment of the homogeneity of the graphene.

[3]The focusing procedure is based on maximizing the intensity of the Raman signal, not the position of the peaks.

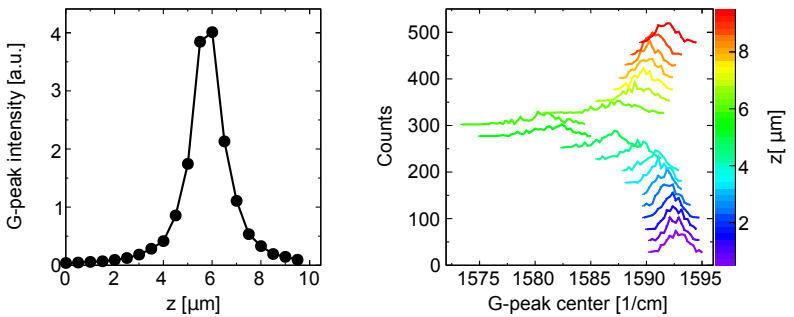

Figure 3.9: Left, the dependence of the intensity of the signal on the distance d_{ob} between the graphene and the microscope (0.5 µm steps, offset for clarity), where the *z*-axis is taken to be the one perpendicular to the graphene surface, with an arbitrary zero value close (*i.e.* within a 10 µm distance) to the focal distance. We determine the focal distance by maximizing the intensity as a function of *z*. Right, histograms for the measured position of the G peak over the same sample as in Figure 3.7 (offset for clarity). We fix the *z*-value, map the graphene over a given area and measure the position of the G-peak. Due to inhomogeneities over the graphene, we collect a distribution of G-peak values (typically a ~4-cm^{-1} wide gaussian distribution). The procedure is repeated for different values of *z* (color scale).

For instance, in Figure 3.10 we show the Raman data of a CVD graphene sample after an oxygen plasma etching (50 W, 10 sccm O_2 at 1 mbar, 240 s). Mapping the 2D Raman peak next to the edge of the etched graphene reveals the poor effectiveness of this method: small graphene islands are still traceable where none was expected, despite the prolonged etching time. The etching strategy can thus be disregarded as not effective.

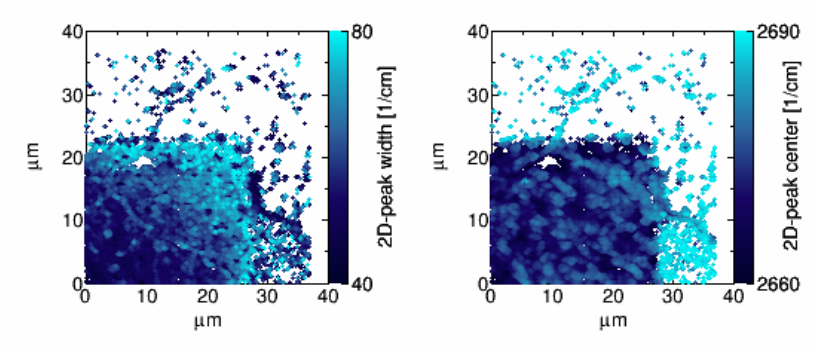

Figure 3.10: Raman etching maps for assessing the effectiveness of an oxygen plasma etching step. The 40 µm × 40 µm area is from a CVD graphene sample on a SiO_2 substrate. The bottom-left corner (first ~ 25 µm × 20 µm) is covered by an EBL-defined PMMA mask before exposing the sample to an O_2 plasma (50 W, 10 sccm O_2 at 1 mbar, 240 s). After the etching step, the PMMA is removed and the Raman data is collected. A large number of graphene islands is found where none was expected, along with poorly defined edges of the covered area. Both these findings indicate a poor effectiveness of the etching step.

Raman can also reveal alterations in the graphene from exposure to long annealing times. Exposure to temperatures ~ 100 °C is a common technique to remove resisit residues from lithographic treatments [72,141] and Raman data like the one in Figure 3.11 can be used to monitor the possible degradation of the specimen.

Raman Cleaning

Our experience with the Raman equipment ocasionally extended beyond the analysis of peak positions and intensities. In some fabrication processes involving an etching step to shape the CVD graphene, we would find a uniform layer

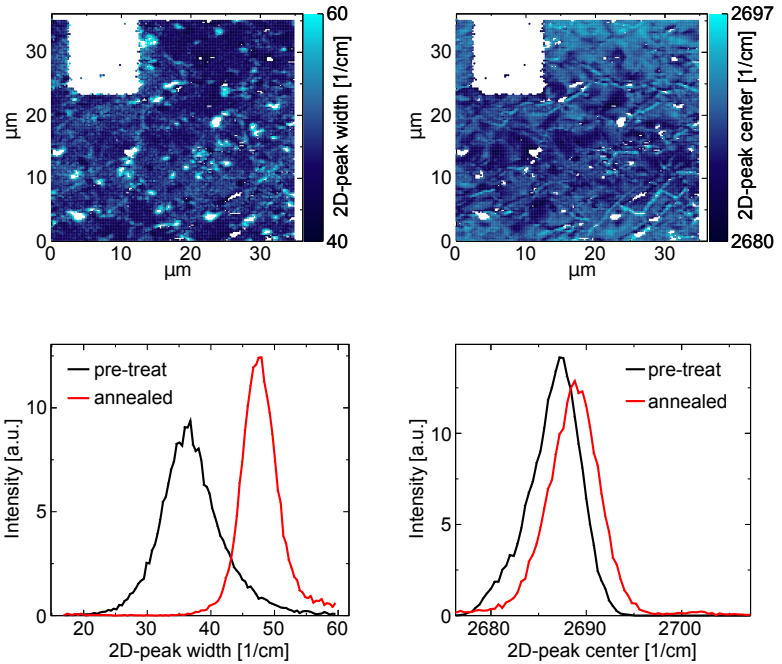

Figure 3.11: Raman mapping after an annealing step at 500 °C in O_2 atmosphere for 5h, illustrating the width (left) and center (right) of the 2D-peak. Bottom, histograms of the data displayed in the maps above. We can see from the corresponding histograms (bottom) how the annealed sample shows significantly wider (*i.e.*, larger width values) 2D features, suggesting this particular annealing could be damaging - rather than improving - the quality of the graphene.

of residues left over the un-etched graphene, appearing as a blue/green film in an optical microscope (see Figure 3.12).

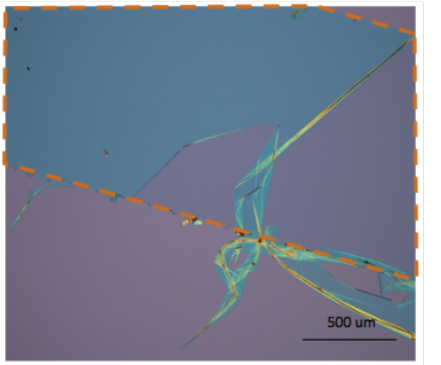

Figure 3.12: Optical image showing the residues left on graphene after an etching step. The substrate is SiO_2 and the area enclosed by the dashed line is covered by graphene.

As this is not a broadly reported issue in the graphene literature, we investigated the matter a little further. Supposing this was regular resist residue, we performed a few standard tests.

- Thermal annealing: PMMA is known to decompose under prolonged annealings at temperatures higher than 200 °C. However, the uniform film in Figure 3.12 would stand annealing procedures at high temperatures (> 300 °C) in vacuum conditions.
- O_2 plasma: this method resulted in effective removal of the film, with the side effect of etching (or at least damaging) the graphene as well, as we verified with Raman spectroscopy.
- Sonication: upon immersion in a ultrasonic bath, the film would "liftoff" from the graphene. However, CVD graphene transferred on SiO_2 is poorly attached to its substrate and, along with the green film, sonication will easily detach the graphene, too.

We collected Raman spectra over the areas covered by the film. Curiously, the spectrum would change in time while sampling over the same location. At first a broad background would appear, superimposed to the expected Raman signatures for graphene, but upon subsequent exposures to the laser the intensity of the background would diminish, particularly when using a relatively

intense power output (20 mW, compared to a typical 0.1 mW power output). We have measured this systematically: in Figure 3.13 we show the magnitude of the background as a function of sampling iteration (over the same location). A monotonic decrease clearly emerges, at virtually all wavelengths. Moving to a different location the trend repeats: a large and broad background reduces in amplitude with increasing exposure to the laser light.

Traces left from the laser could be seen also in optical images, particularly with an intense laser output, as shown in Figure 3.13. Both individual spots and whole trails exposed to the scanning laser could be traced over the film in optical images. Notably, the exposed graphene would then show the original, pre-lithography contrast to the SiO_2 substrate. Based on the reduction of background in the Raman signal and the return to the original graphene/SiO_2 contrast, we referred to this procedure as laser-cleaning. Effects of the cleaning procedure were also detectable electrically, with a monotonic decrease in resistivity as larger areas of the graphene were scanned by the laser.

Narrowing down the options in the fabrication steps, we found the presence of the film to be a result of exposing the (thin) resist to ion milling for more than 30 s, a step which entered in the fabrication procedure for graphene etching. We also noticed that a thicker resist layer (*i.e.* thicker than 500 nm) would not leave the mentioned film after the ion milling.

The observations collected here suggest that during the ion milling step the first few nanometers at the top of the resist cross-link, forming the green film visible in Figure 3.12. PMMA is reported to behave as a negative resist for high dose exposure [142] and, although a direct comparison with electron-beam lithography setups is not straightforward[4], the phenomenology seems consistent. Upon irradiation, the resist hardens and looses its solubility in acetone. However, the organic layer will react with the oxygen in the atmosphere upon exposure to high temperatures (like in the laser-cleaning procedure) or to oxygen plasma. The relatively low acceleration voltage of the ion miller and the shorter penetration depth of ions compared to electrons make it for an inhomogeneous effective dose along the thickness of the resist, so that when thicker (> 500 nm) resist layers are used, the bottom part of it is not hardened and dissolves in acetone, with the hardened top layer “lifting off”.

[4]The acceleration voltage in EBL systems tends to be in the 10-100 kV range, while for the ion miller is in the 50-300 V. Moreover, energy losses from charged particles going through matter generally have a dependence on the mass of the particle, making a direct comparison between electron and ion irradiation more challenging

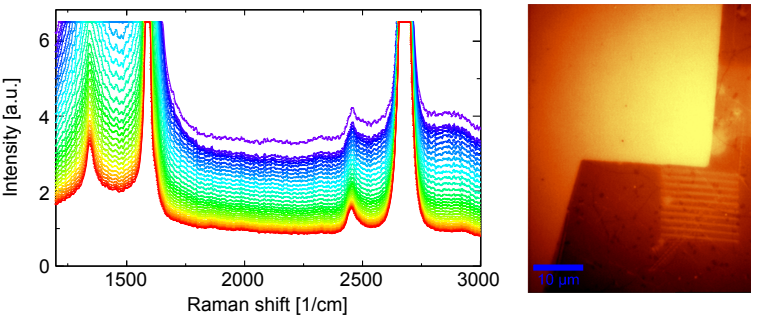

Figure 3.13: Left: Raman spectra over the same point at intervals of 20s. The average intensity diminishes with time (from blue to red curve). Right: optical image of a graphene structure (bottom right, darker color) on a SiO_2 substrate. After the Raman laser scan, traces are clearly visible over the graphene area.

Most notably, the graphene withstands the heat of the laser-cleaning. This is not to be taken for grated: the same procedure over a MoS_2 or Bi_2Se_3 sample burned the flake as well, along with the PMMA residues. To quantitatively understand the heating at which these flakes were exposed, one would need to estimate how much heat is retained by the flake and how much diffuses to the SiO_2 substrate. This level of understanding extends beyond the interest of this work, but it remains fascinating to notice that a monolayer material can survive 20 mW of power focused in ~ 1 um^2.

This understanding helped us in choosing a different etching technique for the fabrication procedure, namely reactive ion etching (RIE). After RIE processing and acetone cleaning, the samples did not show the residues depicted in Figure 3.12 and their Raman signal proved to be stable over time. We also note that the Raman cleaning method can be a powerful tool for local annealing of graphene devices. This is especially interesting for cases where an annealing in an oxygen-rich atmosphere would be the method of choice (for instance, in order to burn organic residues left over graphene after a lithography step), were it not for the likely deterioration of specific sections of the sample (for instance, the Co electrodes of a lateral spin valve). In these cases, a laser can be used for local annealing without deterioration of the most sensitive sections of the device.}{it can be a valuable tool for local annealing in micro-fabrication, as some materials of interest in this work (like Co, for instance) cannot stand

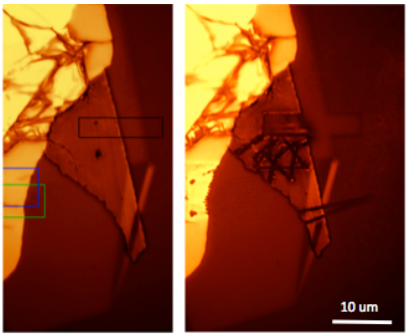

Figure 3.14: A Bi_2Se_3 flake before (left) and after (right) exposure to the Raman laser, under the same conditions of Figure 3.13. It is evident how the flake cannot withstand the power from the laser. The black box highlights a hole area scanned by the laser.

oxygen-rich atmospheres at high temperatures without degrading.

3.4 Electrical characterization

We include here some general electric characterization performed most commonly on our graphene-based devices: more specific details will follow in the next chapters, according to the particular cases of study.

Equipment

The electrical characterization reported in this work has been performed with one of the following sets of equipment:

- *Lakeshore* Probe Station (~10^{-5} mbar, typically at room temp) with a Keithely 4200 Semiconductor Characterization System electronics (sub-femtoamp resolution) connected via triax cables.
- Pysical Properties Measurement System (PPMS) from *Quantum Design Inc.* (~10 mbar, temperature varying in the 2-300 K range (liquid-He cryostat), magnetic field up to 9 T), with a Keithely 6221 AC and DC current source, Keithely 2182 Nanovolt meter and (optionally) Keithely

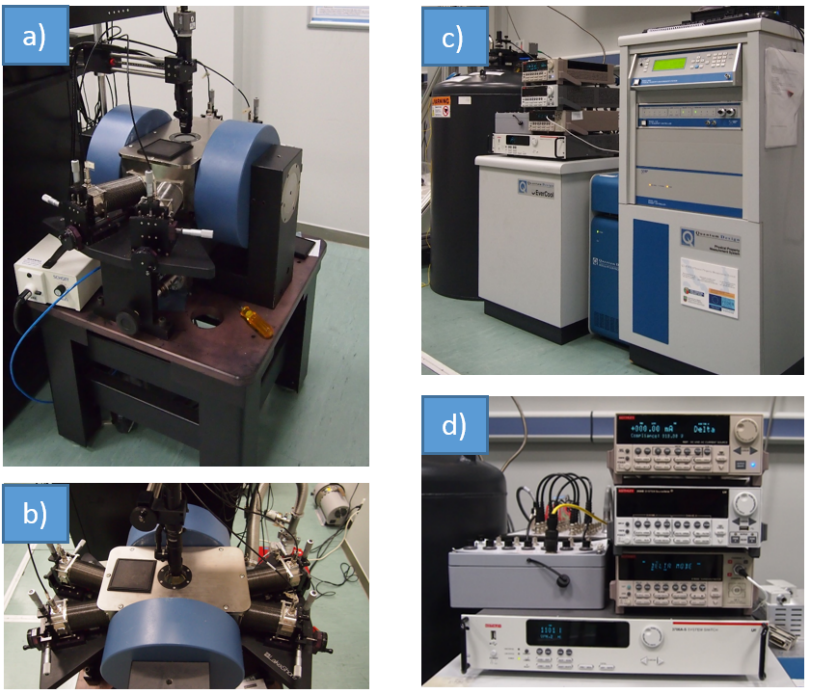

Figure 3.15: Equipment for the electrical characterization. a) and b) *Lakeshore* Probe Station, side and top view respectively. c) Pysical Properties Measurement System (PPMS) from *Quantum Design Inc.*. d) Example of Keithley moduli for sourcing and/or measuring electrical currents and voltages.

2636 Dual-channel System SourceMeter, coordinated by a custom made Labview interface. The samples are mounted on a sample stage that allows for eight different electrical connections, *via* copper wires bonded to the macroscopic part of the sample by cold indium pressing. Once in the PPMS, the sample stage can be controllably rotated around an axis perpendicular to the direction of the magnetic field.

Particularly for devices with low signal-to-noise ratio, we used a sampling technique implemented in the electronic equipment named *Delta Mode* [143], which works by combining the capabilities of the 6221 module as a current source and the 2182 module as a nano-voltmeter. The working principle is to rapidly alternate the sign of the output current and measure the response in voltage from the device, to filter out systematic errors in the readings. Figure 3.16 shows a few details of the measurement cycle: while the 6221 module alternates the output current between the values I_{High} and I_{Low}, where I_{High} = - I_{Low}, the module 2182 measures the voltage at the terminals of the device. One *Delta cycle* is complete with three voltage readings, and the appropriate average is computed in order to yield one *Delta reading* V_Δ (see Figure 3.16).

This procedure is very useful in removing any systematic error, that is contributions to the measured voltage that are not dependent on the polarity of the current, such as, for instance, offsets from contact-potentials. The i-th voltage reading $V_i(I)$ from the device will be the sum of the signal, $V_{\mathrm{DUT}}(I)$, a random noise term $V_i^{\mathrm{ran}}(I)$ and a systematic (*i.e.* not dependent on the applied current I) term V^{sys}. One Delta reading will then result in

$$\begin{aligned} V_\Delta &= \frac{V_i(I) + 2V_j(-I) + V_k(I)}{4} \\ &= V_{\mathrm{DUT}} + \frac{V_i^{\mathrm{ran}}(I) + 2V_j^{\mathrm{ran}}(-I) + V_k^{\mathrm{ran}}(I)}{4} \end{aligned}$$

where all systematic contributions are effectively cancelled out and the random ones are reduced by an arithmetic average. Notice that the Delta Mode approach will remove the systematic terms even when time dependent: as long as $V^{\mathrm{sys}}(t)$ does not depend on the polarity of the current I and it varies slowly in time compared to the Delta cycle period, V_Δ will be free from systematic errors. This is a very effective method for improving the quality of the measurements and a simpler one than more traditional lock-in filters.

The procedure is then repeated a number of times, for statistical averaging. We will refer to one *measurement* y_i as to the averaging of a number of Delta readings, and to *counts N* as to how many readings we have been averaging over:

$$y_i = \frac{1}{N} \sum_{j}^{N} V_{\Delta_j}$$

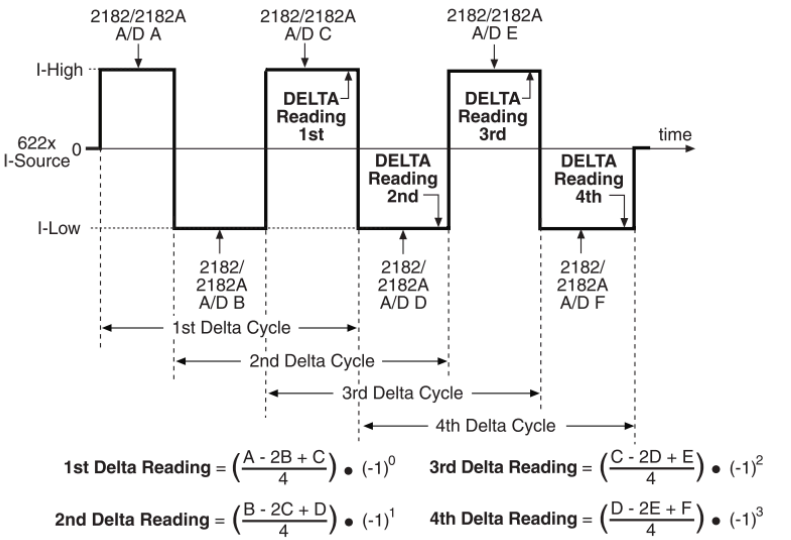

Figure 3.16: Illustration of the measurement cycle for the Keithley Delta Mode. Image adapted from [143].

Field Effect measurements

One of the most common setups for graphene-based electronic devices is the Field Effect Transistor (FET) device, where the graphene lies on a plane ~10-100 nm apart from a gate electrode, with dielectric material filling the gap in a layered geometry. Forcing a voltage difference between the gate and the graphene changes the carrier density (and thus its conductivity) in the later, as introduced already in Chapter 1.

In our case, our devices were composed of CVD graphene transferred on 300 nm thick SiO_2 substrate, grown on highly doped Si which we used as a gate electrode. Figure 3.17 shows the typical modulation of the graphene's resistivity as a function of the applied gate voltage, where we can see the improvements in measuring with a 4 point method compared to a 2 point one. We also note that the graphene is quite doped compared to an ideal sample: we find the maximum of the graphene resistance at a gate voltage of 40-60 V (as opposed to 0 V) and a broad FWHM (10-20 V on the gate axis), sign of a relatively low mobility compared to exfoliated graphene. The values we typically extract are ~ 1000 $cm^2V^{-1}s^{-1}$.

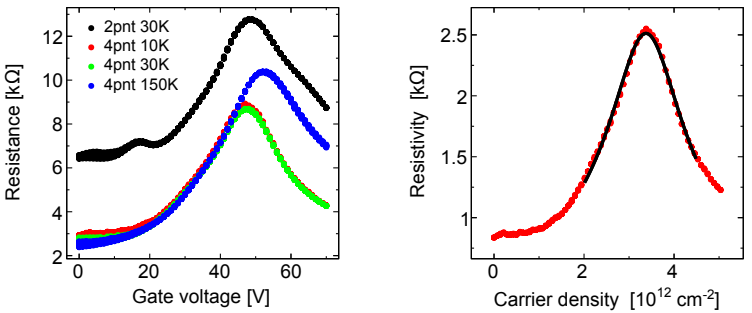

Figure 3.17: Field Effect measurements on a graphene device. Left, dependence on temperature and type of measurement (4 point *versus* 2 point). Right, the same data (4 point, 10 K) fitted to Eq. 1.6 yields a mobility μ_c of 3000 $cm^2V^{-1}s^{-1}$ and a residual carrier density n_{imp} of 8×10^{11} cm^{-2}.

Magnetoresistance measurements

Along with FET measurements, magnetoresistance (MR) measurements are another common way to characterize graphene samples, particularly through the Hall effect. Graphene devices are fabricated in a characteristic Hall-bar shape as the one sketched in Figure 3.18, where a voltage V_{xy} is measured transverse to an electrical current I, as a function of an external magnetic field B. As a charge carrier flows though the conductor with a velocity $\mathbf{v}$, its direction is stirred by the Lorentz force $\mathbf{F} = q(\mathbf{E} + \mathbf{v} \times \mathbf{B})$: on the scale of the device, this results in an asymmetric charge density in the direction transverse to both $\mathbf{I}$

and $\mathbf{B}$. An electric field arises from this accumulation, opposing further charge separation and establishing a steady-state electrical potential V_{xy}. A linear relationship between V_{xy} and B is found:

$$\frac{V_{xy}}{I} = -\frac{1}{nte}B \tag{3.1}$$

where n is the carrier density, t the thickness the conductor and e the fundamental charge. By using $\sigma = ne\mu$ we can then fit the Hall measurements and extract the mobility $\mu = \frac{1}{\rho}|\frac{1}{ne}|$. The Hall measurements can also be performed as a function of the backgate voltage V_g, which will change the carrier density in the graphene through Field Effect. The change in n then shows in the Hall measurements as a change in slope of the $V_{xy}(B)/I$ data and we can see the change from an electron- to a hole-type of carriers in the change of the slope of the data. (see Figure 3.18). Figure 3.18 shows the result of a Hall measurement for the graphene device at different values of gate voltge V_g. From these measurements we extract a carrier density n of the order of 10^{12} cm^{-2} (*i.e.* mobility $\sim 10^3$ cm^{2}V^{-1}s^{-1}).

If on the one hand the order of magnitude for the carrier density is the expected one, however, on the other we can see how the gate dependence is not, with smaller values of n at V_g = 60 V than at 48 V ($V_{xy} \propto 1/n$). In addition, from Eq. 3.1 we expect to measure $V_{xy} = 0$ at zero magnetic field, which is never the case. Both these two unexpected behaviors (the gate dependence and the offset of the data) are ascribable to the electrostatic inhomogeneity in the graphene layer. The presence of trapped charges near the surface of the substrate accounts for variations in the local carrier density of the graphene [103], which our voltmeter can not distinguish from the ones generated via Hall Effect. These measurements attest, once again, the high sensitivity of graphene to electrostatic doping.

Along with the Hall effect, which is measured in the direction transverse to the current, in graphene samples we expect to measure MR signals in the longitudinal direction as well, particularly through weak localization. Weak localization has been reported in graphene samples and, although we will come to a more detailed description in the last chapter of this work, let us briefly mention its phenomenology here for completeness. Figure 3.19 shows an example of the typical magnetoresistance arising from weak localization physics: the resistivity of the graphene changes upon applying a magnetic field perpendicularly to the conductor's plane, irrespectively of the sing of B. Typically the MR from

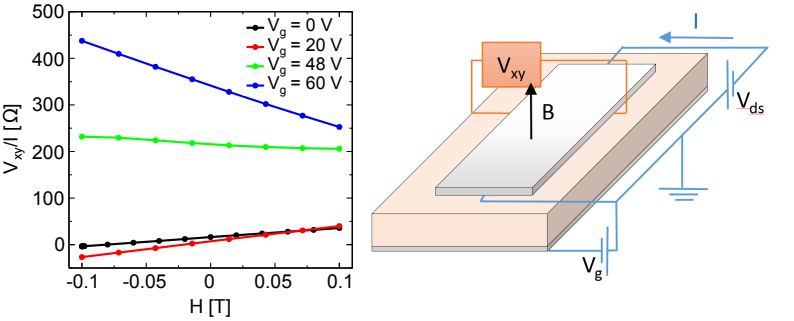

Figure 3.18: Hall effect from CVD graphene on SiO_2 for the same device as in Figure 3.17. Different colors correspond to different backgate voltage V_g. Measurements done at 10 K.

weak localization will increase with lower temperatures and with lower mobilities, but regular values of $\Delta\rho/\rho$ will be ~0.1-1% at magnetic fields of about 0.1 T.

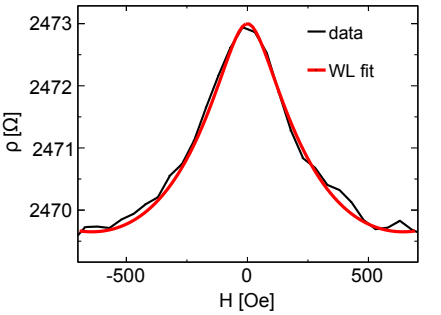

Figure 3.19: Dependence of the graphene's resistivity on an out-of-plane magnetic field. Measurement done at 4K.

Part II

Non-Local spin valves on CVD graphene

4 Spintronics

Spintronics is a large field, with flourishing results both in industry and academic fields, exploiting the magnetic moment of electrons for the manipulation and storage of information in solid-state devices. This chapter will focus on currents of spin-polarized electrons: we will introduce the two-currents model, the injection process, the principal mechanisms for spin relaxation in graphene and two device geometries used for the study of spin transport in graphene.

4.1 Spin polarized currents in diffusive systems

The idea that the current in metals could be spin-polarized is nearly a century old.

As early as in 1936, Mott [144] had a remarkable insight while examining ferromagnetic metals. He suggested that the change in resistance with temperature for transition metal ferromagnets could be explained considering the current as "made up of two parts, contributed with electrons with the two spin directions". The same point is typically visualized with figures such as Figure 4.1, which depicts a simplistic density of states as a function of energy, $g(E)$, for a ferromagnetic metal. For temperatures T smaller than the Curie temperature T_C, $g(E)$ is different for majority and minority spins, with two important consequences:

- the total number of electrons with spin up polarization differs from the

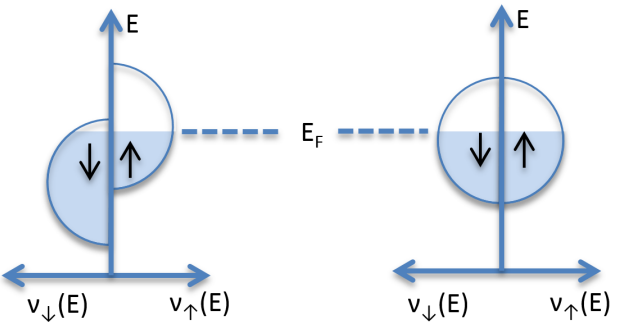

Figure 4.1: Density of states as a function of Energy for free electrons in a ferromagnetic (left) and a non-magnetic conductor (right).

number of spin down one, which accounts for the spontaneous magnetization of the ferromagnet;

- the density of states at the Fermi level, $g(E_F)$, is different for the two different populations. It is then natural to use the Einstein relation $\sigma = e^2 D g(E_F)$ to define a spin-dependent conductivity for each spin population[1]:

$$\sigma_{\uparrow,\downarrow} = e^2 D g_{\uparrow,\downarrow}(E_F)$$

where e is the elementary charge and D the diffusion constant.

The idea to model the transport as happening through two independent channels in parallel is often called the "two current model", and the formalism to describe it has been developed in detail in Ref. [145]. As discussed there, if scattering between the different spin populations is rare compared to momentum scattering, one can consider the conduction as happening through two channels in parallel, writing $\sigma = \sigma_\uparrow + \sigma_\downarrow$ and $g = g_\uparrow + g_\downarrow$.

This approach predicts that it is possible to distinguish the relative magnetic orientation of two ferromagnets by electrical measurements. Figure 4.2 depicts the basic idea behind a magnetoresistance measurement: as the density

[1] If scattering between spin population is rare compared to momentum scattering

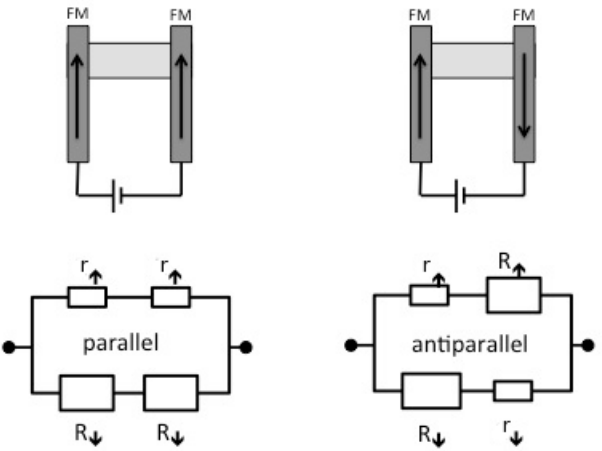

Figure 4.2: Cartoon depicting the changes in resistance of an electronic device upon change of the relative orientation of the electrodes' magnetization.

of states $g_{\uparrow,\downarrow}(E_F)$ is spin-dependent, an electron passing through a ferromagnetic lead will encounter a larger (R) or smaller (r) resistance depending on the relative orientation of its own spin to the electrode's magnetization. If we consider the system as the parallel of two conduction paths, one for electrons with spin up and one for electrons with spin down, it is then clear that the parallel or anti-parallel orientation of the ferromagnetic leads will lead to different values of resistance, $4rR/(2R + 2r)$ in the first case and $(r + R)/2$ in the second. Thus, a change in the magnetic configuration of the leads can be detected as a change in the whole device's resistance.

This simple picture, of course, applies if the spin of the electron is conserved from one electrode to the other. This is typically the case in local spin valves, where two conductive ferromagnets (FM) are separated by a thin non-magnetic layer (NM), to enable individual switching of the electrodes' magnetizations. The FM-NM-FM system typically comes in two geometries: a so called *vertical* one, where the layers are stacked one on top of the other, and a *lateral* one, where the NM material is shaped into an elongated channel, connecting the two FM leads on the surface of a supporting substrate. In both cases the goal is to have a measurable spin-polarized current traveling through a NM material,

where by definition the ground state is a not-spin polarized one. This introduces us to the topic of injection and detection of spin polarized currents.

4.2 Injection and Conductivity mismatch

Experimentally, spin scattering typically happens in the nm scale for ferromagnetic materials and in only few non-magnetic materials approaches micrometer lengths [146]. The more common picture, then, considers the population of conduction electrodes, instead of the single carriers, as spin-polarized (to a degree P, with $0 \leq P \leq 1$) in the injector electrode. The contrast in spin polarizations between the two ferromagnetic electrodes, mediated by the non-magnetic channel, is what originates the magnetoresistive signal.

To be more quantitative, it is useful at this point to introduce two different electrochemical potentials, $\mu_\uparrow$ and $\mu_\downarrow$, for the two spin-populations. From the local version of Ohm's law we get

$$j_{\uparrow,\downarrow} = -\frac{\sigma_{\uparrow,\downarrow}}{e}\frac{\partial \mu_{\uparrow,\downarrow}}{\partial x}$$

Under the same approximation, one can define the transport by the spin current density $j_S = j_\uparrow - j_\downarrow$ and the charge current density $j = j_\uparrow + j_\downarrow$. In a ferromagnet, $\sigma_\uparrow \neq \sigma_\downarrow$ giving a non-zero spin polarization P:

$$P \overset{\text{def}}{=} \left|\frac{j_\uparrow - j_\downarrow}{j_\uparrow + j_\downarrow}\right| = \left|\frac{\sigma_\uparrow - \sigma_\downarrow}{\sigma_\uparrow + \sigma_\downarrow}\right|$$

Typical values for P in transition metal ferromagnets are $P \approx 0.2{-}0.6$, whereas the bulk of a NM channel has $P = 0$. This discrepancy suggests that an accurate description of the spin transport sees three distinct regions, the bulk FM, the bulk NM and the FM/NM interface. In the proximity of the FM/NM interface, a flow of spin-polarized current from FM to NM will generate a non-equilibrium spin accumulation into the NM, which will diffuse into the bulk of the NM, decreasing with a decay length λ_s^N. The non-equilibrium spin population can also diffuse back into the FM, so that the spacial dependence of $\mu_s = (\mu_\uparrow - \mu_\downarrow)/2$ across the interface typically has the shape shown in Figure 4.3.

The evolution of the spin population is described by the Bloch equation [149]

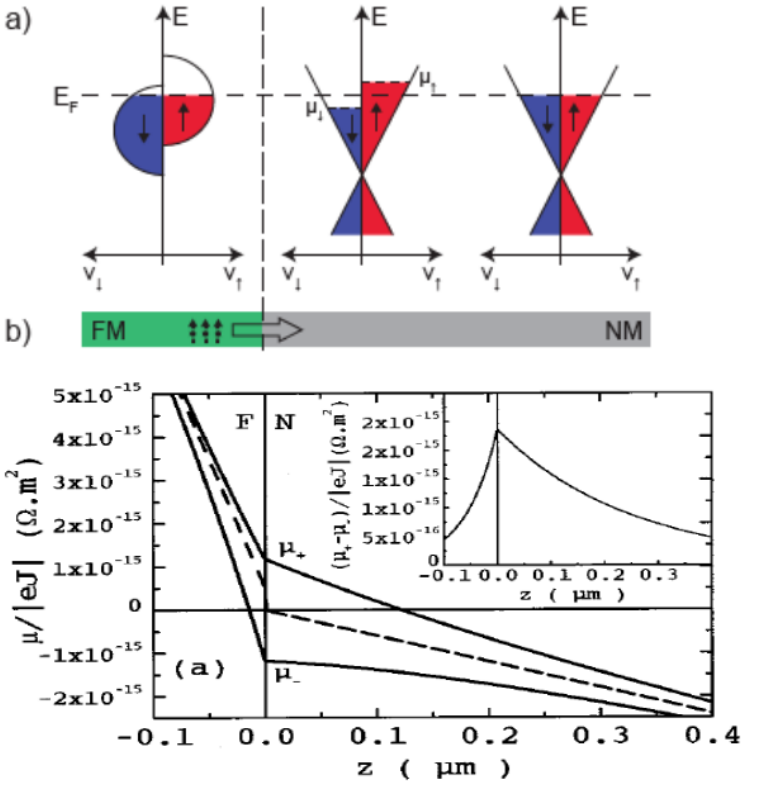

Figure 4.3: a) Concept of spin injection at the interface between a FM and a NM, where the spin population in the NM is changed close to the interface when an electron current is flowing from the FM into the NM. Image adapted from [147]. b) Variation of the electrochemical potentials $\mu_\uparrow$ and $\mu_\downarrow$ (labeled as $\mu_+ - \mu_-$ in the figure) as a function of the lenght-dimension z at a Co/Cu interface (transparent interface). The inset shows the variation of the spin accumulation parameter, μ_s as a function of z. The quantitative example of a Co/Cu interface has been adapted from [148], but the qualitative features are general for a transparent FM/NM junction.

$$\frac{\mathrm{d}\boldsymbol{\mu}_s}{\mathrm{d}t} = D\nabla^2\boldsymbol{\mu}_s - \frac{\boldsymbol{\mu}_s}{\tau_s} + \boldsymbol{\omega}_L \times \boldsymbol{\mu}_s$$

where τ_s is the spin relaxation time, D the diffusion constant and $\boldsymbol{\omega}_L = \frac{g\mu_B}{\hbar}\mathbf{B}$, g being the g-factor, μ_B Bohr's magneton, $\hbar$ Planck's constant and $\mathbf{B}$ the magnetic field. Bloch's equation captures the spin diffusion, relaxation and precession around a magnetic field in a very general synthesis. The boundary conditions, however, will be dependent on the specific system, particularly with respect to the spin polarization of the carriers at the interface. Intuitively, the value of μ_s at the point of injection in the NM (and the corresponding spin polarization, which we will refer to as P_N) will depend on the polarization of the ferromagnet and on the spin scattering that the interface might introduce. Nonetheless, even with an ideal polarization $P = 1$ and no spin scattering at the interface, the polarization P_N can vanish simply for the particular electrical resistances involved in the device. This is called the conductivity mismatch problem.

Conductivity mismatch

The conductivity mismatch is a fundamental problem when considering spin injection. Raised in the context of spin injection into semiconductors [150,151], and still relevant to date for injection in graphene [152,153], this issue alone can make the difference between a measurable signal and a not working device. The core intuition here is that a non-equilibrium spin population at the FM/NM junction is not bound to distribute evenly around the interface. The spin accumulation will be enhanced on the one side or the other, depending on the relative spin-resistances of the two materials, which will control the diffusion of the population in the one direction or the other.

As showed in Ref. [148], the introduction of a resistive interface barrier provides a way to control the polarization P_N in the channel. Given a ferromagnet with a bulk spin polarization P_F, an interface of finate resistance R_I and polarization P_I, we have

$$P_N = \frac{P_F R_F + P_I R_I}{R_F + R_N + R_I} \tag{4.1}$$

where we have introduced the spin resistances R_F and R_N of the ferromagnetic and non-magnetic conductors. The general form of the spin resistance

is $R_{spin} = \lambda_s^2 \rho / \mathcal{V}$, where $\mathcal{V}$ is the volume over which a net spin population can diffuse in the material. That is to say that, if we imagine a net spin population at the interface of two materials, there will be a larger diffusion into the one with the lower spin resistance. For FM electrodes, λ_s is typically smaller than their thickness [154], making the spin current in the FM decay very close to the interface, over a volume $w_N w_F \lambda_s^F$, with $w_{F/N}$ the width of the FM/NM channel. For NM electrodes, and particularly for graphene, λ_s tends to be larger than the thickness and the net spin population will diffuse over a volume $w_N t_N \lambda_s^N$, with $t_{F/N}$ the thickness of the metal. Therefore we obtain Eq. 4.1 with $R_N = R_g = \rho_{sq} \lambda_s^N / w_N$ and $R_F = \rho_F \lambda_F / w_N w_F$.

From these relations it is straightforward to see how crucial the role of the interface resistance is. If we suppose a transparent contact, for instance, we obtain $P_N = P_F R_F / (R_F + R_g)$, which vanishes for $R_F / R_g \to 0$: should it simply be the case that the spin resistance of the ferromagnet is much larger than the one of the graphene, there would be no spin injection in the channel. Note that these are all intrinsic quantities of the materials involved, with the only exception of the geometry of the contact area. This implies that, from a fabrication point of view, the only room for optimization is given by one of the lateral dimensions of the ferromagnetic contact, which typically happens to be constrained by magnetostatic or lithographic requirements.

Introducing an interface barrier of finite resistance R_I, with $R_I > R_g \gg R_F$, yields $P_N \approx P_I$ and enables the accumulation of a net spin population in the NM. As discussed in [148], the value of R_I can be optimized to maximize the measured spin signals, depending on the particular geometry employed.

Mechanisms of spin relaxation

In this section we will introduce two spin relaxation mechanisms, Elliott-Yafet (EY) [155,156] and the D'yakonov-Perel' [157]. Although spin relaxation in graphene is still a matter of debate, EY and DP are the most likely processes behind it. For more thorough information, we recommend the reader to reviews such as [158].

Elliott-Yafet spin relaxation

The Elliott-Yafet mechanism is the most commonly found in metallic systems, and typically in systems with spacial inversion symmetry. The key idea here is

that spin scattering takes place *during* momentum scattering events, through spin-orbit coupling. The larger the number of scattering events, the larger the dephasing of the spins: the spin relaxation time and the momentum relaxation time grow proportionally, $\tau_s \propto \tau_p$. Sources of such scattering events could be impurities, phonons, boundaries, each mechanism leading to a different τ_s/τ_p ratio.

D'yakonov-Perel' spin relaxation

The D'yakonov-Perel' relaxation mechanisms is based on the presence of spin-orbit (SO) fields in the material through whitch the spins are diffusing. The two authors were considering solids like GaAs and InAs, which lack a center of inversion symmetry. As a result of the SO fields, the spins travel through a system with intrinsic magnetic fields, precessing as they diffuse. As momentum scattering occurs, the direction of the carrier changes, and so does the direction of the magnetic field acting on it. In this picture, the coherence among the spin population is lost *in between* momentum scattering events, as the momentum relaxation will drive the randomization of the spin phases. The key measurable result is that the spin relaxation time τ_s is $\propto 1/\tau_p$

4.3 Measurement of spin diffusion in non-magnetic materials

The focus of the previous section has been on the fundamental physics behind the dynamics of a spin polarized population of carriers diffusing near a FM/NM interface. We have described the injection, accumulation and relaxation of a non-equilibrium spin population in a non-magnetic material, taking minimal assumptions about the geometry of a potential device and on the measurement techniques necessary to experimentally investigate this phenomenon.

We now turn our attention to a few common measurement techniques employed in the study of spin diffusion. The attention here is typically to characterize the spin transport properties of a non-magnetic material: the quantities of interest are, for instance, the intrinsic spin diffusion length λ_s and spin relaxation time τ_s of such material, where the least invasive techniques are generally the most appreciated ones.

Lateral spin valve

The simplest approach for an electrical measurement of λ_s, especially in the case of a 2D material like graphene, is to contact it with two ferromagnetic leads and study the magnetoresistance curves of such devices varying the distance in between such electrodes. Typically the ferromagnets are shaped into small widths, so to reduce the number of individual magnetic domains and enhance the overall polarization. In addition, care is taken so that the coercive field of each lead is unique, which can be achieved by use of different ferromagnetic materials (most commonly Co or NiFe) or by tuning the lateral dimensions of the individual contact. The magnetization of the leads is controlled by sweeping an external, in-plane magnetic field, so that the ferromagnets switch between a parallel and an anti-parallel orientation. If the spin polarization is preserved, the resistance of the whole device will change as it switches between the parallel and anti-parallel states. The advantage of a lateral geometry like the one in Figure 4.4 is then the possibility of measuring how the spin polarization is lost as the distance between the ferromagnets increases, an (almost) direct measurement of λ_s.

This type of measurement, however, can suffer from a few possible artifacts like Hall effects and anisotropic magnetoresistance effect [160], which might mask or even mimic the contributions from the intrinsic values of the NM. What ultimately these phenomena share is that the spin and the charge current are not separated from one another, so that it is not trivial to discern the signals coming from the first and the ones coming from the second.

The *non-local* geometry addresses precisely this point (see Figure 4.4). It is still a measurement of magnetoresistance, but now the NM is contacted with four leads, with the measurement circuit out of the current loop. At least two of the contacts must be ferromagnetic, so to act as the spin injector and detector, and the same magnetostatic considerations on the physical dimensions of these electrodes apply, just like in the local setup. The non-local geometry ensures that, at least to first approximation, all the electrical current is confined to one side of the NM, while the spin accumulation, which *per se* typically diffuses isotropically, is measured on the other side of the channel. This setup ensures that the signal coming from the spin accumulation is separated from the ones arising from charge transport.

The detector electrode, as a result of the spin accumulation in the channel, will see its electrochemical potential μ_2 shifting from zero, so that a measurable

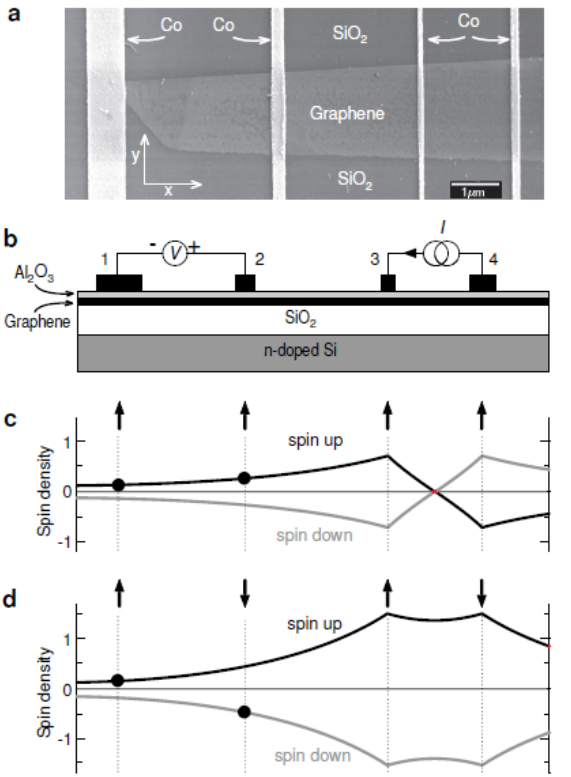

Figure 4.4: Lateral Spin valve. Spin transport in a four-terminal spin valve device. a) SEM image of a four-terminal single-layer graphene spin valve. b) The non-local spinvalve geometry. A current I is injected from electrode 3 through the Al_2O_3 barrier into graphene and is extracted at contact 4. The voltage difference is measured between contacts 2 and 1. c) Illustration of spin injection and spin diffusion for electrodes having parallel magnetizations. Injection of up spins by contact 3 results in an accumulation of spin-up electrons underneath contact 3, with a corresponding deficit of spin-down electrons. Owing to spin relaxation the spin density decays on a scale given by the spin relaxation length. A positive non-local resistance is measured. d) Spin injection and spin diffusion for antiparallel magnetizations. The voltage contacts probe opposite spin directions, resulting in a negative non-local resistance. Adapted from [159].

voltage V between the detector and the ground can be measured [161]:

$$V = I\frac{2R_N\left[P_{I1}T_{I1} + P_{F1}T_{F1}\right]\left[P_{I2}T_{I2} + P_{F2}T_{F2}\right]e^{-L/\lambda_N}}{[1+2(T_{I1}+T_{F1})][1+2(T_{I2}+T_{F2})] - e^{-2L/\lambda_N}} \tag{4.2}$$

$$T_{\gamma\delta} = \frac{1}{1-P_{\gamma\delta}^2}\left(\frac{R_{\gamma\delta}}{R_N}\right)$$

where $P_{\gamma\delta}$ and $R_{\gamma\delta}$ are the previously introduced polarization and spin resistance of FM and interface with $\gamma = F$ and $\gamma = I$ respectively (see Eq. 4.1), and the indexes $\delta \in \{1,2\}$ distinguish between injector and detector electrode.

A few approximations will bring us a far way. First, we consider the two FM electrodes as made of the same material, along with the two interfaces being identical as well: this removes the δ distinction. Secondly, we consider the two cases of transparent and tunneling contacts.

For the case of resistive interface $R_I \gg R_N \gg R_F$, the expected non-local signal R_{NL} is [149]:

$$R_{NL} = \frac{V}{I} = \pm\frac{1}{2}P_I^2 R_N e^{-L/\lambda_N} \tag{4.3}$$

where L is the distance in between the electrodes. This is arguably the most intuitive picture for the NLSV: the signal depends on the spin injection and detection efficiency ($\propto P_I^2$) and it exponentially decreases with L/λ_N. The conductivity mismatch is completely alleviated by the highly resistive contacts.

In the opposite case of a transparent interface $R_I \ll R_F \ll R_N$, we find

$$\Delta R_{NL} = \frac{4P_F^2 R_N}{\left[2+\frac{R_N(1-P_F^2)}{R_F}\right]^2 e^{L/\lambda_N} - \left[\frac{R_N(1-P_F^2)}{R_F}\right]^2 e^{-L/\lambda_N}}$$

Considering typical values from our particular graphene spin valve devices, we find

$$\frac{R_N(1-\alpha_F^2)}{R_F} \approx \frac{R_N}{R_F} \approx 5\cdot 10^3 \rightarrow \Delta R_{NL} \propto \frac{1}{e^{L/\lambda_N} - e^{-L/\lambda_N}} \tag{4.4}$$

It is Interesting to notice that Eq. 4.2 holds a formidable number of quantities, each of which could in principle be extracted from the fit of a non-local spin valve measurement. However, if the interest is solely on extracting λ_N, then both Eq. 4.3 and Eq. 4.4 offer a much more straightforward solution.

Hanle effect

The Hanle effect is the modulation of a spin-valve signal with the intensity of an external magnetic field. It is a manipulation of the net spin population in the channel, between injector and detector: if up to this point the focus has been on injection and detection, now the attention shifts to the dynamics in the channel, an particularly in the presence of an external magnetic field.

The typical Hanle experiment sees a lateral spin valve, most often in a non-local geometry, where an external magnetic field is first used to magnetize the electrodes in the plane of the sample and eventually leaves the magnetization of the leads at their remanent value. The (non-local) spin signal is then recorded as a function of an *out of plane* magnetic field $B_\perp$. As introduced earlier, the propagation of the spin signal from injector to detector, the diffusion, relaxation and precession around a magnetic field of the net spin population $\boldsymbol{\mu_s}$, is described by the Bloch equations [149]:

$$D\,\nabla^2\boldsymbol{\mu}_s - \frac{\boldsymbol{\mu}_s}{\tau_s} + (\boldsymbol{\omega}_L \times \boldsymbol{\mu}_s) = \frac{\mathrm{d}\boldsymbol{\mu}_s}{\mathrm{d}t}$$

where D is the diffusion constant, τ_s is the spin relaxation time and $\boldsymbol{\omega}_L = g\mu_B\mathbf{B}/\hbar$ is the Larmor frequency for the precession of the spins about a magnetic field $\mathbf{B}$. For the steady state and $B = 0$ case, we retrieve the exponential decay $\mu_s \propto e^{-x/\lambda_s}$, where $\lambda_s = \sqrt{D\tau_s}$. For $\mathbf{B}\cdot\boldsymbol{\mu}_s \neq 0$, the spins injected in the channel precess as they are diffusing, which results in a dependence of the non local signal R_{NL} on the intensity of B.

To be more specific, let us consider the example of spins propagating in a 1D conductor along, say, the x-direction. In a diffusive regime of transport, the time t it will take for an individual spin to travel the distance L in between the electrodes will be a random value with a broad distribution function $P(t) = \exp(-L^2/(4Dt))/\sqrt{4\pi Dt}$. During this time, each spin will precess an angle $\phi = \omega_L t$ around the direction of $B_\perp$. Eventually its projection along the magnetization of the second electrode will give rise to the non-local signal. As

this projection will have a sinusoidal dependence on the field and taking into account the relaxation of the spin population over time, we obtain

$$R_{NL}(B_\perp) = \pm \frac{P_I^2 R_N D}{w_N} \int_0^\infty \mathrm{d}t\, P(t) \cos(\omega_L t) \exp(-t/\tau_s) \tag{4.5}$$

Fitting this formula to the Hanle measurements we can extract the spin diffusion parameters, such as D and τ_s.

At a first look, the Hanle method seems a straightforward way to experimentally characterize the spin transport: D and τ_s can be extracted from a single lateral spin valve, while mapping the exponential decay of Eq. 4.4 requires a series of spin valves from which to extract ΔR_{NL} as a function of L. However, the reliability of the Hanle method is currently a point of discussion [162–164].

4.4 Graphene lateral spin valves: state of the art

The first graphene spin-valve devices were realized by Hill *et. al.* in 2006 [165], where two NiFe contacts were bridged by a 200 nm long graphene channel (see Figure 4.5). An intense line of research has followed and a nice review of the explored possibilities and addressed challenges can be found in [166,167]. Here we will limit ourselves to a quick overview of the major results achieved.

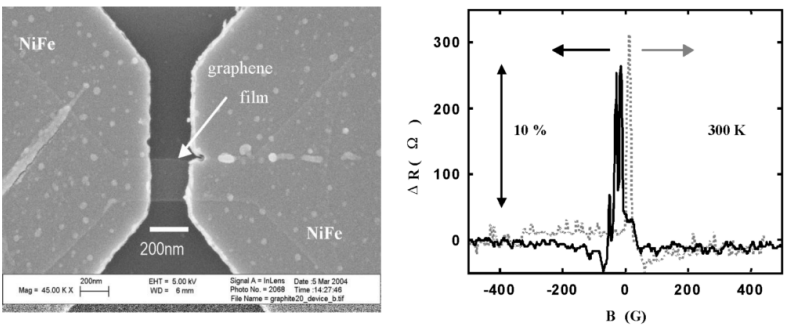

Figure 4.5: Left, SEM image of a Two Electrode Spin Valve structure showing the NiFe electrodes and a 200 nm wide graphene channel. Right, The MR response from the spin valve device shown on the Left. Adapted from [165].

Experimental achievements

Around the year 2007, a number of different publications on single and multilayer graphene spin valve devices were presented, this time exploiting the nonlocal measurement technique. We summarize them in Table 4.1. It is interesting to notice that all these studies concerned mechanically exfoliated graphene and only one of them [159] at this early stage reported Hanle measurements. The typical output from these publications, however, was the MR signal, rather than a reliable measurement of the intrinsic spin transport properties of the graphene: with the exception of the work in [159], these publications would typically focus on the ratio $\Delta R_{NL}/R$ rather than on the dependence of ΔR_{NL} on the distance between the electrodes, which can lead to an estimation of the spin diffusion length λ_s.

Table 4.1: Overview of the first publications in the field of graphene lateral spin valves.

graphene source	Non-Local	Hanle	FM/graphene junction	Reference
exfoliated	no	no	transparent	[165]
exfoliated	yes	no	transparent	[168]
exfoliated	yes	yes	Al_2O_3	[159]
exfoliated	yes	no	transparent	[169]
exfoliated	yes	no	transparent	[170]
exfoliated	no	no	MgO	[171]
exfoliated	yes	no	transparent	[172]

In the following few years the publication on graphene lateral spin valves grew significantly, and a representative list of experimental works is presented in Table 4.2, from which we can draw a few observations. As a first consideration, it is clear how the overwhelming majority of the works are from exfoliated graphene. This is most likely due to a number of reasons, not last the fact that this way of obtaining graphene can be very straightforward and of lowest economical costs. The physical argument, however, was that exfoliated graphene had been (and still has) shown to yield the highest values of mobility (μ), which is often taken as a measure of purity of the graphene against possible dopants. The reasoning was then to consider the cleanest possible source of graphene for such sensitive measurements as the ones of spin transport. As it turned

out later, however, we can not find a strong correlation between μ and λ_s, as shown in Figure 4.6.

Table 4.2: More recent developments in lateral spin valves over graphene. λ_s is the spin diffusion length and μ is the electrical mobility "O2 pl." stands for oxigen plasma.

Graphene	λ_s [μm]	μ [cm^2/Vs]	Etch	Hanle	Anneal	Ref.
CVD	3	2×10^3	yes	yes	no	[173]
exfoliated	1.2	20×10^3	no	yes	no	[174]
exfoliated	3	5×10^3	O_2 pl.	yes	Ar/H2 350 °C	[152]
exfoliated	3.3	5×10^3	no	yes		[175]
exfoliated	2.4	7×10^3	no	yes		[176]
exfoliated	1.4	3×10^3	no	yes	Ar/H2 200 °C	[177]
exfoliated[2]	20	40×10^3	no	yes	no	[178]
exfoliated[3]	4.7	100×10^3	no	yes	curr. anneal	[179]
exfoliated[4]	8	1.2×10^3	no	yes	no	[180]
SiC	100	17×10^3	O_2 pl.	no	no	[181]
SiC	0.9	1.9×10^3	O_2 pl.	yes	Ar/H2 350 °C	[182]

This is a relevant observation for CVD graphene where, even if exceptionally performing samples have been reported [72], typical values for μ are $\lesssim 3000$ $cm^2V^{-1}s^{-1}$. The other relevant observation for CVD samples is their rare presence in Table 4.2: although this technology came later (the seminal publication is from 2009 [11]), at the point of writing the present work the large majority of the graphene lateral spin valves publications is still based on exfoliated graphene, which is far from an industrially scalable solution.

As argued in [167,181], the interface resistance between the graphene and the FM contacts can be of much larger relevance than the electrical mobility of graphene. This further promotes the hopes of spin transport over CVD graphene, provided a good control of the FM/graphene interface is achievable.

[2] on BN

[3] suspended

[4] few layers

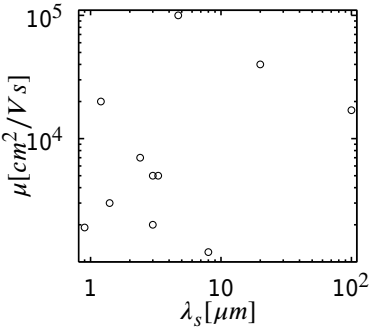

Figure 4.6: Scatter plot of electrical mobility μ versus spin diffusion length λ_s with the results from the works collected in Table 4.2. We can see the poor correlation between μ and λ_s.

5

Spin Valves on CVD graphene

We studied the diffusion of spin populations through CVD graphene by fabricating and characterizing spin-valve (SV) devices. The general background for the theory of spintronics and for the experimental techniques used has already been introduced in the past chapters: this section dives deeper into the specific of fabrication and analysis used for our spin valve devices. We will start with the challenges of the fabrication process, presenting the different strategies that were considered and comparing their advantages and disadvantages. Following, we collect the results from the experimental measurements and analyze them according to the theory presented earlier in this work.

5.1 Fabrication issues and strategies

Exploring spin diffusion in graphene by electrical means has a number of experimental constrains. It inevitably requires the fabrication of lateral structures, with the distance between the magnetic electrodes bounded to be smaller than the spin diffusion length. The shape of the electrodes also has a few constrains: the ideal ferromagnetic electrode for lateral spin valve systems has a narrow width (on the order of 100 nm) and a high aspect ratio, so to favour the alignment of its magnetization along a clear direction. In addition, there needs to be a dispersion in the widths of the electrodes, so to create different coercive fields, each characteristic of a specific contact, setting a need for reproducible, sub-micrometer precision. Finally, electrodes and graphene channel need to be aligned, again with sub-micron precision.

Typical fabrication strategy

The requirement for such precision can be addressed by Electron Beam Lithography (EBL) and this has been indeed the type of approach used in fabricating all of the SV of the present work. More specifically, a multi-step lithographic process has been used:

1. *Marks*. As it is crucial to be able to align a number of different lithographic steps, we start with fabricating cross-shaped marks on the surface of the sample. Each one of the following lithographic steps will then be aligned to these same marks. Marks are defined by EBL, metal deposition and liftoff.
2. *Etching*. We define the shape of the graphene channel out of the whole CVD layer. A lithographic step defines a polymeric mask over a particular area of the CVD graphene and then the whole sample is exposed to a physical etching step (plasma etching). Finally, upon removal of the resist, only the graphene covered by the polymer is left on the surface of the sample.
3. *Ferromagnetic (FM) contacts*. A further EBL step is used to define the shape of the FM contacts for spin injection and detection. As this and the previous step are aligned to the same reference marks, the electrodes are drawn precisely over the graphene channel. Metal deposition and liftoff follow.
4. *Large contacts*. A final lithography is used to define the non-magnetic contacts, typically Ti/Au or Pd contacts, which connect the SV device to millimeter-size pads, wich will then be used for the electrical contact to the measuring equipment.

To minimize possible issues coming from occasional bad liftoff or local defects in the graphene, a number of SV is fabricated in parallel on the same chip up to step 3 (between 9 and 12 devices, 100 µm apart from each another). Step 4 is then use to contact the most promising one.

Optimizing the lithography

As it is easy to imagine the process tends to be lengthy, with a considerable number of parameters involved. To reduce the complexity in the lithography, the following principles were used in optimizing the process:

- we stick with the same resist along the whole process: while other resists have been tested (*e.g.* ZEP 520A), using the same polymer along the whole fabrication reduces the number of parameters to optimize and the number of different chemicals coming in contact with the graphene.
- we reduce the possible range of EBL settings to three options, namely one value for the acceleration voltage (10 kV) and three for the column aperture (10, 30 and 120 µm). While other options in acceleration voltage and apertures are possible, these settings proved to be sufficiently suitable in resolution for the *FM contacts*, *Etching* and *Large contacts* steps, respectively.
- we fix the developing step and, where needed, play with the dose for fine adjustments. Although resolution could possibly improve by optimizing the development step, adjusting the dose is as effective and more straightforward in our experience.

One of the concerns in having such a large number of lithographic steps is the multiple exposure of the graphene to a range of different chemicals, which might alter its conduction properties. Removing the residues from the EBL resist, for instance, is known to be a very complex procedure [141], and residues from multiple EBL steps will cumulate over the fabrication process. One way to solve this is to cover the whole graphene sample with a few-nm-thick AlO_x film in the first place, so that the following lithography only comes in contact with AlO_x, which can ultimately be removed by wet etch. However, in our experience this was incompatible with the *Etching* step, as we will more clearly illustrate in the following section. An alternative approach is to minimize the number of different PMMA layers placed over the graphene and avoid dissolving the PMMA in acetone when possible. For instance, in the production of CVD graphene a PMMA layer is used to transfer the graphene from a Cu foil to a SiO_2 substrate. That same PMMA layer can be used in the first lithographic process, instead of spinning a new one.

Further reducing the number of PMMA coatings can come from "fusing" the *Marks* and the *Etching* steps. Instead of having metallic reference marks, we can define the alignment marks with overexposed PMMA by using writing doses > 5 mC/cm^2 (reference dose for clearance is 100 µC/cm^2). At such high doses PMMA behaves as a negative resist [142]: the written area will not dissolve in the developer and, incidentally, not in acetone either. We can then use the same lithographic step to define a PMMA mask for the etching step (by regular positive-lithography, *i.e.* exposing the surrounding area to the electron beam)

and the alignment marks (by writing these one with very high doses). This approach, however, has a significant drawback: negative-PMMA marks show very poor contrast (if any) to the SiO_2 substrate in a 10 kV electron microscope. The only option for the following step (the definition of the FM contacts) is to work at a lower acceleration voltage ($\lesssim$ 4 kV), which will yield a more surface-sensitive image in the electron microscope, and allow the system to locate the alignment marks. However, the performance of the lithography at such low voltage was not always satisfactory.

Finally, one could invert the fabrication process and have the graphene at last, transferred on an already fabricated set of electrodes. This method leaves very little control over the graphene-FM interface compared, for instance, to the UHV conditions achievable in a metal evaporation system.

Etching graphene

CVD graphene comes in films of large areas, with lateral dimensions easily of the order of centimeters [11] and a polycristalline structure above length scales of $\sim$ 100 µm. Defining a micrometer-size channel is essential for characterizing the spin-transport and this is mostly achieved by protecting the area of interest with a polymeric mask (defined via lithography) while the rest is being etched away in an oxygen plasma [7,181–184], most typically in less than 30 s and 50 W power. As shown in chapter 3. Characterization of devices, however, this resulted in not-well defined structures, with graphene residues clearly visible in the Raman maps.

Much cleaner results were obtained by Reactive Ion Etching in and Ar/O_2 atmosphere (see details in Table 5.1). Electrical measurements also confirmed a superior quality, with the resistance of individual graphene strips scaling with their lengths and without electrical paths shorting different devices.

As pointed out in the literature, graphene is very sensitive to disorder both in electric and spin transport [152,185,186], and that SV devices fabricated on etched graphene flakes lose reproducibility compared to the ones fabricated without etching [152]. Chemical and physical disorder is inevitably introduced in an etching process, however this remains a *sine qua non* step for CVD graphene electronics.

The AlO_x barrier

The non-local signal measured in lateral spin valve devices comes from the diffusion of a net spin-population across the channel. Although the propagation length of this accumulation is limited by intrinsic properties in the channel, its amplitude can be engineered at the point of injection, particularly with respect to the conductivity mismatch problem [150,177,187]. A common approach here is to increase the interface resistance at the ferromagnet-channel junction by introducing a thin dielectric layer (typically AlO_x, TiO_x or MgO) between the two conductors. This applies for the case of graphene as well: lateral spin valves with graphene(/TiO_x)/AlO_x/Co [152,159,188], graphene(/TiO_x)/MgO/Co [189], graphene/MgO/Py junctions [190], and others [191,192] have been reported in the literature.

In fabricating our SV devices, an appealing strategy is to cover the whole graphene with an AlO_x layer as a first fabrication step, in order to use the AlO_x as both a protective layer for the graphene and a tunnel barrier at the point of spin-injection. In graphene flakes it has been shown that the presence of the AlO_x layer on top of the channel does not influence the spin-transport properties [152]. The flip-side here for CVD graphene is that an etching step is required to define the graphene channel, as opposed to directly finding a natural graphene flake with an elongated shape. In our experience, a physical etch inevitably causes a redeposition of material along the sides of the graphene channel. Figure 5.1 shows an Atomic Force Microscope profile resulting from such a fabrication procedure, with clear horn-like structures building up along the sides of the graphene channel. As it turns out, these structures can be comparable to the thickness of the FM electrodes, hindering their homogeneity (if not their conduction at all), therefore the alternative of etching the graphene first and depositing the AlO_x underneath the FM material only, by using the very same lithographic mask, appears to be more promising.

The uniformity of the AlO_x layer is key for a reproducible control over the interface resistance. Growing such a layer over graphene is notoriously challenging due to a poor wetting of Al on graphene. Metal evaporation of Al followed by natural oxidation is a strategy which struggles to deliver uniform, dense AlO_x barriers [193]. We confirmed this by monitoring the growth of the AlO_x with electron microscopy. Figure 5.2 shows a number of SEM images where the individual grains of AlO_x are clearly visible: after the deposition of up to a few nanometers of Al, the coverage is far from uniform. One alternative option is

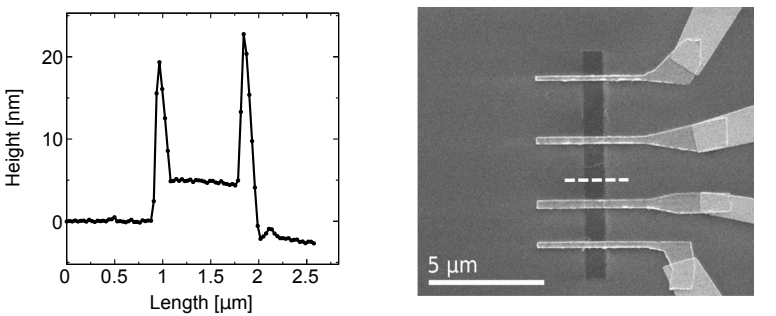

Figure 5.1: Evidence for the redeposition of AlO_x during an etching step. Top right, SEM image of a typical graphene SV device. The dotted line indicates the location where the Atomic Force Microscope (AFM) profile was measured. Top right, AFM profile transversal to the graphene channel. High spikes emerge along the sides of the channel, as a result of the redeposition of etched AlO_x. Bottom, schematics of the fabrication sequence: we start with a CVD graphene on SiO_2 substrate, covere it with a 1.5-nm-thick AlO_x layer, coat with a PMMA layer, define a PMMA mask by EBL, expose to an ion milling etching step and ultimately remove the PMMA (acetone bath).

to sputter the Al on graphene [167], which we indeed found to deliver a more uniform coverage, particularly for deposition rates higher than 1 Å/s. However, the Raman spectra of graphene after the sputtering step systematically showed an enhanced D peak, most likely a result of the highly energetic deposition process. Attempts to reduce this damage to the graphene by tuning the pressure of the Ar gas or the distance of the sample from the sputtering target did not result in significant achievements: although it has not been quantified how sensitive the diffusion of spins in graphene would be to the presence of these defects, sputtering did not appear to be an encouraging strategy.

Atomic layer deposition (ALD) is also a promising technique, as it is capable of growing single atomic layers of oxides with chemical precision in thickness and coverage. Graphene is, however, inert to the ALD precursors, as there are no available dangling bonds [188]: the dielectric grows only from edges and defects in the lattice [194]. To enhance the adsorption, one option is to evaporate a thin layer of seeding material, for instance AlO_x, without fully covering the surface of the graphene. The ALD process is, however, challenged again at its next step: a reactant must be introduced in the chamber in order to oxidize the deposited material, the most common choice being H_20. As graphene is hydrophobic, the reaction can result in patchy and non-uniform oxidation. Promising results have been shown for the growth of HfO2 on exfoliated graphene [195], but we were not able to reproduce these results in our CVD-based graphene devices.

In conclusion, although sputtering and ALD alternatives were considered, the optimization of the evaporation technique turned out to be the most promising and straightforward solution.

Ferromagnetic contacts

The ideal FM electrode would be in a magnetic monodomain state, with a high polarization and its magnetization sharply directed in one single direction at all stages of the measurements (*i.e.* only changing in sign). To favor this arrangement, the FM electrodes are designed as long and thin leads (shape anisotropy enhances directionality), with widths on the order of ~100 nm (to favor the single-domain state) and material of high purity deposited in (Ultra) High Vacuum chambers.

These attentions enabled us to achieve SV devices on graphene with injec-

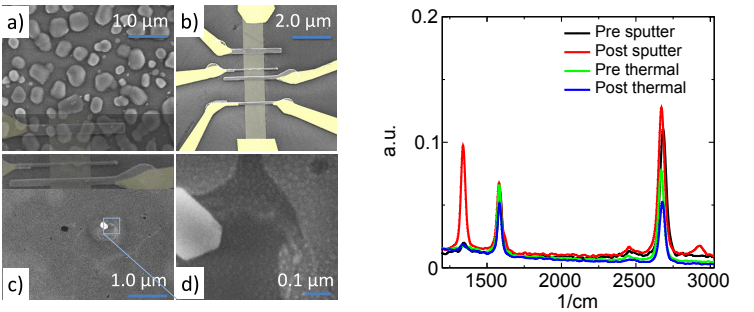

Figure 5.2: The sputtering technique could be optimized to yield uniform AlO_x layers, but at the cost of higher graphene defect densitiy. a) SEM image after sputtering 5 nm (nominal) of Al at a deposition rate of 0.2 Å/s over CVD graphene, with the Al naturally oxidized. To show the relevance of the granular structure, we superimpose at the bottom of the image a detail (to scale) of a typical device shown in (b). b) SEM image of a typical device, color-coded for clarity: we can identify the graphene stripe (vertical, light grey), the FM electrodes (horizontal, grey), and the Ti/Au electrodes for contacting the device (yellow). c) SEM image after sputtering 2 nm (nominal) of Al at a deposition rate of 2.0 Å/s over CVD graphene, with the Al naturally oxidized. Note that the scale is the same as in (a): the granularity of the AlO_x film is greatly reduced by sputtering at higher rates. d) Detail of (c): the granularity in the AlO_x is visible only at much higher magnifications. Right panel: results of Raman characterization for samples undergoing sputtering or thermal metal deposition. A clear D peak after the sputtering step emerges, signaling an increased defect density in the graphene.

tor and detector electrodes in clear parallel and anti-parallel states, as we will show in the following sections. On this respect, the experience of the group of research in fabricating metal-based spin valves [187,196–200] has been of tremendous help. However, the reproducibility of the FM electrodes achieved there was not directly transferable to our graphene devices due to a few different geometrical and fabrication constrains. Firstly, in order to reduce edge effects[1], the graphene channel is about 10 fold wider than the analogous metallic one (~1 µm, *versus* the &lessim;100 nm wide Cu channel), requiring longer (and thus more fragile) FM electrodes. Secondly, in fully metallic spin valves a gentle etching step precedes the deposition of the FM electrodes: the shape of the electrodes is defined by EBL but, just before deposition, the sample is exposed to a soft ion milling step to ensure a clear the channel-FM interface. Such etching step would inevitably harm the monolayer graphene and had to be removed, at the cost of a less reproducible interface.

Recipe details for Lateral Spin Valves on CVD graphene

A typical fabrication recipe resulting from the optimization of the fabrication steps described above is shown in Table 5.1.

Table 5.1: Typical fabrication process. DF stands for *dose factor* (*i.e.* the effective dose used is DF × 100 µC/cm^2) and US for *ultra-sonication*.

Section	Step	Details
Marks	PMMA	495kA4/950kA2 14krpm 45s, bake 180C 60s (2x)
	EBL	10kV 30um - DF 1.2 step 0.02um
	Develop	MIBK:IPA 1:3 60s, IPA 30s, spindry
	Deposit	sputtering: 50-200nm Pd; (or evaporation: 5nm Ti / 40nm Au)
	Liftoff	Pd: Acetone few min, IPA 1min, spindry. Ti/Au: ≤ 1.5h Acetone, spray Acetone, (US few seconds low power), IPA few min, spindry

[1] Edge magnetism has been predicted in narrow graphene strips (*i.e.* graphene nanoribbons) for certain edge geometries. [201]

Section	Step	Details
Etching	PMMA	495kA4/950kA2 4krpm 45s, bake 180C 60s (2x)
	EBL	10kV 10um - DF 0.8 step 0.02um (small area)
	EBL	10kV 120um - DF 0.8 step 0.2um (large area)
	Develop	MIBK:IPA 1:3 60s, IPA 30s, spindry
	RIE	30s 5 sccm O_2 50 sccm Ar, 40W, 10 mTorr
	Cleaning	warm acetone, 10min IPA, blowdry
	EBL	10kV 10um 28pA - DF 1.2 step 0.02um
	Develop	MIBK:IPA 1:3 60s, IPA 30s, spindry
	Deposit	0.5 nm Al to be oxidized in air (for tunneling barrier)
	Deposit	evaporation: 35nm Co
	Liftoff	Acetone 30min (US(low) if needed), IPA, spindry
Large	PMMA	495kA4/950kA2 | 2.5krpm 45s, bake 180C 60s (2x)
contacts	EBL	10kV 30um 220pA - DF 1.1 step 0.02um (small area)
	EBL	10kV 120um - DF 1.1 step 0.2um (large area)
	Develop	MIBK:IPA 1:3 60s, IPA 30s, spindry
	Deposit	sputtering: 50-200nm Pd; (or evaporation: 5nm Ti / 40nm Au)
	Liftoff	Pd: Acetone few min, IPA 1min, spindry. Ti/Au: <=1.5h Acetone, spray Acetone, (US few seconds low power), IPA few min, spindry

We found a great variability in the performance of SV devices fabricated on CVD graphene, despite achieving reproducible lithography, ensuring a well-defined etching step, and considering different metal deposition techniques. For instance, the interface resistance could range from ~Ω to 100 kΩ and the spin signal ΔR_{NL} from undetectable to ~Ω. We could extract a spin signal from 1 out of 4 samples on average, but achieving measuring a spin signal from more

than one SV in the same device proved to be a much more rare event (~1/10 on average). In the case of working devices, characterization of the graphene's electric (*e.g.* sheet resistance ~1 kΩ/□) and spin transport properties (*e.g.* spin diffusion length ~ 1 µm) yield consistent results across a few different fabrication strategies. At the same time, little correlation could be found between the yield of performing devices and the fabrication options investigated (*e.g.* the specific metal deposition technique used or the magnitude of the interface resistance).

Based on these observations, we must consider whether the origin of this variability could come from outside the range of explored options, rather from a poor optimization of the fabrication process.

One place for improvement could be a better control over the morphology of the CVD graphene itself. in Figure 5.3 we show SEM images of two SV devices fabricated over the same chip, using the very same CVD graphene sample. The electronic microscope shows textures next to the one device unseen in the other, which extend in the region of the graphene as well. We could not clearly determine the origin of these features, but it would seem to be independent of the fabrication process, as the two devices in Figure 5.3 went through the same steps at the same time. The Cu substrate for the Chemical Vapor Deposition growth of the graphene is a possible source of inhomogeneities [202], however a definitive assessment would require further studies.

5.2 Measurements of spin diffusion length

Non Local Spin Valves (NLSV) are our technique of choice to characterize the spin transport in graphene. On the one hand it is the most intuitive one, with a clear point of spin injection and detection. On the other, this technique has extensively been used to characterize metallic channels already [149,163,203–210], making it a convenient way to confront our results with the ones in the literature.

Other techniques for the characterization of spin transport that can apply to graphene include devices exploiting the Spin Hall Effect in graphene [211], the fabrication of graphene quantum dots [212] or the Spin Pumping effect [213,214]. However, the spin valve technique remains the most widely adopted one in the graphene literature for extraction of spin transport characteristics.

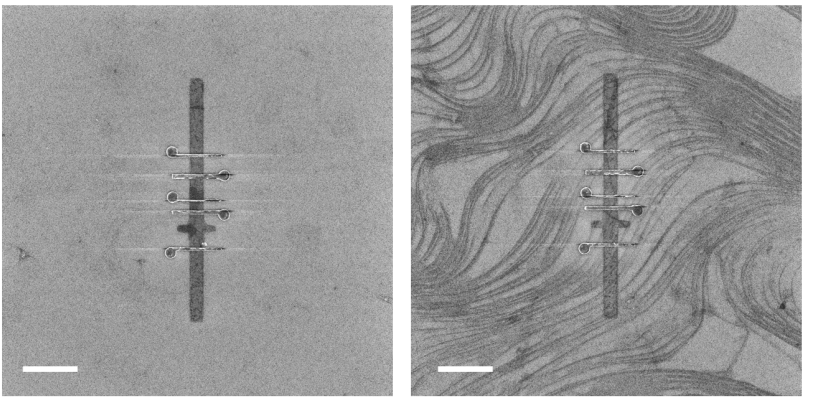

Figure 5.3: Same device fabrication on same chip, just a few hundreds microns away: the landscape is completely different and suggests there are inhomogeneity independent of the fabrication steps here described. Scale bars are 4 µm long in both images.

Typical spin valve signal and its interpretation

Figure 5.4 shows the typical spin valve signal from our NLSV devices. As we sweep the magnitude of an external in-plane magnetic field, the relative alignment between the injector and detector magnetization alternates between parallel and an anti-parallel, with the two states yielding different values of non-local resistance. As we have detailed in Section 4.3, when an electrical current is forced through the injector electrode, a shift in the spin population of the NM is produced, causing a net spin population in the later. The injected spin population diffuses from the injector to the detector electrode, shifting the electrochemical potential of the later to an out-of-equilibrium value, which can be measured with a voltmeter. The experiment typically starts by aligning the electrodes to the external magnetic field $\mathbf{H}$, setting the later to a value H_{sat} high enough to reach magnetic saturation of the electrodes (~3 kOe). The value of H then sweeps up to $-H_{\text{sat}}$, while a current I is forced through the injector electrode into the graphene, generating a non-local voltage V_{NL}. The non local signal $R_{NL} = V_{NL}/I$ is monitored as a function of H, which selectively switches the magnetization of the electrodes, starting from the one with the lowest cohercivity.

The same figure also shows how this signal depends on temperature in two

interesting ways. In the first place, the amplitude of the non local signal, *i.e.* the difference ΔR_{NL} between the resistances measured in parallel and anti-parallel configurations, does not vary significantly with temperature, which is an appealing point for room temperature applications. On the other hand, it shows a temperature dependence of the coercive fields of the ferromagnetic electrodes, where, as expected, we see a slight magnetic hardening as the temperature decreases, which typically translates into a sharper magnetic contrast between the different electrodes. This brings us to a curious observation: in the case of graphene lateral spin valves we prefer low-temperature measurements due to the magnetic properties of the electrodes (*i.e.* clearer magnetic contrast), rather than due to the spin transport properties of the channel (which, contrary to most metals, are virtually temperature-independent).

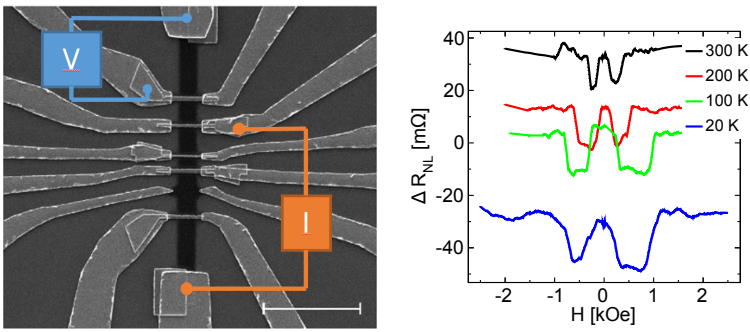

Figure 5.4: Left: SEM image of a typical graphene lateral spin valve whith an example of electrical connections for a non-local measurement (scale bar is 4 μm). Right: Non local measurements over the same graphene spin valve at different temperatures.

NLSV signal as a function of distance in between electrodes

The most intuitive approach to measuring the spin diffusion length is to map the amplitude ΔR_{NL} of the non-local signal as a function of the separation between injector and detector electrodes.

In Figure 5.5 we show the results of this type of study. We use a lateral spin valve device where multiple ferromagnetic electrodes are contacting the graphene, in such a way that the spacing between the electrodes vary

between half and several µm. We consider different combinations of injector and detector electrodes for the SV measurements and plot the values of ΔR_{NL} as a function of the edge-to-edge distance L between the electrodes. We have introduced already two analytical formulas to model this data, namely Eq. 4.4 and Eq. 4.3 for transparent and tunneling contacts, respectively, which we present here again for the reader's convenience

$$R_{NL} = \pm\frac{1}{2}P_I^2 R_N e^{-L/\lambda_N} \qquad \text{for } R_I \gg R_N \gg R_F \text{ (resistive)}$$

$$R_{NL} \propto \frac{1}{e^{L/\lambda_N} - e^{-L/\lambda_N}} \qquad \text{for } R_I \ll R_F \ll R_N \text{ (transparent)}$$

$$\Delta R_{NL} \overset{\text{def}}{=} R_{NL}^{\uparrow\uparrow} - R_{NL}^{\downarrow\uparrow}$$

where we have defined ΔR_{NL} as the difference between the non-local signal $R_{NL}^{\uparrow\uparrow}$ in the parallel magnetic configuration and the signal $R_{NL}^{\downarrow\uparrow}$ measured in the anti-parallel one.

In order to examine the difference between the two, we fit the measurements in Figure 5.5 to both equations and extract, in order, $\lambda_s = 1.0 \pm 0.26$ and $\lambda_s = 0.8 \pm 0.14$ µm. The agreement between the two formulas is to be expected, since for $L/\lambda_s > 1$ the one expression teds to the other. The particular sample in Figure 5.5 was fabricated with a 1 nm thick AlO_x layer between the graphene and the FM leads, which most likely accounted for the large amplitude of the ΔR_{NL} signal compared, for instance, to the one in Figure 5.4, and the extracted λ_s compares well with typical values for CVD graphene spin valves of ~1 µm [173].

Typically, despite ΔR_{NL} values changing up to an order of magnitude, our measurements of λ_s were always in the 0.7-1.2 µm range. This confirms that, although the amplitude of ΔR_{NL} is sensitive to the quality of the injection in a particular device, the spin transport measured is a more intrinsic characterization of the properties of graphene.

As a curiosity, we performed the same measurement over bi-layer CVD graphene, from which we extracted a $\lambda_s = 0.8 \pm 0.1$ µm, which compares quite closely to the previous case of single layer graphene.

Hanle measurements

Another technique to extract the spin diffusion length in NLSV systems is the Hanle measurement. As we introduced already in Section 4.3, the fundamental

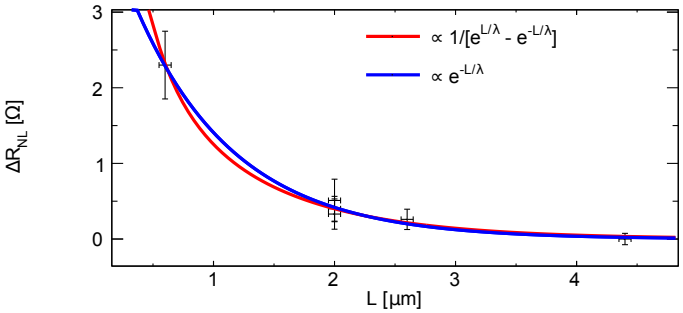

Figure 5.5: Dependence of the ΔR_{NL} signal on the edge-to-edge distance L between electrodes. The device is fabricated from a single layer CVD graphene, with 1 nm AlO_x at the graphene/FM interface. ΔR_{NL} is extracted from several spin valves present in the same device, some of which have identical spacings L. Measurements done at 150 K.

idea in a Hanle measurement is to have the injected spins precess about an out-of-plane direction as they diffuse through the channel. At the point of detection, only one projection of the spin (the one parallel to the FM electrode) will build up the R_{NL} signal, resulting in a dependence of R_{NL} on the angle of precession α. Experimentally, the precession is controlled by an external magnetic field $B_\perp$ orthogonal to the graphene.

The experimental procedure starts by setting the NLSV in a (anti-)parallel configuration applying an in-plane magnetic field. This field is then brought to zero, leaving the FM in their remanent magnetization state. The NLSV is now in its initial state: from here one, the R_{NL} signal is monitored as a function of an out-of-plane field $B_\perp$, as shown in Figure 5.6 and we expect the dependence of Eq. 4.5, which we report here for the reader's convenience:

$$R_{NL}^{P(AP)}(B_\perp) = \pm \frac{P_i P_d R_g D}{W} \int_0^\infty \mathrm{d}t\, P(t) \cos(\omega_L t) \exp(-t/\tau_s)$$

with $P(t) = \exp(-L^2/(4Dt))/\sqrt{4\pi Dt}$, where the ± stands for the parallel (P) and anti parallel case (AP).

For large values of $B_\perp$, the magnetization $\mathbf{M}$ of each FM electrode is tilted out of plane by an angle $\vartheta(B_\perp)$. In order to account for this, the former equation

is corrected [149,207]:

$$R_{NL}^{P(AP)}(B_\perp, \vartheta) = \pm R_{NL}^{P}(B_\perp)\cos^2(\vartheta) + |R_{NL}(B_\perp = 0)|\sin^2(\vartheta) \quad (5.1)$$

The dependence of ϑ on $B_\perp$ can be extracted from the anisotropic magnetoresistance (AMR) measurements of the FM electrodes as a function of $B_\perp$ [161]. Alternatively, we can recover the Hanle signal by considering that from Eq. 5.1 we have

$$R_{NL}^{P}(B_\perp, \vartheta) + R_{NL}^{AP}(B_\perp, \vartheta) = 2|R_{NL}(0)|\sin^2(\vartheta)$$

Re-arranging the terms in Eq. 5.1 we find

$$R_{NL}^{P}(B_\perp) = |R_{NL}(0)|\frac{R_{NL}^{P}(B_\perp, \vartheta) - R_{NL}^{AP}(B_\perp, \vartheta)}{2|R_{NL}(0)| - [R_{NL}^{P}(B_\perp, \vartheta) + R_{NL}^{AP}(B_\perp, \vartheta)]} \quad (5.2)$$

which does not require an additional AMR characterization of the electrodes, provided both P and AP Hanle measurements are available.

In Figure 5.6 all these characteristics are visible. The $R_{NL}^{P(AP)}$ signal modulates as expected from Eq. 4.5 up to a few kOe, after which the electrodes' magnetization gradually tilt out of plane and the corrections described in Eq. 5.2 become significant. The fit yields a spin diffusion length $\lambda_s = \sqrt{D\tau_s} \approx 1 \pm 0.1$ µm.

The Hanle measurement is a very convenient method for spin transport characterization since it requires only one non-local spin valve, compared to the previously described method where the ΔR_{NL} signal was measured over several spin valves with different inter-electrodes spacings.

At the same time, these measurements can be very sensitive to different device details, such as the contact resistance [162,163] or the finite length of the NM channel [164], resulting in a contact-induced spin dephasing and an under-estimation of relevant quantities such as λ_s. Generally speaking, all the modelling introduced is based on a 1-dimensional description of the diffusion process, which is definitely arguable in a 1 µm wide graphene channel. Additionally, the validity of the model in Eq. 4.5 for the case of transparent contacts is questionable [149] and more involved alternatives have been proposed

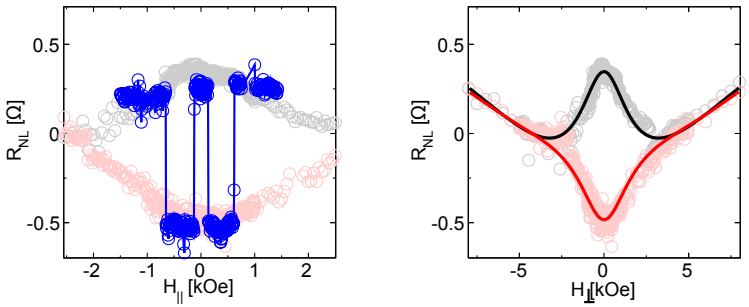

Figure 5.6: Hanle measurements over a graphene spin valve at room temperature. Left, the NLSV signal as a function of an in-plane magnetic field $H_{\parallel}$. In the background, the Hanle signal: although the Hanle measurement is done as a function of an out-of-plane field, we expect Hanle and in-plane values of R_{NL} to be the same, which we indeed find in this measurement. Right, the NLSV signal as a function of an out-of-plane magnetic field $H_{\perp}$. Solid lines are fit to Eq. 5.1.

[162,163]. On the other hand, it has been suggested that the spin relaxation induced by the contacts could be avoided when measuring on a longer inter-electrode distance [162,163].

In our case the model in Eq. 4.5 estimates values of λ_s that are in good agreement with those found by the *L*-dependence method, which leads us to conclude that the dispersion in λ_s is more a consequence of the difficulties in achieving reproducibility for the graphene devices rather than of a inaccurate Hanle analysis.

5.3 Summary and Conclusions

We have successfully achieved spin injection into CVD graphene. We presented here some of the issues encountered in optimizing the fabrication process, particularly in terms of reproducibility. Challenges in lithography, etching and metal deposition techniques were individually addressed and finally resulted in the fabrication recipe reported in Table 5.1. The non-local spin valve signal was analyzed both as a function of the distance between ferromagnetic electrodes

and also as a function of an out-of-plane magnetic field (Hanle measurement). Both approaches resulted in a value of approximately 1 µm for the spin diffusion length in graphene, which is in accordance to what reported in literature. Most interestingly, we were able to obtain Hanle measurements even at room temperatures.

Part III

Outlook on possible developments

6

Foreseeing the next step: Tuning the injection

We have discussed in Chapter 5 how the efficiency of electrical spin injection into graphene can be very dependent on the interface resistance. A transparent contact will typically suffer from the conductivity mismatch problem, while a less-invasive tunneling contact is generally preferable for preserving the spin polarization at the point of injection. In this chapter we explore a few other options for electrical spin injection, namely the injection of hot electrons.

6.1 Hot electrons: an introduction

For the purposes of this work, we shall consider a charge carrier to be a *hot-carrier* when its energy ε is well above the Fermi energy ε_F compared to the thermal energy k_BT, *i.e.* $\varepsilon - \varepsilon_F \gg k_BT$. This condition is typically realized in ballistic electron emission microscopy (BEEM) [215,216], where a scanning-tunneling-microscope (STM) metallic tip is used to inject electrons in a semiconductor, with the peculiarity that between the tip and the semiconductor electrons first tunnel through vacuum and then propagate through a thin ($\sim$ 10 nm) metallic layer.

Figure 6.1 shows the working principle of BEEM. Three terminals are applied to the *emitter* (in this case, the STM tip), the *base* (the thin metallic layer) and the *collector* (the semiconductor). Electron tunneling from the emitter

to the base electrode occurs upon applying a voltage V_{EB} between the two. Since typical attenuation lengths for metals are greater than 10 nm [217], the injected electrons may propagate ballistically through the base and reach the interface with the collector. For base-tip tunnel bias less than the base-collector barrier height Δ_c, there is no ballistic-electron current into the collector. On the contrary, as V_{EB} is increased above Δ_c, a dramatic increase in base-collector current I_{BC} occurs.

This current provides a direct probe of the interface electronic structure, including the Schottky barrier height, quantum-mechanical reflection of electrons at the interface, and ballistic-electron transport properties of the base film [215]. The distinctiveness here is in probing the energy barrier between a metal and a semiconductor in "operational conditions". For example, one can obtain a first approximation of Δ_c by considering the work functions of the metal and semiconductor, but the energy level alignment at the interface is ultimately determined by the electric dipoles that build up at the interface [218,219], which can be sensitive to fabrication details hard to control, like small contaminations in the deposition chamber, for instance. Injecting hot-electrons has the advantage of probing the interface energetics in real, operating conditions: instead of assuming a theoretical, expected Δ_c, we can probe the specific barrier of the device at hand. In addition, the BEEM technique has recently been applied to metal/molecule systems [220,221], as a means to extract information on the effective barrier height in these systems.

It is interesting to notice that the same understanding can apply to a fully solid-state device where the vacuum layer is substituted by an insulating material [222,223]. Graphene has very recently entered this field as a base-electrode candidate [224,225], where its strong points of ultimate thinness and high conductivity are used to enhance the performance of hot-electron transistors. This point of view proposes graphene as a means, but we suggest this technique could see graphene as the objective, at least in two ways. Firstly (and most trivially), a graphene-based device can be used as characterization technique to explore semiconductor-graphene energy alignment, which would be particularly interesting in the case of organic semiconductors. Secondly, graphene could be used as a collector to investigate the propagation of hot-carriers in graphene, which would be most appealing in the case of spin-polarized electrons. Keeping these suggestions as long-term proposals for our research, in the following section we present the first steps in realizing hot electron devices and in accurately extracting the spectroscopic information.

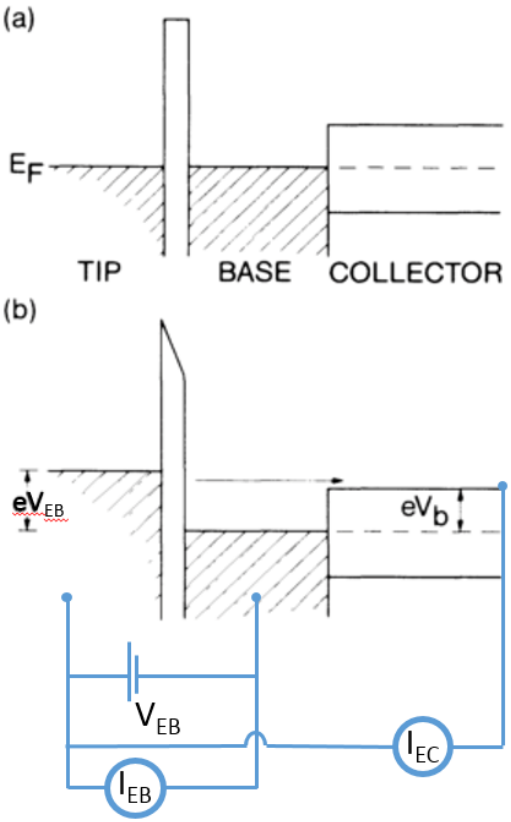

Figure 6.1: Schematic energy-band diagram for the three-terminal BEEM experiment, where the STM tip is separated by a vacuum barrier from the base metal. Terminals are applied to the tunnel tip, metal base, and semiconductor (typically Si) collector. (a) The energy-band diagram for zero tunnel bias, V_{EB}=O. (b) The energy-band diagram for tunnel bias greater than the barrier voltage, $eV_{EB} > eV_b$. We also highlight the electronic terminals used for the sourcing of the emitter-base voltage V_{EB}, the measurement of the emitter-base current I_{EB} and the emitter-collector current I_{EC}. Image adapted from [215].

6.2 Hot electrons in a solid state device

As a starting point for our study of hot electrons and metal/molecules interface barriers, we consider a metal-based device with a C_{60} molecular layer as a collector. The C_{60} here enters as a semiconductor material easy to evaporate, which enables more freedom in the realization of devices (by hard-mask deposition) compared, for instance, to a bulk Si substrate. The whole device is fabricated as a vertical stack of layers deposited in UHV conditions:

1. The emitter is fabricated as a 13-nm-thick Al film, which is then plasma-oxidized *in situ* to create a thin AlO_x barrier.
2. The base metal is deposited over the AlO_x barrier. Different metals are used, in order to explore the different energy level alignments with the C_{60}.
3. A 200 nm thick molecular layer of C_{60} is deposited over the base, ultimately capped with a 15 nm thick Al electrode.

A sketch of the relative band alignments is shown in Figure 6.2. As a voltage V_{EB} is applied between the emitter and base terminals, electrons[1] tunnel through the AlO_x barrier and propagate through the base, with a fraction of them reaching the base-collector interface. When V_{EB} is smaller than the base-collector barrier Δ_c, the emitter-collector current I_{EC} is suppressed, whereas for $V_{EB} > \Delta_c$ we expect a roughly linear [216] increase of I_{EC}. Once in the semiconductor, electrons thermalize quickly [222] and diffuse to the Al electrode. Two factors drive this diffusion: firstly, these electrons have a component of their momentum directed perpendicularly to the base/collector interface; secondly, an electric field is present in the semiconductor due to the difference in work functions of the emitter and collector: since the top Al electrode has the highest work function of all metals here considered, the electric field is always directed to accelerate the electrons towards the collector. Employing a ferromagnetic emitter or base metal results in a net spin-polarization of the hot-electrons reaching the semiconductor [222,223].

[1] More generally the current arises from hot *carriers*. However, due to the specific band alignments present in this case, the transport is always driven by electrons, rather than holes.

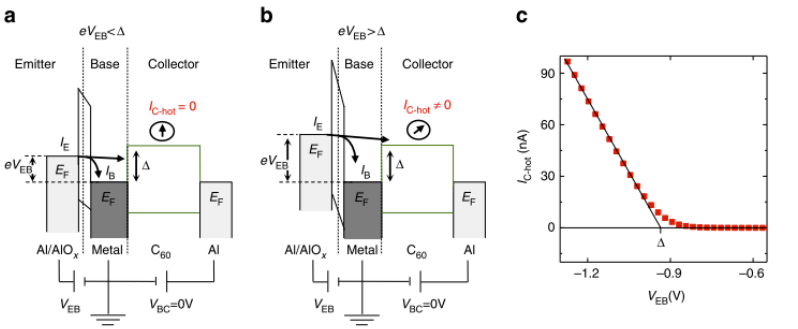

Figure 6.2: Working principle of the device. (a,b) Sketch of the energetics of the device. (a) For $0 < V_{EB} < \Delta_c$ electrons are collected in the base terminal and no collector current I_{EC} is measured. (b) For $V_{EB} > \Delta_c$, part of the electrons tunnelling into the base flows into the C_{60} resulting in $I_{EC} > 0$. (c) Hot electron current I_{EC} in a device with a 10-nm-thick Cu base at 245K. The barrier height is Δ_c = 0.95 eV, as obtained by interpolating the linear fit of the growth and the *I*=0 line. Image adapted from [226]

Analysis and modeling of the measurements

We can obtain the barrier height Δ_c in a simple and visual manner by fitting the rise of I_{EC} above V_{EB} by a linear function over some hundreds of mV and extract the voltage at which the fitting line intercepts $I_{EC} = 0$ as an approximation of the barrier height. In the case of Figure 6.2 we obtain Δ_c = 0.93 V. We refer to this as the *liner extrapolation* method.

Further information can be extracted from the hot electron current by a more careful modeling. In a 1-dimensional picture, we can express the current I between two electrodes as [227]:

$$I_{12} = \frac{e}{\hbar} \int d\epsilon \sum_{\nu\mu} |T_{\nu\mu}(\epsilon)|^2 A_1(\nu, \epsilon + eV_{\text{Bias}}) A_2(\mu, \epsilon) [f(\epsilon + eV_{\text{Bias}}) - f(\epsilon)]$$

where $A_1(\nu, \epsilon)$ is the spectral function[2] of the state $|\nu\rangle$ at energy ϵ in electrode 1, $A_2(\nu, \epsilon)$ is the analogous for state $|\mu\rangle$ in electrode 2, $f(\epsilon)$ is the Fermi

[2] As a reminder to the curious reader, the spectral function is typically used in the context of second quantization, many body physics calculations. Its formal definition involves the introduction of Greens functions, for which we refer to many body physics textbooks (see, for instance,

distribution, V_{Bias} is the voltage applied between the two conductors and the term $T_{\nu\mu}(\epsilon) = \langle \nu|\mathcal{H}|\mu\rangle$ describes the coupling between the two electrodes, where $\mathcal{H}$ is the Hamiltonian of the system.

The physical interpretation here is that the current between the electrodes at a given energy ϵ will be determined by the difference in Fermi levels times a transmission coefficient $\mathcal{P}_{12}(\epsilon)$, which in turn depends on the presence of electronic states in each electrode at that energy ($A_1(\nu, \epsilon + eV_{\text{Bias}})A_2(\mu, \epsilon)$) and the coupling between the two electrodes ($T_{\nu\mu}$). $\mathcal{P}_{12}(\epsilon)$ may be a function of ϵ depending on the particular coupling between the electrodes. For instance, in a tunnel junction where the tunneling barrier φ is very large (*i.e.* $\varphi \gg eV_{\text{Bias}}$), $\mathcal{P}_{12}(\epsilon)$ is independent of ϵ and (at least in the zero temperature limit) one recovers the linear dependence $I \propto V_{\text{Bias}}$ [228].

At higher values of V_{Bias}, however, $\mathcal{P}_{12}(\epsilon)$ will be a particular function of ϵ determined by the specific barrier, and the linearity between I and V_{Bias} will generally be lost. One of the simplest approaches here is the Fowler–Nordheim description, where the dependence of the transmission probability on ϵ is found to be exponential. We can apply the Fowler–Nordheim approach to our particular case for the emitter-base junction, where we have an AlO_x tunnel barrier between two metallic regions, and write $\mathcal{P}_{EB}(\epsilon) = C_{EB}e^{\epsilon/\lambda}$. We then obtain:

$$I_{EB} = \frac{e}{\hbar}\int \mathrm{d}\epsilon\, C_{EB}e^{\epsilon/\lambda_\epsilon}\left[f(\epsilon - eV_{EB}) - f(\epsilon)\right]$$
$$I_{EC} = \frac{e}{\hbar}\int \mathrm{d}\epsilon\, \mathcal{P}_{EC}(\epsilon)\left[f(\epsilon - eV_{EB}) - f(\epsilon)\right]$$

where the indexes E, B, C stand for emitter, base and collector.

We can make a few considerations about $\mathcal{P}_{EC}(\epsilon)$. The probability of the electrons entering the C_{60} depends on the tunneling through the AlO_x, the probability of thermalizing in the base (reflected in what we previously referred to as the attenuation length), and the probability to enter the C_{60} from the base. To first approximation, we can consider all these as independent and

Ref. [227]). For the scope of this work, it will be sufficient to recall that the spectral function is related to the density of states $g(\epsilon)$. This is evident since the occupation number n_ν for the state $|\nu\rangle$ can be calculated as $n_\nu = \langle c_\nu^\dagger c_\nu\rangle = \int \frac{d\epsilon}{2\pi}A(\nu,\epsilon)f(\epsilon)$, which implies that the total number N of fermions (at equilibrium) is $N = \sum_\nu n_\nu = \int \frac{d\epsilon}{2\pi}\sum_\nu A(\nu,\epsilon)f(\epsilon)$, which must be equal to $N = \int d\epsilon\, g(\epsilon)f(\epsilon)$, finally leading to $g(\epsilon) = \sum_\nu A(\nu,\epsilon)/2\pi$.

write $\mathcal{P}_{EC}(\epsilon) = \alpha \mathcal{P}_{EB}(\epsilon)\mathcal{P}_{BC}(\epsilon)$, where we follow Bell *et al.* [216] in taking the attenuation constant α as independent of energy. In addition, the density of states in the metallic layers is constant for small values of V_{EB} and we can write $\mathcal{P}_{BC}(\epsilon) \approx \mathcal{C}_{BC} \sum_\nu A_C(\nu, \epsilon) = \mathcal{C}_{BC} g_C(\epsilon)$, where $g_C(\epsilon)$ is the density of states in the C_{60}. These approximations are rather simplistic, but, as it turns out, sufficiently accurate to describe our measurements.

All together, the expressions for the currents now are

$$I_{EB} = C_{EB} \frac{e}{\hbar} \int \mathrm{d}\epsilon \, e^{\epsilon/\lambda_\epsilon} \left[f(\epsilon - eV_{EB}) - f(\epsilon) \right]$$
$$I_{EC} = \alpha \, C_{EB} C_{BC} \frac{e}{\hbar} \int \mathrm{d}\epsilon \, e^{\epsilon/\lambda_\epsilon} g_C(\epsilon) \left[f(\epsilon - eV_{EB}) - f(\epsilon) \right]$$

from which we obtain

$$\frac{I_{EC}}{I_{EB}} \propto \frac{\int \mathrm{d}\epsilon \, \left[f(\epsilon - eV_{EB}) - f(\epsilon) \right] e^{\epsilon/\lambda_\epsilon} g_C(\epsilon)}{\int \mathrm{d}\epsilon \, \left[f(\epsilon - eV_{EB}) - f(\epsilon) \right] e^{\epsilon/\lambda_\epsilon}} \tag{6.1}$$

In the original model [215], $g_C(\epsilon)$ was approximated as a Heavyside function centered at Δ_c (*i.e.* $g_C(\epsilon) = \Theta(E - \Delta_c)$), with the physical meaning that all the electrons above the Schottky barrier would enter into the semiconductor, while all the electrons below it would be reflected back into the base, implying that the density of states of the semiconductor would not have any influence on the number of injected electrons, other than a harsh cut in the energy axis.

For a more realistic description of the metal/molecule interface, we can consider a more accurate function for $g_C(\epsilon)$. At the interface, the molecular levels broaden because of the interaction with the metal surface, with a broadening that can be approximated by a Gaussian or a Lorentzian distribution [218,219,229], as sketched in Figure 6.3. Therefore, the electrons can enter in the semiconductor before reaching the C_{60} lowest unoccupied molecular orbital (LUMO) level, since they find available states in the tail of the LUMO energy broadening. We thus approximate the density of states in the C_{60} as

$$g_C(\epsilon) = \begin{cases} \beta \exp\left[-\frac{1}{2} \left(\frac{E - \Delta_c}{\sigma_c} \right)^2 \right] & \text{for } E < \Delta_c \\ 1 & \text{for } E > \Delta_c \end{cases}$$

Above the LUMO, other molecular levels are available, which also broaden and hybridize with the LUMO. Therefore, we approximate the density of states above the LUMO as a featureless continuum of states. Such approximation is rather gross, but in the region of interest (*i.e.* at $eV_E B \approx \Delta_c$) the increase of I_{EC} compared to a linear approximation is determined by the Gaussian broadening of $g_C(\epsilon)$.

We fabricated and characterized three different hot electron devices, with $Ni_{80}Fe_{20}$, Au and Cu bases. The measurements from the hot electron device were fitted with Eq. 6.1, from which we extracted the values of λ_ϵ, Δ_c and σ_c and the fitted data is shown in Figure 6.3.

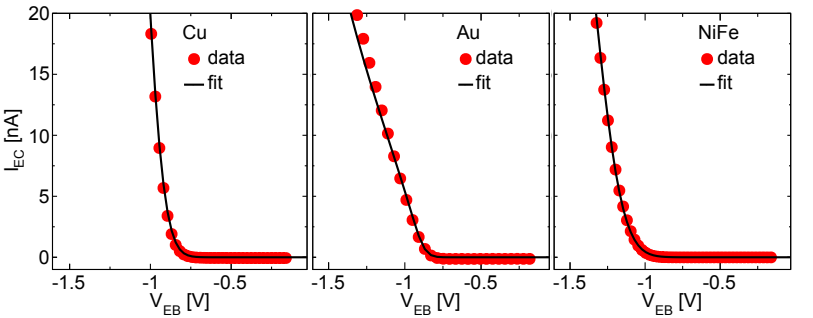

Figure 6.3: Corrected version of the hot electron injection model, where we take into consideration the finite density of states in the C_{60} according to Eq. 6.1. The results of the fits are reported in Table 6.1. Measurements done by Marco Gobbi [226].

Table 6.1: Results from fitting the hot electron data. Δ_{lin} is the value obtained with the linear extrapolation; Δ_c, σ_c and λ_ϵ result from fitting the mesurements with Eq. 6.1. Φ is the work function of the material (the LUMO level of bulk C_{60} sits at 4.5 eV)

Material	Φ [eV]	Δ_{lin} [eV]	Δ_C [eV]	σ_c [eV]	λ_ϵ [eV]
Au	5.3	0.89	0.93	0.045	0.20
NiFe	5.1	1.2	1.37	0.150	0.18
Cu	4.7	0.93	1.05	0.100	0.22

In Table 6.1 we summarize the findings for both the linear extrapolation Δ_{lin} and the fitting method. The first observation we can make is that the values of base/semiconductor barrier extracted by the two are consistent with $\Delta_{\mathrm{lin}} = \Delta_c - \sigma_c$. The trivial interpretation here is that a large fraction of the ballistic electrons encounter an effective barrier at $\Delta_c - \sigma_c$, which results in an injection in the C_{60} at energies below the LUMO. In addition, we note that the values of Δ_c and Δ_{lin} for NiFe are larger than for Au and Cu, which we would not expect based on the sole analysis of the work functions.

In fact, the rearrangement of the metal electron density at the interface with the C_{60}, which contributes to the energy level alignment at the interface, depends on the metal's tendency to transfer charge, which is inversely proportional to the density of states of the material at the Fermi level. This property is often called hardness [230]. NiFe is more prone to transfer charge [231] than Au and Cu, so we can expect a higher interface dipole and consequently a higher energy barrier, which nicely explains the measurements. This result shows that the work function is not the only important factor for the determination of the interfacial energetics.

The values of σ_c, which in our modeling represents the energy broadening of the LUMO of the C_{60}, varies significantly among the three cases. This parameter describes the degree of interaction between the molecules and the metal surface [218,229], so it is consistent to find that NiFe has the highest σ_c

On the other hand, the values of λ_c are around 0.2 eV for all cases. The variability here is reduced because the AlO_x barriers were produced in the same conditions. Similar values for λ_c were reported in previous studies [219,232].

In summary, we have applied a detail modeling to the hot electron current measured in a fully solid state device. This enabled not only the evaluation of the interface barrier Δ_c at the base/collector interface, but also further insight into the energetics of metal-molecule junctions, namely with the estimation of the electrostatic interactions through a Gaussian broadening of the molecular layers. This is a valuable method for the analysis of hot electron devices and of graphene-based one in particular.

6.3 The Graphene-C_{60} junction

In the prospects of fabricating a hot-electron device with graphene, we start by characterizing the graphene-C_{60} junction. From the study shown in the previous section, we can expect the formation of an energy barrier at the interface between the graphene and the C_{60}. We can also expect the amplitude of this barrier to be dependent on the difference in the (bulk) work function $\Delta\phi$ between the two materials: although $\Delta\phi$ is not sufficient to accurately evaluate the energy barrier, the general trend of a higher barrier with a higher $\Delta\phi$ still holds. Graphene's work function can be tuned by Field Effect, so it is interesting to investigate the transport properties across the graphene-C_{60} barrier *as a function of an applied backgate voltage.*

In order to focus on the graphene-C_{60} junction, we suspend the hot-electron design and consider a simpler vertical FET geometry. Our device is show in Figure 6.4. It sees a single-layer CVD graphene transferred onto a Si++/SiO2 substrate. The highly-doped Si and the 300-nm-thick thermal SiO2 layer act as a gate electrode and a gate dielectric, respectively. Lithography and RIE define a 2 mm-long and 100 µm-wide strip of graphene, with Ti/Au electrodes (defined by lithography and metal evaporation) for electrical contact. FET characterization of the graphene strip yields typical mobility values of $\gtrsim 1000$ cm^2/Vs. A 280-nm-thick C_{60} layer is then evaporated over the sample in ultra-high vacuum (UHV) conditions through a shadow mask, accurately tailored to define a cross-bar graphene/C_{60} junction area of 1 mm × 100 µm. Finally, a 30-nm-thick Al layer is deposited on top of C_{60} for electrical contact.

We apply a voltage V_{ds} between the Al and the graphene contacts and measure the two-point current I_{ds} flowing through the device, as a function of a backgate voltage V_g. As the resistances of the metallic layer ($< 10\,\Omega$) and of the graphene ($\sim$ kΩ) are negligible compared to the C_{60} ($\gtrsim$ MΩ), we can consider that the whole voltage drop takes place either in the bulk of the C_{60} or at the interfaces with its contacts, namely the Al or graphene[3]. For the results presented here, the graphene electrode was grounded and, since the C_{60} is a photo-sensitive material, we took care of performing the measurements in a dark chamber.

The transport across the whole device depends dramatically on the value of V_g.

[3] We have checked that this is the case for all values of backgate voltage tested: $R_{device} \gg R_{gr}$, R_{Al} $\forall$ V_g, where R_{device}, R_{gr} and R_{Al} are the resistance of the device as a whole, of the graphene and of the Al, respectively.

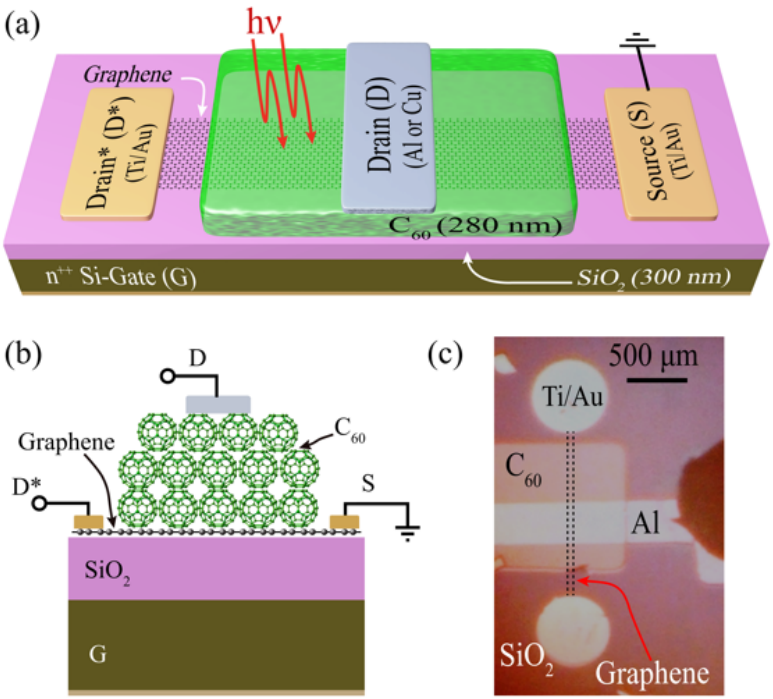

Figure 6.4: a) Schematics of our device: CVD-grown graphene is transferred on a Si/SiO_2 substrate and subsequently patterned. Ti/Au contacts and C_{60} are then separately evaporated. Finally, either Al or Cu is deposited on top of C 60 for the collector (drain) contact. b) Cross-sectional schematic view of the device. c) Optical microscopy image of a typical graphene/C_{60}/metal device. Image made by Subir Parui, adapted from [233].

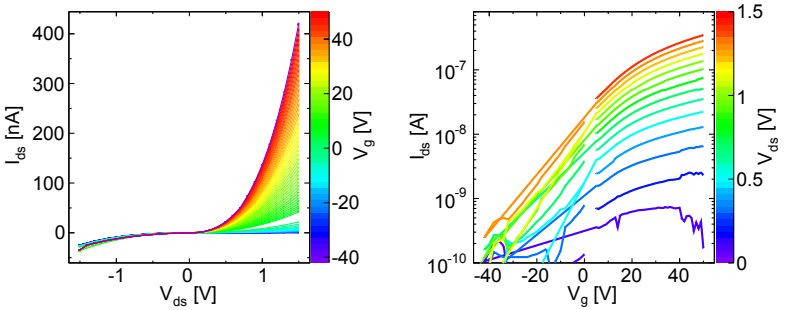

Figure 6.5: I-V characteristics of a hybrid graphene-C_{60} device, 2 point measurement at room temperature. Left, the measured current I_{ds} flowing through the device as a function of the applied voltage V_{ds}, for a range of gate values V_g (color scale). Right, transfer characteristics, where the same data as in the previous panel is shown as a functon of V_g (V_{ds} in color scale).

Figure 6.5 shows the $I_{ds}(V_{ds})$ characteristics for different values of V_g, where we can see a gate-dependent diodic behaviour. For sufficiently high values of V_g the device is rectifying, but for $V_g \leq 10$ V the conduction is suppressed. We will start by examining these two effects, the gate dependence and the rectification, separately.

The backgate voltage V_g induces a surface charge carrier density

$$n = C_g|(V_g - V_D)/e| \tag{6.2}$$

where C_g = 12 nF/cm^2 is the gate capacitance per unit area for a 300-nm-thick SiO2 layer, V_D is the value of the gate voltage which maximizes the graphene resistance, and e is the elementary charge. This notably results in a change in conductance for the graphene, which however is not sufficient to explain the measurements. As we pointed out, the resistance of the graphene is always negligible compared to the one of the C_{60}, thus the series of the two will only shift $\sim$ 1‰, while the gate dependent changes in Figure 6.5 can be much larger. A similar thought is to suppose a field-effect induced change of the C_{60} bulk conductivity. However this alone would not justify the asymmetry in the $I_{ds}(V_{ds})$ measurements.

The expression for n in Eq. 6.2 is rigorous only in the case of an ideal capacitor

with an electric field fully confined between two parallel plates. As soon as we consider a non-perfect electrical screening at the graphene/C_{60} interface, a redistribution of the carrier density will emerge so that $n_{gr}<n$ carriers will populate the graphene while $n_{C60}=n-n_{gr}$ carriers will be induced in the first layers of C_{60}. Based on what learned in the previous section of this chapter, we can expect this change in carrier density to affect the electric dipole at the graphene/C_{60} barrier.

In fact, an energy barrier at the graphene/C_{60} interface is the ideal candidate to explain the rectifying characteristics of the device. In a similar way as in the base-collector junction in Figure 6.2, we can suppose an energy barrier at the graphene/C_{60} interface where the C_{60} LUMO sits at a higher energy than the Fermi level, blocking the transport in one direction. The interesting suggestion we can harvest from the measurements in Figure 6.5 is that this interface barrier modulates with the backgate voltage.

The models discussed for hot-electron injection are not directly applicable in this case. The transport through the whole device is far from ballistic and, most importantly, we can not quantify the exact voltage drop across the graphene/C_{60} interface from knowing V_{ds} only, since most likely there will be a voltage drop $V_{Al\text{-}C60}$ at the Al-C_{60} junction and a finite voltage drop V_{Bulk} across the bulk of the molecular layer which we cannot quantify *a priori*.

It is interesting, however, to consider how these quantities would depend on V_g. As we illustrate in Figure 6.6, grounding the graphene has the important consequence that all the field effect from the backgate must be confined to the graphene. If we consider the profile of V_g in the z-direction (*i.e.* the direction perpendicular to the graphene plane) at $V_{ds}=0$, we note that $dV_g/dz = 0$ for all z values above the graphene, which is forced at zero electric potential. Consequently, there is no electric field that can extend to the C_{60} or to the Al/C_{60} interface to modulate their carrier density. For $V_{ds}\neq 0$ there clearly are electric fields through the device, but the same reasoning still applies: the graphene layer is forced to ground, screening the gate-driven electric field. Should we have a conducting material above the graphene, the induced carrier density n would spread in it up to a characteristic length of the order of the Debye length, leaving only n_{gr} extra carriers in the graphene, as previously discussed.

This observation allows us to conclude that, although we can not extract the exact value of the graphene/C_{60} barrier, we can evaluate its backgate tunability by examining the gate-dependent changes in the $I_{ds}(V_{ds})$ measurements. In Figure 6.5 we can see that I_{ds} changes over three orders of magnitude as a

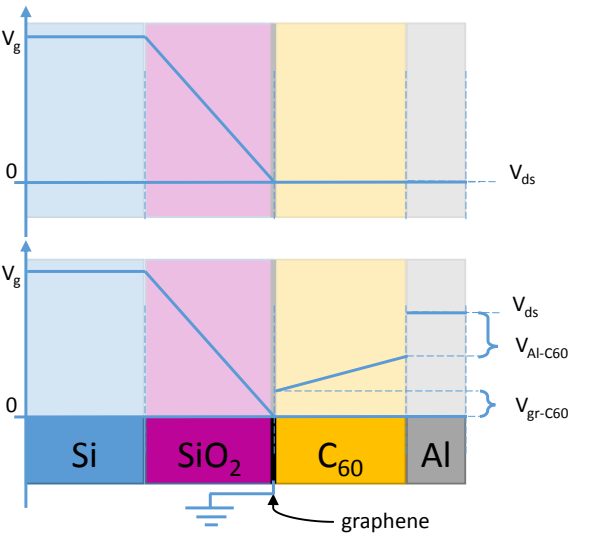

Figure 6.6: Schematic voltage drop across the device. On the horizontal axis, a cross-section of the device components (not to scale), while on the vertical axis we show the electrical potential. Because the graphene is grounded, the electrical field effect from the gate electrode does not penetrate the bulk of the C_{60}, thus modulating the graphene/C_{60} interface only, as opposed to modulating both the interface barrier and the C_{60} bulk resistivity as well. This line of thought applies both when there is no voltage V_{ds} applied between the Al and the graphene electrode (top) and when $V_{ds} \neq 0$.

consequence of the changes at the graphene/C_{60} barrier. At the current stage, integrating this into a spin valve device requires further research and optimization. However, if such an interface were to be used for the injection of spin currents, its large resistance tunability could prove very useful in alleviating the conductivity mismatch issue.

6.4 Summary and Conclusions

In this chapter we have introduced the phenomenon of hot electron injection, from its initial applications in Ballistic Electron Emission Spectroscopy to its realization in a fully solid-state device. This innovative approach allows for a direct insight into the energetics of interface barriers, which can play a major role in the transport across the device. Here we elaborated a model based on ballistic conduction across the base electrode, which enabled an accurate description of the emitter-collector current I_{EC}, and allowed for the measurement of the energy alignment at the metal/molecule interface in a three terminal, solid-state device. Interested in exploring the graphene-C_{60} interface, we considered a C_{60} layer sandwitched between a graphene and a metallic contact in a vertical FET geometry. The electrical characterization indicated that the graphene-C_{60} interface is a major player in the transport: although we could not single out the specific contribution of the interface to the measured resistance, our understanding suggests that the gate dependence of the current (modulation over 3 orders of magnitude) is primarily attributable to a modulation of the graphene-C_{60} barrier.

7

Graphene on a ferromagnetic substrate

In the previous chapters we have discussed the diffusion of a net spin population in graphene and the challenges in injecting a spin-polarized current into this material, which is a demanding task on its own. With a proven spin-injection, an interesting question to ask is whether we can manipulate the spin current as it diffuses through the graphene channel. Hanle measurements are an example of achieving such a manipulation by an external magnetic field. Another example is *magnetic gating* [196], which modulates the amplitude of the spin current through the magnetization of an insulating substrate. The thought of studying transport in graphene on a ferromagnetic substrate is even more appealing as recent publications predict a large spin polarization of graphene's π orbitals when the carbon lattice is placed on a ferromagnetic insulator [234–236]. An induced magnetic response in graphene could lead to significant advances in topics such as spin transport, spin transfer torque or magnetic random access memories [237–239]. Attracted by this active field of research, in this chapter we explore the transport properties of graphene transferred on YIG. Specifically, we make use of magnetoresistance (MR) measurements to show how the magnetization of the substrate influences the resistivity of the graphene strip and, conversely, to what extent such resistivity measurements are revealing of the YIG's magnetostatics.

7.1 Fabrication of the device

Our device is sketched in Figure 7.1. Single layer graphene, produced by Chemical Vapor Deposition (CVD) [11], is transferred on a YIG substrate and shaped into a Hall bar geometry by means of Electron Beam Lithography and Reactive Ion Etching in a Ar/O_2 atmosphere. A second lithographic step defines the Ti/Au electrodes. Electrical characterization has been carried out with a standard four-point-measurement technique and a 0.1 mA current amplitude. Typical sample characterization done via Hall effect shows that the graphene is moderately doped (carrier density $\approx 4 \times 10^{12}$ cm^{-2}) and presents an electrical mobility of 2800 $cm^2V^{-1}s^{-1}$. The YIG sample employed here is a 2 µm thick single crystal film grown epitaxially on a paramagnetic gallium gadolinium garnet (GGG) (111) substrate.

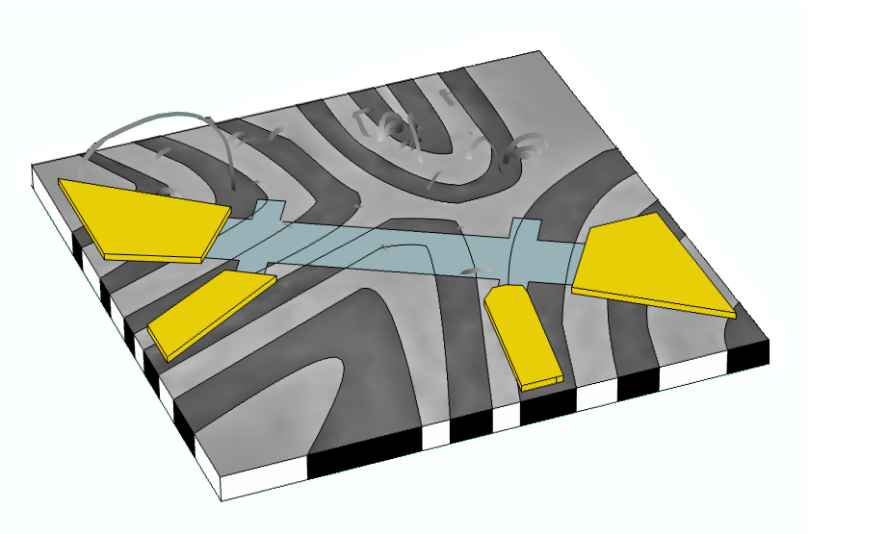

Figure 7.1: Schematic drawing of the device. The YIG sample is represented in its stripe domain configuration (black and white domains represent the direction of the out-of-plane magnetization). A CVD graphene strip lays over it, contacted through Ti/Au leads.

7.2 Characterization of the device

In order to probe the magnetic coupling between the substrate and the graphene we perform magnetoresistance measurements sweeping an external magnetic field **H** both in intensity and direction. We also perform magnetic characterization of the substrate alone.

Magnetoresistance measurements

The in-plane MR measurements are of special interest in a 2D system. Both the Lorentz force and the weak localization physics depend only on the out-of-plane component of the magnetic field, and thus they do not contribute to the in-plane field MR [240]. A potential problem might arise since the graphene is never absolutely flat and wrinkles would inevitably give rise to a finite size area where the flux of the external field is non-zero. As a crosscheck experiment, we always performed analogous measurements for graphene transferred on a SiO_2 substrate, which proved that in-plane MR - if any - is not measurable in our usual setup. This is a relevant point, as it implies that any MR signal measured in this configuration must come from a coupling of the resistivity of the graphene to the magnetization of the YIG (as opposed to a coupling to the external magnetic field **H**).

Figure 7.2 a shows the sheet resistance (ρ) of the graphene device for an in-plane magnetic field (*i.e.*, for a polar angle $\theta = 90°$). There is a clear non-monotonic modulation of ρ with increasing magnetic field, which is peculiar on its own. In addition, as the azimuthal angle φ between the direction of the current in the graphene and the external magnetic field changes (Figure 7.2 b), a six-fold modulation of ρ emerges. The combined dependence of ρ on φ and H is shown in Figure 7.3 c (ρ in the color scale), where we can distinguish three regimes. The low-field regime (namely $|H| < 50$ Oe), where no angular dependence of ρ is present while its value increases with H. The second regime ($50 < |H| < 150$ Oe), where $\rho(H, \varphi)$ is non-isotropic. Finally a third regime (150 Oe $< |H|$) where the resistivity is, again, isotropic.

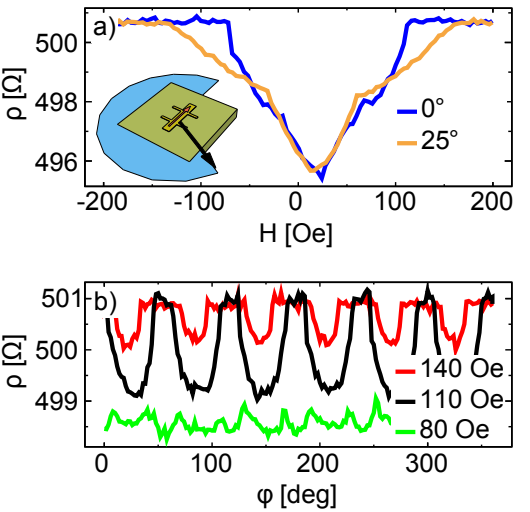

Figure 7.2: Dependence of the graphene's sheet resistance ρ on the magnitude and orientation of an *in plane* external magnetic field **H**. a) Graphene sheet resistance ρ for an in plane magnetic field at two selected values of φ, specifically 0° and 25°. We notice both the qualitatively unusual shape of the curve and its angular dependence for 50 Oe < |H| < 150 Oe. Inset: schematic representation of the geometry of the experiment. b) ρ as a function of the azimuthal angle φ between **H** and the electrical current in the graphene. Three particular values of H are shown, namely 80, 110 and 140 Oe for the green, black and red curves respectively. A peculiar 6-fold periodicity is observed for the second graph, which is then lost at higher fields.

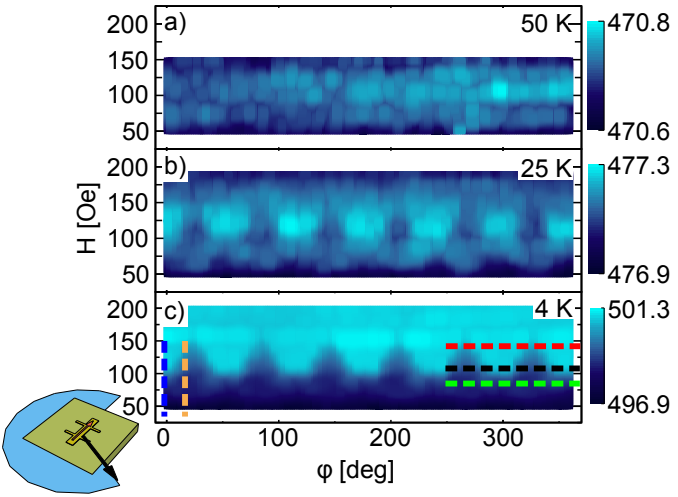

Figure 7.3: ρ (color scale) as a function of both intensity and direction of the external, in-plane, magnetic field at 3 different temperatures. The panels in Figure 7.2 are cuts to the data in Figure 7.3 c, the dotted lines in the later being guides to the eye, color coded as the respective curves in Figure 7.2.

Magnetometry characterization of the YIG substrate

To confirm that these modulations in fact relate to the substrate magnetization, we turn our focus to the ferromagnetic insulator. In Figure 7.4 a we show the room temperature magnetic characterization of the YIG substrate performed with a vibrating sample magnetometer (VSM). Under an in-plane magnetic field of magnitude > 100 Oe, the YIG film is magnetically isotropic, but at small in-plane magnetic fields (H<50 Oe) the hysteresis loop shows an articulated structure, consequence of a non-trivial magnetization process.

YIG films are well known to exhibit a stripe-domain magnetization pattern [241,242]. The geometry of such domains in the bulk is, in a first approximation, that of parallel, in-plane stripes of opposite magnetization directions. At H=0 the magnetization of the epitaxial film is directed out of plane, with stray field lines connecting neighboring domains. To confirm this result in our sample as well, we performed electron holography images at the surface of the YIG (see Figure 7.4 d), which clearly indicate the stray field lines connecting neighboring domains, confirming the magnetostatic description. Lorentz microscopy images, as the ones elegantly reported in [243], show that, under an external in-plane magnetic field, the average size of the domains grows and the orientation of the magnetization gradually rotates into the plane of the film, until saturation is reached.

Specifically, in Figure 7.4 c we note a six-fold symmetry in the measured magnetic moment as the external field rotates in the sample plane. Similarly to what has been observed in Figure 7.3 c, we can again distinguish three regimes in the dependence of the magnetization **M** on **H**. The first one, occurring at small fields, shows an isotropic magnetization. The second one (for 30 Oe < |H| < 50 Oe), where **M** depends on φ; and a third one for higher fields, where again **M** is isotropic. YIG has a cubic structure which, when observed from the (111) direction, shows a 6-fold symmetry. The crystal symmetry manifests itself as an in-plane magnetization symmetry [244]. Since YIG is a very soft ferromagnet, the presence of such easy in-plane magnetization axes is generally overlooked. However, especially in low-field measurements (for instance like the ones reported here or elsewhere in the literature [246]), these details of the YIG magnetostatics can play a relevant role in the electronic transport.

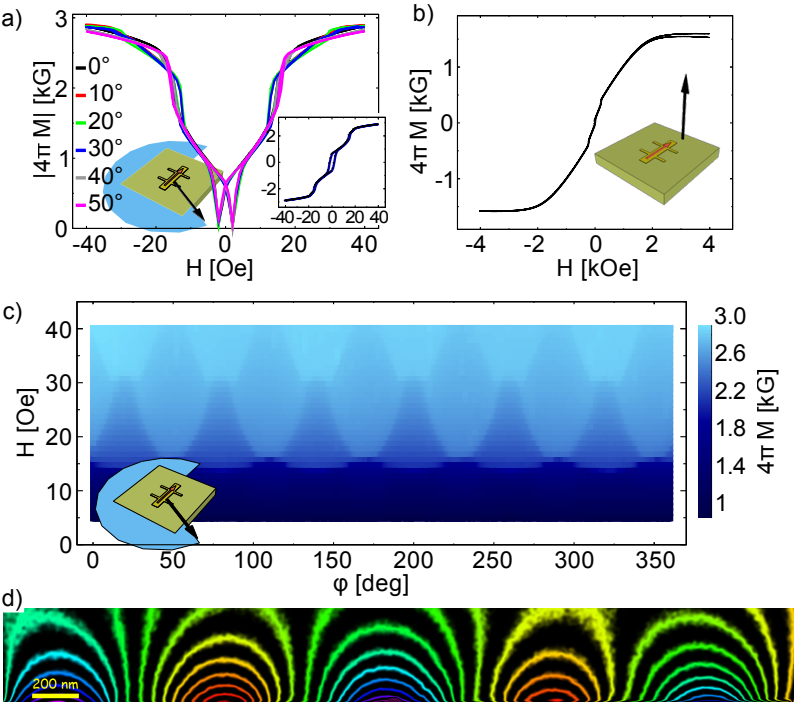

Figure 7.4: Magnetic characterization of the YIG (111) on GGG sample (field-in-plane geometry). a) In-plane magnetization M of the YIG as a function of an in-plane external magnetic field *H*. The hysteresis loop is suggestive of a non trivial magnetization process. b) The absolute value of M as a function of H, for different in-plane angles φ. As **H** rotates in the plane of the sample, changes in the hysteresis loop are visible for 30 Oe < |H| < 50 Oe. In the context of this work a positive or negative value of the field $\mathbf{B} = \mu_0(\mathbf{H}+\mathbf{M})$ at the surface of the YIG contribute equally to the resistance of the device, which makes |M| a more relevant quantity than M. c) M(H, φ) (color scale) for different values of H and azimuthal directions of magnetization φ. d) Electron holography image at the surface of the YIG for a plane perpendicular to the sample's surface: the lines picture the iso-levels for the stray field H_{str} at H_{ext}=0. The scale bar (bottom left corner) is 200 nm.

Weak Localization

There is a strong correlation of the in-plane magnetization data with the ρ(H) shown in Figure 7.3 c. More quantitatively, the exact values of H that delimit the different regimes in Figure 7.4 c are slightly different since the two measurements were carried out at different temperatures (room temperature for the VSM measurements, 4K for the magnetoresistance ones). The critical values of **H** for the later are slightly larger than for the former, which is consistent with a moderate magnetic hardening of the YIG at low temperatures.

Considering the results shown above, it is tempting to speculate that the current **I** in the graphene channel is being spin-polarized via proximity effect to the magnetization **M** of the YIG, and that the product **I**·**M** is at the origin of the modulation of the graphene's resistivity. However, we show here below that a simpler explanation should be considered.

In order to understand the changes in the graphene resistivity with the applied magnetic field, we can consider the well-known quantum phenomenon of weak localization (WL). WL is a positive correction to the resistivity of a conductor, which decreases in an increasing magnetic field. At its core, WL is an interference effect with a natural length scale of the electron's phase coherence length λ_φ [240], which will be generally material dependent. For the specific case of graphene, we expect a relatively strong WL due to the low dimensionality: a requirement for WL is the presence of self-intersecting sections along the electrons propagating paths, which are more likely in lower dimensions. In addition, in a flat system only the out-of-plane magnetic field contributes to the changes in resistivity: since the physical quantity at the origin of the de-localization is the flux of the magnetic field **B** through the self-intersecting paths, all the magnetic contributions to the weak localization must be in the out-of-plane direction.

In Figure 7.5 a we show ρ as a function of an out-of-plane magnetic field and fit the data points for $|H| > 200$ Oe (considering the magnetization of YIG as a single domain in this regime) to the WL formula $\rho^{WL}(B)$ for graphene [247–249]. For such values of H, the fit in Figure 7.5 a describes quite accurately the measurements. However, around H=0 the measurements show a local minimum in ρ, whereas standard WL would predict a (local) maximum.

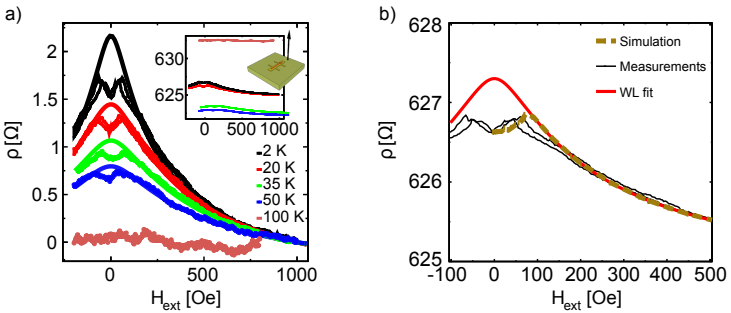

Figure 7.5: a) Measured graphene sheet resistance ρ as a function of an out-of-plane magnetic field H_{ext} at different temperatures *T*, where the *ρ(H)* curves have been rigidly shifted for easier comparison (see inset for original data). As the temperature rises from 2 K, both ρ(H) and the quantity ρ^{max} - ρ_0 goes to zero, suggesting that the local minimum in the graphene's MR around H=0 is due to weak-localization physics (the solid lines are fit to the weak localization formula for graphene). b) Closeup of the data in a) for *T*=2 K, where we add the calculated values for $\langle \rho(h) \rangle$ after simulation of a stripe domain structure in the YIG.

7.3 Modelling and discussion

Taking into account the information exposed, we argue that the field lines arising from the magnetic domains of the YIG substrate are the main contributors to the de-localization of the carriers in graphene, causing the minimum at H=0 in the magnetoresistance. For high values of the in-plane magnetic field (|H|>2 kOe), the magnetization **M** of the YIG is saturated and parallel to the external field (see Figure 7.4 b). As H decreases, **M** gradually turns in plane and the characteristic stripe domain pattern emerges, causing some stray field lines to cross the graphene. In this regime, the flux of the magnetic field **B** through the graphene surface changes sign on a scale comparable to the lateral dimensions *d* of the magnetic domains, which is expected to be comparable to the film thickness (in our particular case, the YIG is 2 μm thick). On the other hand, the phase coherence length λ_φ in graphene - which can be extracted from WL theory – is 10 to 100 times smaller than *d*. We can then expect WL effects in the MR measurements since, even though the flux of *B* through the whole graphene averages zero, locally (*i.e.* on the scale of λ_φ) WL always gives a

positive contribution to the resistivity, just as if the graphene were in a homogeneous magnetic field.

The fits in Figure 7.5 a effectively consider the YIG as monodomain for |H|>200 Oe. The WL is a function of the magnetic field $B = \mu_0(H_{ext} + H_{str})$, where here on we distinguish between the external magnetic field H_{ext} and the stray field from the YIG domains H_{str}: as long as $H_{str} \neq 0$ (*i.e.*, the YIG is in a multidomain configuration) a fit of $\rho(H_{ext})$ like in Figure 7.5 a is not rigorously valid. *A priori*, we cannot exclude the presence of stripe domains until the ferromagnet is saturated, which happens only for a field $H_s \sim 2$ kOe. For $H_{ext} < H_s$ the magnetic domains will change in two ways [242]: (i) by the *displacement* of domain walls, leading to the growth of the domains in which the magnetization makes an acute angle with H_{ext}; (ii) by the *rotation* of the magnetization vectors within domains.

The displacement processes tend to dominate at small fields and are well described in the literature. Models like the one in ref. [250] enable us to evaluate H_{str} as a function of H_{ext}. We consider 1 layer of alternating magnetic domains and compute the stray field $H_{str}(x,z)$, where the (x,y)-plane is taken to be the plane of the YIG surface. As H_{ext} changes, the size *d* of the domains evolves and a new field $H_{str}(x,z)$ is found. We can then evaluate the resistivity of the graphene at each point in space and average over the length of the device:

$$\langle \rho(H_{\text{ext}}) \rangle = \frac{1}{L} \int_0^L \mathrm{d}x \, \rho^{\text{WL}} \left(B_{tot}(x) \right)$$

where $B_{tot}(x) = \mu_0 (H_{ext} + H_{str}(x,z_0))$ and z_0 is the height of the graphene above the YIG surface. This approach describes the whole magnetization process as a wall-displacement one (see information in appendix). A better agreement can be obtained considering a 2-step magnetization process, where for $|H_{ext}| < H_1$ we approximate the development as purely displacement-driven and for $|H_{ext}| \geq H_1$ we take the YIG as monodomain, with **M** rotating towards the out-of-plane direction. In Figure 7.5 b we show the result of these calculations, which accurately describe the data for $H_1 = 90$ Oe. In addition, the model yields a value for the size of the magnetic domains *d* at $H_{ext}=0$ of ≈ 0.5 µm, in accordance with the electron holography images in Figure 7.4 d. The agreement between the experimental data and the model could be improved with a more complex description considering both the displacement and rotation processes at each value of H_{ext}, but such level of detail is beyond the scope of this work. Our interest lies in understanding the nature of the coupling between the resistivity

ρ and the magnetic substrate, which we find can be explained through weak localization physics.

To further support this argument, we show in Figure 7.5 a $\rho(H_{ext})$ for different temperatures. We consider the difference between the measured resistivity (ρ_0) and the extrapolated value from the WL-fit (ρ_0^{WL}) at H_{ext}=0 as indicative of how effectively the stray fields de-localize the carriers in graphene. An accurate evaluation of quantity $\rho_0^{WL} - \rho_0$ is non trivial, as the fitting process necessarily lacks its most critical parameter, namely the value of ρ when no magnetic field is present (*i.e.* B = 0, instead of simply H=0). However, a qualitative trend clearly emerges from Figure 7.5, where the size of the local minimum at H_{ext}=0 (*i.e.* ρ^{max} - ρ_0, where ρ^{max} is the maximum value of ρ(H)) decreases with rising temperature. In fact, the ratio $\Delta\rho_{YIG} = [\rho^{max} - \rho_0]/[\rho^{max} - \rho(H = 1 \text{ kOe})]$ is approximately 9% across all the temperatures where we measure weak localization. Such consistency of $\Delta\rho_{YIG}$ across the measured temperature range further suggests that WL is the effect coupling the magnetization with the changes in resistivity in our experiments. Ultimately, the minimum in ρ at H_{ext}=0 could qualitatively resemble a weak anti-localization (WAL) phenomenon but, as shown in [251], WAL is not expected in graphene for these high carrier densities (4×10^{12} cm^{-2}).

7.4 Possible applications

Interestingly, the de-localization picture we have presented enables us to reverse the thought process. Instead of calculating the stray field from the YIG and then fitting the WL measurement, we can use the graphene as a sensor for estimating the field at the YIG surface for H_{ext}=0. In other words, we can invert the WL formula and indirectly measure the average $\boldsymbol{B}$ field at the surface of the YIG when no external field is applied.

Looking at the data in Figure 7.5 a (for clarity, let us consider the one at 2 K), we find that we measure the value ρ_0 both at H_{ext}=0 and at an external field H_c>0. Because the function $\rho^{WL}(B)$ is monotonic, we can infer that the flux of B through the graphene is the same at H_{ext}=0 and H_{ext}=H_c, and conclude that

$$\langle|\mathbf{B}_{\perp}^{surf}|\rangle = \mu_0 H_c = [\rho^{WL}]^{-1}(\rho_0)$$

where $\langle|\mathbf{B}_{\perp}^{surf}|\rangle$ is the component of the **B** field perpendicular to the graphene

plane at the surface of the magnetic material, averaged over the area of the graphene strip, and $[\rho^{WL}]^{-1}$ is the inverse of the WL function. The value we extract for this dataset is H_c = 125 Oe. Interestingly, we extract the same value from the simulation introduced earlier, with the two-step magnetization approximation.

This measurement of H_c is clearly different from the average magnetic field a magnetometer would measure far from the surface of the sample, as the stray field is stronger the closer to the YIG's surface. In our case, with MR measurements we determine the average magnetic field at the surface, which is difficult to experimentally evaluate knowing **M** only from a bulk magnetic characterization. Our measurement technique is also different from a micro-SQUID one, as this one would be sensitive to $\langle \mathbf{B}_\perp^{surf} \rangle$ instead of $\langle |\mathbf{B}_\perp^{surf}| \rangle$, the former tending to a value much smaller than the latter as the area of the SQUID increases. A micro-SQUID can deliver very local information about $\mathbf{B}_\perp^{surf}$ (for instance, if the dimensions over which the flux of *B* is sampled are smaller than the lateral sizes of the stripe domains), and similarly can a Magnetic Force Microscopy measurement. Our approach is for a more extended characterization of the surface, providing an averaged value of $\langle |\mathbf{B}_\perp^{surf}| \rangle$, instead of having to scan large areas over which to average $\mathbf{B}_\perp^{surf}$. As such, this setup is a very valuable characterization technique for the magnetic field of ferromagnetic insulators at their very surface.

Finally, we note the steep slope displayed by ρ(H) for $|H_{ext}| \lesssim 200$ Oe. Since the graphene is sensitive to the **B** field rather than **M**, any change of a few Oe at the surface of the YIG could be detected as a change in the resistance of the device. One could then use this property as a mean to measure small magnetic fields, like the ones from powder samples, or for characterizing double-layered systems, such as perpendicular magnetic recording media, where the loops for both the recording layer and soft under layer may be measured individually at once, a task not easily accomplished using conventional magnetometers [252], which would hardly disentangle the contribution of the one layer from the other. The temperature range where this would be feasible is not restricted to cryogenic temperatures: our samples serve as a proof of concept up to nearly 100 K, but WL in CVD graphene has been reported up to 300 K [248], paving the way to room temperature applications.

7.5 Summary and Conclusions

In conclusion, in this chapter we have presented magnetoresistance measurements of graphene devices placed over a YIG ferromagnetic insulating substrate. The MR curves remarkably resemble the magnetization of the YIG, both in the six-fold angular symmetry (field-in-plane configuration) and in the atypical structure for small fields (field-out-of-plane configuration). Although this resemblance might spark discussions regarding proximity effect in graphene in contact with a ferromagnetic substrate, we have developed a simpler explanation. The stray field from the stripe domains present in the YIG, which occurs for small values of H, has an out-of-plane component that de-localizes the electrons in graphene, causing a change in its sheet resistance. Our argument is based on a simulation of the YIG magnetization process, a good fit of the WL equation to our MR curves and on the temperature dependence of our measurements. The technique here presented constitutes a characterization tool complementary to that of traditional magnetometry.

Finally, we stress once more how, while exploring magnetic-proximity-effect physics on ferromagnetic insulators [246], one needs to be very aware of the magnetostatics of the substrate and be able to exclude effects from the possible stray field first.

Appendix

Determination of the WL parameters

The analytical expression for the resistivity in graphene with the weak-localization corrections ($\rho^{WL}(B)$) comes with 4 independent parameters [249], the most relevant of which (especially for small fields) are the value of the resistivity at zero B field (ρ_0) and the phase coherence length (λ_φ). As pointed out in the main text, ρ^{WL} is a function of the magnetic field $\mathbf{B}=\mu_0(\mathbf{H}_{ext} + \mathbf{H}_{str})$ arising from the superposition of the external field H_{ext} and the stray field of the magnetic substrate H_{str}. Typically the last one is unknown except for the case of a magnetically saturated YIG, where $H_{str}=0$. As a first option, we could extract the values of ρ_0 and λ_φ from graphene samples fabricated on SiO_2 substrates, but it is our experience that with CVD graphene samples these parameters vary significantly from sample to sample (*e.g.* a 1% change in resistivity across samples is too large of a variation compared to the weak localization correctons of $\sim$ 0.2% reported in the main text). Alternatively, we could fit ρ^{WL} only for $H_{ext}>H_s$ and extrapolate to lower fields, however the saturation field H_s for our sample is 1800 Oe (at room temperature), far larger than the values of interest in this work ($|H_{ext}| \lesssim 500$ Oe). In addition, from our experience on analogous graphene devices on SiO_2, we expect relatively small changes in ρ for such high fields, which would make the extrapolation of ρ_0 and λ_φ less accurate.

We propose a different (and, to the best of our knowledge, new) setup for WL measurements, which takes advantage of the 2D nature of the conductor.

Figure 7.6 shows the measured resistivities ρ as a function of an external fixed H_{ext} at a polar angle $\theta > 0$ with respect to the normal to the YIG surface. The low dimensionality of the graphene makes it sensitive only to the out-of-plane component B_z of the total magnetic field:

$$\begin{aligned} B_z &= \mu_0(H_{\text{ext}} + H_{\text{str}})\cos\theta \\ &= \mu_0\left(H^z_{\text{ext}} + H_{\text{str}}(\theta)\right) \end{aligned}$$

where we write $H_{str}(\theta)$ to emphasize that the stray field will have a non-trivial dependence on θ. This can be seen, for instance, considering the dependence on θ of the YIG saturation fields (as confirmed by VSM measurements): for H_{ext}=300 Oe and θ =0 the sample is *not* saturated ($H_{str} \neq 0$), but for H_{ext}=300 Oe and θ =90° it is ($H_{str} = 0$). From this observation we can conclude that H_{str} does indeed depend on θ, although the dependence is more elaborate than $\propto \cos(\theta)$.

In Figure 7.6 we also show the measured ρ as a function of H^z_{ext}: in this case, all the angular contributions must come from $H_{str}(\theta)$, while the rest of the data must be in a regime where $H_{str}(\theta)$ is negligible with respect to H^z_{ext}. A fit to the non-angular-dependent data yields the values for the parameters of $\rho^{WL}(B)$.

In summary, this analysis allows us to distinguish between the contributions to ρ coming from the external field H_{ext} and the ones coming from the YIG stray field H_{str}. It also shows that there is a particular field $H_{tr}(\theta)$ above which H_{str} is negligible compared to H_{ext}, which takes values up to $\lesssim$ 200 Oe. The magnetostatic insight is therefore that, for fields $H_{ext} > H_{tr}$, the difference in magnetic moment among stripe domains are small and the magnetization evolves mainly by rotation.

Modeling the magnetostatics

In order to understand the measurements at small fields we need to calculate the stray field H_{str} coming form the stripe domain magnetization of the substrate. We use the model in [250] and, with reference to the nomenclature used there, our case has N=1, t=1.7μm, and τ=0.2 erg/cm^2 [253]. For a given value of magnetization *m*, we compute the domain periodicity *d(m)* and the stray field H_{str}(m,x,z). Equation (6) in [250] enables us to compute also the value of H_{ext}(m) required to reach a magnetization *m*, so that ultimately we obtain the total magnetic field at any point in space as a function of the externally applied field: $H_{tot}(H_{ext}, x,z) = H_{ext} + H_{str}(H_{ext},x,z)$. We can then calculate the resistivity of the graphene at each point and average over the length of the device:

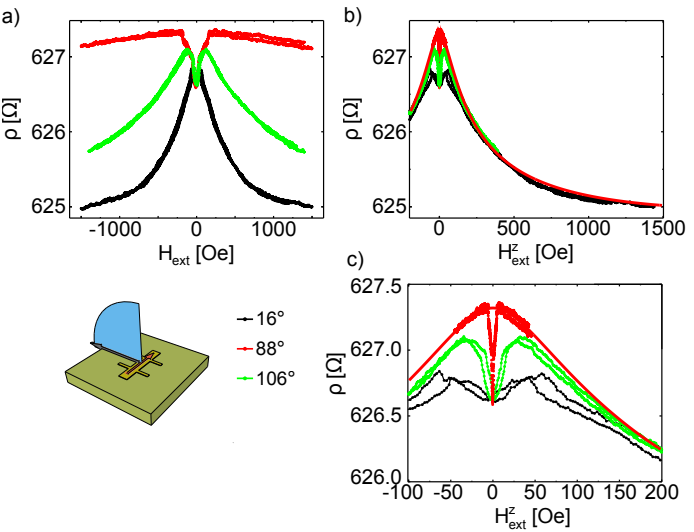

Figure 7.6: a) Measured graphene resistivity ρ for an external magnetic field H_{ext} changing both in intensity and direction (polar angle θ>0. b) Same data as in a), but plotted against the out-of-plane component H^z_{ext} of the external field: the angular-dependent data in this plot highlights the regions of field intensity where $H_{str} > H^z_{ext}$. c) Closeup of b).

$$\langle \rho(H_{\text{ext}}) \rangle = \frac{1}{L} \int_0^L \mathrm{d}x \, \rho^{\text{WL}} \left(\mu_0 H_{\text{tot}}(x, z_0) \right)$$

where z_0 is the height of the graphene above the YIG surface. The main features in the data we want to recover are: (i) the value of $\rho_0 = \rho(H_{\text{ext}}=0)$; (ii) an increase of ρ with H_{ext} in the (0, 100) Oe interval; (iii) a local maximum at $H_{\text{ext}} \approx 100$ Oe; (iv) WL-like tails for high values of H_{ext}.

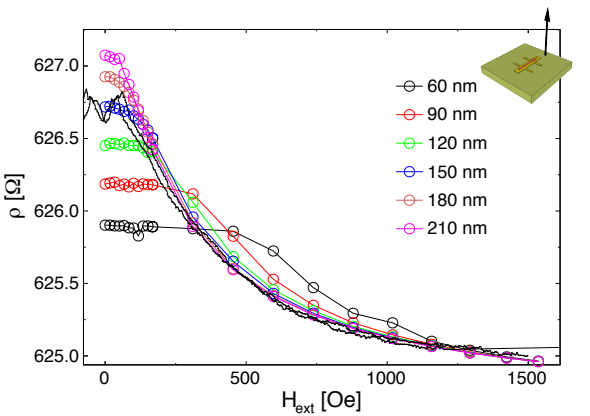

Figure 7.7: Calculation of the expected resistivity $\langle \rho \rangle$ after averaging in space the contributions of $\rho^{\text{WL}} \left(B(x, z_0) \right)$ over the length of the device, where the different colors are for different heights z_0 of the graphene over the YIG surface. It is clear how a the model lacks quantitative agreement, even for un-probable values of z_0. Measurements of ρ at 2K (same as in the main text) stand in the background.

In Figure 7.7 we show a selection of calculated curves for different values of the parameter z_0. On a qualitative level, we can see the WL tails (iv) and a shoulder for $H_{\text{ext}}>0$ (iii), but the quantitative analysis is not quite satisfactory, particularly for the data at small fields. In light of the analysis of the angular dependence of ρ^{WL}, we propose a picture where the changes in ρ are dominated by H_{str} for small fields, whereas above a threshold $H_{\text{tr}} \approx 200$ Oe the dominant contributor is H_{ext}. In this view, the model in [250] is still valid at small fields and it is interesting to ask how valid of an approximation a two-step-magnetization process would be. We adapt the model by changing the value of M_s, which is effectively a scaling factor for this model, and having it as a free parameter together with z_0 (results in the main text). As it turns out,

the data can be well described by this approximation, reproducing each of the (i)-(iv) features we are interested in.

Part IV

Concluding Remarks

8

Summary and Outlook

We have presented charge and spin transport in graphene devices with an experimental approach. After an introduction to graphene (Chapter 1) and to the specific equipment used for the fabrication (Chapter 2) and characterization (Chapter 3) of the devices, we analyzed the results obtained around three major topics: lateral spin valves, hot electron injection and transport in graphene transferred on a ferromagnetic insulator.

Spin valves are an established technique for characterizing the spin transport in metallic systems. Ferromagnetic (FM) contacts are used to induce an imbalance in the spin population of a non-magnetic material (NM), where the electronic transport is modeled as happening through two independent channels in parallel, one per spin degeneracy (the "two current model", [145]). In Chapter 4 we introduced the experimental designs of vertical and a lateral spin valves, the theoretical concepts of spin current density and spin polarization and the challenge presented by the conductivity mismatch issue [148].

Our study focused on spin transport in CVD graphene. We characterize the spin transport in graphene through two methods: firstly as a function of the distance between injector and detector electrodes and secondly as a function of a magnetic field perpendicular to the graphene surface (Hanle measurement). In both cases we obtain a spin diffusion length λ_s of the order of 1 µm at room temperature. The fact that these two different methods yield comparable results suggests that this is a good characterization of the spin transport. To further improve these devices, the most impactful breakthrough would probably be an improved reproducibility in the contact resistance, which some of

our evience suggests might be a function, among others, of the topography of the as-transferred graphene itself. The result of a λ_s = 1 µm is *per se* very interesting, as this is a very accessible length scale for today's micro- and nano-fabrication techniques.

In Chapter 6 explore the topic of hot electron injection. Although this technique was originally concived for STM-like setups, we show how it can also be realized in fully solid state devices. Such an on-chip hot-electrons device allows to extract relevant information about the energetics at a metal/semiconductor interface in operating conditions (as opposed to, for instance, an STM-like setup), by simply measuring the emitter-collector current I_{EC} as a function of the emitter-base voltage V_{EB}. The $I_{EC}(V_{EB})$ is approximately 0 up to a threshold value of V_{EB}, after which I_{EC} shows a linear behaviour. A first interpretation of the results relies on the linear extrapolation of this threshold value, which we directly relate to the height of the energy barrier at the metal/semiconductor interface. We suggest an improved modelling of the current through the device, which gives a further insight into the electrostatics at the interface. This second modelling not only estimates the height Δ_c of the energy barrier, but also gives an indication for the strength of the electric coupling at the interface through the fitting parameter σ_c.

Results of a preliminary study of the graphene-C_{60} interface for a possible hot-electron device were also shown. Instead of a hot-electron injection, in this case we presented a direct graphene-C_{60} junction, with a capacitive coupling between the graphene and a backgate electrode V_g. Most interestingly, the resistance of the device could be largely modulated (over three orders of magnitude) by V_g. A few considerations about the electrostatics of the system seemed to indicate that this modulation is primarily due to changes at the graphene-C_{60} junction, rather than the result of a modulation of the bulk resistivities of the materials. This is most interesting for applications where the contact resistance to a graphene channel is critical. Interesting developments here range from a more specific characterization of the graphene-C_{60} interface (for instance, by fabricating a full hot-electron device) to the generalization of this method to other materials. A very interesting achievement would see a similar (or improved) modulation of the resistance *versus* V_g with a reduced thickness of the semiconductor material.

Finally we considered the magnetotransport through graphene on YIG, a ferromagnetic insulator. We found a clear correlation between the sheet resistance ρ of the graphene and the magnetization **M** of the substrate, concerning

both intensity ad direction of **M**. We proposed that the coupling is mediated by weak localization in graphene, affected by the stray field of the underlying ferromagnet. We characterized the weak localization in our device by fitting our measurements to the standard weak localization theory for graphene [249] and separately modeled the stray field from the YIG as a function of the external magnetic field **H**. We discussed the limits of this model and used it to successfully reproduce our measurements. We also pointed out possible applications for this technique and its specific points of distinction to other, more established magnetometry techniques.

Overall, the interaction of graphene and magnetism emerges as an interesting and rich field, especially concerning CVD graphene and its promises for industrial scalability.

Resumen

El grafeno es una capa bidimensional (2D) de átomos de carbono conectados por enlaces sp^2. Electrónicamente el grafeno es un semi-metal sin banda prohibida con una relación de dispersión lineal para bajas densidades de portadores de carga, y ha mostrado un rendimiento excepcional en una gran variedad de medidas físicas, entre las que destacan la movilidad eléctrica (2.5×10^5 $cm^2V^{-1}s^{-1}$) [1], fuerza intrínseca (130 GPa) [2], impermeabilidad a los gases [3] y conductividad térmica (~ 2000 a 5300 W $m^{-1}K^{\wedge}$ -1^) [4].

El grafeno fue aislado por primera vez en 2004 [7] mediante disociación mecánica [7]. Otras formas comunes para fabricar grafeno son el crecimiento epitaxial [8], exfoliación líquida [9,10] y la deposición química desde fase vapor (CVD) [11]. Cada uno de estos métodos tiene sus ventajas y desventajas específicas, con la disociación mecánica siendo la más común en investigación fundamental y la CVD la más prometedora para aplicaciones a escala industrial en aplicaciones de alta movilidad eléctrica.

La estructura de bandas del grafeno fue calculada por primera vez por Wallance [100] y puede expresarse [99] como:

$$E(\mathbf{k}) = \pm V_{pp\pi}\sqrt{3 + 2\left[\cos(\mathbf{k}\cdot\mathbf{a}_1) + \cos(\mathbf{k}\cdot\mathbf{a}_2) + \cos(\mathbf{k}\cdot(\mathbf{a}_1 - \mathbf{a}_2))\right]}$$

donde $\mathbf{a}_1$ y $\mathbf{a}_2$ son los vectores de red del grafeno y $V_{pp\pi}$ es el integral de superposición entre los orbitales p_z. Las superficies $E(\mathbf{k})$ muestran los puntos en el espacio de momento en el que las bandas superiores e inferiores se unen: estos puntos se llaman *Dirac points* (K-points). Cerca de estos puntos la estructura de bandas es lineal, como se puede ver mediante la expansión en el entorno de $\mathbf{k} = \mathbf{k} + \mathbf{q}$:

$$E(\mathbf{q}) \approx \pm\hbar v_F|\mathbf{q}| \qquad v_F = \frac{3}{2}\frac{V_{pp\pi}d_0}{\hbar}$$

Dopando el grafeno se puede cambiar de forma continua entre portadores de carga de tipo electrones o huecos, mientras que el valor de energía $E(\mathbf{q} = 0)$

corresponde al nivel de Fermi intrínseco del grafeno. Es posible cambiar la energía del punto de Dirac mediante la realización de transistores de efecto de campo en los que el grafeno sirve como canal de conducción, y se puede controlar su densidad superficial de portadores de carga, n_s, por medio de una puerta electrostática.

Fabricación de dispositivos

Las principales etapas de fabricación para los dispositivos de grafeno típicamente implican técnicas de litografía, eliminación y deposición de metales. En nuestro caso particular, usamos litografía por haz de electrones (EBL) para definir la geometría específica de nuestros dispositivos sobre las muestras de grafeno CVD. La litografía consiste en cubrir la muestra con una película polimérica (en nuestro caso, PMMA) y localmente irradiar el polímero con electrones a una alta energía (~10 kV). Tras la irradiación, el PMMA se vuelve soluble en un tipo específico de producto químico nombrado *revelador* (en nuestro caso, metilisobutilcetona, o MIBK), lo que permite la eliminación local del polímero. La muestra puede ser expuesto a una etapa de grabado (en nuestro caso, Reactive Ion Etching) para la eliminación parcial del grafeno o a una etapa de deposición de metal (en nuestro caso, la evaporación de metal o de pulverización catódica) para la fabricación de contactos metálicos. En última instancia, la muestra se sumerge en un baño de acetona, que elimina el PMMA y los eventuales residuos metálicos depositados sobre ella.

Tecnicas de caracterización

Hacemos un seguimiento de la calidad de la fabricación con una serie de diferentes técnicas de caracterización, siendo las más relevantes la microscopia óptica, la microscopia electrónica (SEM) y la espectroscopia Raman. El grafeno muestra unos rasgos característicos en su espectro de Raman, tales como un pico a ≈1580 cm^{-1} (G-peak) y una banda a ≈2700 cm^{-1} (2D-peak). La intensidad relativa entre los dos, así como la anchura de la banda 2D, se pueden utilizar como un indicador del número de capas de grafeno. Toda la información obtenida por espectroscopia Raman es local, por lo que se puede utilizar para determinar las áreas cubiertas por grafeno y las libres de el, así como para monitorizar los cambios en el pico G o 2D sobre la superficie de grafeno.

En nuestra experiencia también se ha demostrado útil para aportar información sobre el origen de los residuos que permanecen en el grafeno después del proceso de fabricación, residuos que no se pudo eliminar por medios convencionales (es decir, recocido o solventes químicos). Los resultados sugieren que una técnica de grabado específico (el *ion milling*) podría causar un endurecimiento inesperado del polímero, que posteriormente se transforma por la exposición al láser Raman. Esta información nos ayudó en la elección de una técnica de grabado específica para el proceso de fabricación.

Los dispositivos fueron caracterizados eléctricamente a diferentes temperaturas (2-300 K) y campos magnéticos (0-9 T). En la geometría de transistor de efecto de campo (FET), reproducimos la típica modulación de la resistividad del grafeno en función de la tensión de puerta aplicada: encontramos el máximo de la resistencia a una tensión de puerta de 40-60 V (en oposición a 0 V), con valores típicos de la movilidad ~1000 $cm^2V^{-1}s^{-1}$.

Junto con las mediciones de FET, también hacemos mediciones de magnetorresistencia (MR), en particular a través del efecto Hall, donde un voltaje V_{xy} se mide transversal a una corriente eléctrica aplicada I, en función de un campo magnético externo B. Esta configuración permite extraer la movilidad μ del grafeno a diferentes valores de voltaje de puerta V_g. Este método, en nuestra experiencia, arroja valores de μ compatibles a los obtenidos por medidas FET.

Espintronica: introductión

Posteriormente, dirigimos nuestra investigación sobre el transporte de espín en dispositivos de grafeno. En este campo, el transporte electrónico se modela a través de dos canales independientes y en paralelo, uno por degeneración de espín [145], por lo que la conductividad se puede escribir $\sigma = \sigma_\uparrow + \sigma_\downarrow$. Esta sencilla imagen se aplica si el espín del electrón se conserva a lo largo de toda la trayectoria de conducción. Este es típicamente el caso en las válvulas de espín locales, donde dos conductores ferromagnéticos (FM) están separados por una delgada capa no magnética (NM). El sistema FM-NM-FM puede presentarse en dos geometrías: una denominada *vertical*, donde las capas se apilan una encima de la otra, y una *lateral*, donde el material NM forma en un canal alargado que conecta los dos electrodos FM. En ambos casos el objetivo es crear una corriente polarizada de espín a través de un material NM, donde por definición su estado fundamental es sin polarización de espín.

Podemos definir el transporte por medio de la densidad de corriente de espín $j_S = j_\uparrow - j_\downarrow$ y la densidad de corriente de carga $j = j_\uparrow + j_\downarrow$. En un material ferromagnético, $\sigma_\uparrow \neq \sigma_\downarrow$, dando una polarización de espín $P \neq 0$:

$$P \overset{def}{=} \frac{j_\uparrow - j_\downarrow}{j_\uparrow + j_\downarrow} = -\frac{\sigma_\uparrow - \sigma_\downarrow}{\sigma_\uparrow + \sigma_\downarrow}$$

Una descripción exacta del transporte de espín debe incluir tres regiones distintas, la FM, el NM y la interfaz FM/NM. En la proximidad de la interfaz un flujo de corriente de espín polarizado del FM al NM va a generar una acumulación de espín en el NM, que se difundirá en su mayor parte en el NM, disminuyendo con una longitud de decaimiento λ_s^{NM}. La población de espín también se puede difundir de nuevo en el FM, de modo que la dependencia espacial de $\mu_s = (\mu_\uparrow - \mu_\downarrow)/2$ varía a través de la interfaz.

La evolución de la población de espín se describe por la ecuación Bloch [149]

$$\frac{\mathrm{d}\boldsymbol{\mu}_s}{\mathrm{d}t} = D\nabla^2\boldsymbol{\mu}_s - \frac{\boldsymbol{\mu}_s}{\tau_s} + \boldsymbol{\omega}_L \times \boldsymbol{\mu}_s$$

donde τ_s es el tiempo de relajación del espín, D la constante de difusión y $\boldsymbol{\omega}_L = \frac{g\mu_B}{\hbar}\mathbf{B}$, g siendo el factor giromagnético, μ_B el magnetón de Bohr, $\hbar$ la constante de Planck y $\mathbf{B}$ el campo magnético. La ecuación de Bloch captura la difusión de espín, su relajación y su precesión alrededor de un campo magnético de una forma muy general. Intuitivamente, el valor de μ_s en el punto de inyección en el NM dependerá de la polarización del material ferromagnético y en la dispersión de espín que la interfaz podría introducir. Sin embargo, incluso con una polarización ideal $P = 1$ y sin dispersión de espín en la interfaz, la polarización P_N en el punto de inyección puede desaparecer simplemente por las resistencias eléctricas particulares presentes en el dispositivo. Este problema se conoce como el desajuste de conductividad [150,151] y es un tema relevante para la inyección de espín en el grafeno [152,153]. Este problema por sí solo puede hacer la diferencia entre una señal medible y un dispositivo que no funciona. Según lo demostrado en [148], la introducción de una barrera resistiva en la interfaz proporciona una forma de controlar la polarización P_N en el canal [149]:

$$R_{NL} = \frac{V}{I} = \pm\frac{1}{2}P_I^2 R_N e^{-L/\lambda_N}$$

donde L es la distancia entre los electrodos y P_i la polarización en la interfaz.

Como barremos la magnitud de un campo magnético externo en el plano, la alineación relativa entre la magnetización del inyector y del detector cambia entre paralela y anti-paralela, con los dos estados produciendo dos diferentes valores de resistencia no local. La manera mas intuitiva para la medición de la longitud de difusión de espín es mapear la amplitud ΔR_{NL} de la señal no local como una función de la separación entre el inyector y el detector.

El transporte de espín se puede caracterizar también por medio del efecto Hanle. En el caso específico de una válvula de espín lateral, un campo magnético externo se usa primero para magnetizar los electrodos en el plano de la muestra, dejándolos en su estado remanente. La señal de espín no local se mide en función de un campo magnético directo fuera del plano $B_\perp$. Para $B_\perp \neq 0$, los espines inyectados en el canal precesan y a la vez difunden, lo que se traduce en una dependencia de la señal R_{NL} en la intensidad de $B_\perp$. La dependencia de la señal no local es

$$R_{NL}(B_\perp) = \pm \frac{P_I^2 R_N D}{w_N} \int_0^\infty \mathrm{d}t \; P(t) \cos(\omega_L t) \exp(-t/\tau_s)$$

Ajustando esta fórmula a los dados medidos por Efecto Hanle podemos extraer los parámetros de difusión de espín, como D y τ_s.

Válvulas de espín sobre grafeno CVD

Nuestra estrategia típica de fabricación se basa en Litografía por haz de electrones (EBL). En un proceso litográfico de varios pasos, queremos en primer lugar definir marcas de alineación (marcas en forma de cruz en la superficie de la muestra, que se define por EBL, deposición de metal y despegue), en segundo lugar, definir el canal de grafeno (EBL y grabado por plasma), en tercer lugar lugar los electrodos ferromagnéticos (EBL, deposición de metal y liftoff) y por último los contactos macroscópicos (EBL, deposición de metal y liftoff). Una receta típica de fabricación se puede encontrar en la tabla 5.1.

El proceso es largo y articulado. Lo simplificamos mediante el uso de un solo tipo de polímero para la litografía, la optimización de un número limitado de ajustes para la EBL y el fijar un tiempo de development. Con el fin de proteger el grafeno a partir de residuos de PMMA, podemos cubrir toda la muestra con

un película de AlO_x de pocos nm de espesor *a priori*, de modo que la siguiente litografía sólo entra en contacto con al AlO_x, que en última instancia puede ser eliminado por ataque químico. Sin embargo, en nuestra experiencia esto es incompatible con el paso del grabado del grafeno. Un enfoque diferente es reducir el número de recubrimientos de PMMA, que resulta ser viable pero introduje una mayor complejidad en el proceso de fabricación.

El grabado del grafeno se realiza con mayor frecuencia a través de plasma de oxígeno [7,181–184], más típicamente en menos de 30 s y 50 W de potencia. Sin embargo, en nuestro caso los resultados más limpios se obtuvieron mediante Reactive Ion Etching en una atmósfera de Ar y O_2.

Un método común para aliviar el desajuste de conductividad [150,177,187] es aumentar la resistencia de interfaz en la unión FM/NM mediante la introducción de una capa dieléctrica (típicamente AlO_x, TiO_x o MgO) entre los dos conductores. Esto se aplica también para el caso de grafeno: válvulas de espín laterales con grafeno(/TiO_x)/AlO_x/Co [152,159,188], grafeno (/TiO_x)/MgO/Co [189], uniones grafeno/MgO/Py [190] y otros [191,192] están reportadas en la literatura.

La uniformidad de la capa de AlO_x es clave para un control reproducible sobre la resistencia de la interfaz. El crecimiento de una tal capa sobre el grafeno es notoriamente difícil debido a una mala humectación del Al sobre el grafeno. Investigamos algunas estrategias y, todo considerado, la evaporación del metal y su oxidación natural resultó ser la más fiable.

Entre los resultados conseguidos, eseñamos unos dispositivos de válvula de espín lateral donde mapeamos la amplitud ΔR_{NL} de la señal no local como una función de la separación entre el inyector y el detector. Las separaciones entre los electrodos varían entre 0.5 y varios µm. El valor de la longitud de correlación de spin que podemos extraer de nuestros datos experimentales es λ_s = 1.0 ± 0.26 µm.

También medimos la señal Hanle en nuestros dispositivos. La señal medida debe ser corregida por el hecho de que la magnetización de los electrodos FM gira fuera del plano en un ángulo $\vartheta(B_\perp)$ para valores grandes de $B_\perp$. Con el fin de dar cuenta de esto, la señal se reescribe como [149,207]:

$$R^P_{NL}(B_\perp) = |R_{NL}(0)| \frac{R^P_{NL}(B_\perp, \vartheta) - R^{AP}_{NL}(B_\perp, \vartheta)}{2|R_{NL}(0)| - [R^P_{NL}(B_\perp, \vartheta) + R^{AP}_{NL}(B_\perp, \vartheta)]}$$

La evaluación de $\vartheta(B_\perp)$ no requiere una caracterización AMR adicional de los electrodos, siempre que ambas mediciones P y AP estén disponibles. En la Figura 5.6 enseñamos el resultado de esta análisis. Se obtiene una longitud de difusión de espín $\lambda_s = \sqrt{D\tau_s} \approx 1$ µm.

Ajuste de la inyección

Ampliamos nuestra investigación sobre algunas otras opciones para la inyección eléctrica en el grafeno, es decir, la inyección de *hot electrons*. Los portador de carga se consideran *hot* cuando su energía ϵ es muy superior a la energía de Fermi ε_F en comparación con la energía térmica k_BT, es decir, ε - $\varepsilon_F \gg k_BT$. Esta condición normalmente se realiza en microscopía balística de emisión de electrones (BEEM), pero la misma comprensión se puede aplicar a un dispositivo plenamente de estado sólido, donde la capa de vacío está sustituida por un material aislante [222,223]. Consideramos un dispositivo basado en metal con una capa molecular de C_{60} como colector. Los dispositivos se fabrican como una estructura vertical de las diferentes capas, depositadas en condiciones de ultra alto vacío.

Cuando se aplica un voltaje V_{EB} entre emisor y base, los electrones túnelean a través del AlO_x y se propagan a través de la base, con una fracción de ellos que llegar a la interfaz de entre base y colector. Cuando V_{EB} es menor que la barrera base-colector Δ_c, la corriente emisor-colector I_{CE} se suprime, mientras por $V_{EB} > \Delta_c$ esperamos un más o menos lineal [216] aumento de I_{CE}. Una vez en el semiconductor, los electrones termalizan rápidamente [222] y se difunden hasta el }electrodo de Al. Podemos extraer información relevante que se puede extraer de la corriente de *hot electrons*. Consideramos un modelado de transporte balístico 1-dimensional, de un material con densidad de estados $g_1(\epsilon)$ a un segundo con densidad de estados $g_2(\epsilon)$ y obtenemos una corriente neta de

$$I_{21} = \frac{e}{h} \int \mathrm{d}\epsilon \, g_1(\epsilon) g_2(\epsilon) [f(\epsilon - \epsilon_F + eV_{\mathrm{Bias}}) - f(\epsilon - \epsilon_F)] T_{2,1}(\epsilon)$$

donde hemos supuesto que se aplique un voltaje V_{Bias} entre los dos conductores y añadimos un término $T_{2,1}$ para dar cuenta de las resistencias de interfaz (es decir $T_{2,1}(\epsilon) = 1$ para uniones óhmicas transparentes y $T_{2,1}(\epsilon) = 0$ para uniones absolutamente aislantes). Después de algunas consideraciones, obtenemos

$$\frac{I_{EC}}{I_{EB}} = \alpha \frac{\int \mathrm{d}\epsilon \, \left[f(\epsilon - eV_{EB}) - f(\epsilon) \right] e^{\epsilon/\lambda_\epsilon} g_C(\epsilon)}{\int \mathrm{d}\epsilon \, \left[f(\epsilon - eV_{EB}) - f(\epsilon) \right] e^{\epsilon/\lambda_\epsilon}}$$

donde los índices E, B, C reposan por emisor, base y colector. Para describir de forma realista la interfaz entre moléculas y metal, consideramos una función específica para $g_C(\epsilon)$. En la interfaz, los niveles energéticos moleculares se amplían debido a la interacción con la superficie metálica, con una ampliación que puede ser aproximada por una curva de Gauss o una distribución de Lorentz [218,219,229]. Por lo tanto, aproximamos la densidad de estados en el C_{60} como

$$g_C(\epsilon) = \begin{cases} \beta \exp\left[-\frac{1}{2} \left(\frac{E - \Delta_c}{\sigma_c} \right)^2 \right] & \text{for } E < \Delta_c \\ 1 & \text{for } E > \Delta_c \end{cases}$$

Por encima del LUMO hay otros niveles moleculares que están disponibles, que también se amplían y se hibridan con el LUMO. Por lo tanto, aproximamos la densidad de estados por encima del LUMO con un continuo de estados sin rasgos distintivos. Tal aproximación es bastante burda, pero en la región de interés (es decir, $eV_EB \approx \Delta_c$) el aumento de I_{CE} en comparación con una aproximación lineal se determina por la ampliación de $g_C(\epsilon)$.

Fabricamos y caracterizamos tres dispositivos diferentes de *hot electrons*, con bases de $Ni_{80}Fe_{20}$, Au y Cu. Las mediciones se ajustan a nuestro modelo, y extraemos los valores de λ_ϵ (que caracteriza la barrera túnel), Δ_c y σ_c, (que caracterizan la densidad de estados en el semiconductor).

En la Tabla 6.1 resumimos los hallazgos tanto para la extrapolación lineal Δ_{lin} y el método aquí desarrollado. La primera observación que podemos hacer es que los valores de la barrera base/semiconductor extraídos por los dos son coherentes con $\Delta_{\text{lin}} = \Delta_c - \sigma_c$. La interpretación trivial aquí es que una gran parte de los electrones balísticos encontrar una barrera efectiva en $\Delta_c - \sigma_c$, que da lugar a una inyección en la C_{60} a energías por debajo del LUMO. Además, observamos que los valores de Δ_c y Δ_{lin} para NiFe son mayores que para el Au y Cu, lo que no esperaríamos basándonos únicamente en la análisis de las funciones de trabajo.

En la perspectiva de la fabricación de un dispositivo de *hot electrons* con el grafeno, empezamos por caracterizar la interfaz entre grafeno y C_{60}, sobre todo

en función de una tensión de puerta aplicada. La Figura 6.4 enseña el dispositivo. Una capa de grafeno CVD es transferida sobre un sustrato de Si++/SiO2 en una geometría similar a la FET. Litografía y RIE definen un canal de grafeno de 2 mm de largo y 100 µm de ancho, con electrodos de Ti/Au (definidos por litografía y evaporación de metal) para el contacto eléctrico. Una capa de C_{60} de 280 nm de espesor se evapora sobre la muestra en ultra alto vacío (UHV) a través de una máscara rígida, definiendo una barra transversal al grafeno y una área de unión grafeno/C_{60} de 1 mm × 100 µm.

El transporte a través de todo el dispositivo depende de manera significativa en el valor de la tensión de puerta V_g, como se muestra en la Figura 6.5. Una barrera de energía a la interfaz entre grafeno y C_{60} la candidata ideal para explicar las características de rectificación del dispositivo. De una manera similar como en la unión base-colector, podemos suponer una barrera de energía en la interfaz grafeno/C_{60} donde el LUMO del C_{60} está a una energía más alta que el nivel de Fermi, bloqueando el transporte en una dirección. La sugerencia interesante que emerge es que esta barrera de interfaz modula con la tensión de puerta.

Los modelos discutidos para inyección de hot electrons no son directamente aplicables en este caso. El transporte a través de todo el dispositivo no es balístico y no podemos cuantificar la caída exacta de tensión en la interfaz grafeno/C_{60} solamente al saber V_{ds}. Podemos, sin embargo, explorar cómo estas cantidades dependerán de V_g. El conectar a tierra del grafeno tiene la importante consecuencia de que todo el efecto de campo de la tensión de puerta debe limitarse al grafeno. Esta observación nos permite concluir que, aunque no podemos extraer el valor exacto de la barrera, podemos evaluar su modulación en función de la tensión de puerta al examinar los cambios de en $I_{ds}(V_{ds})$ por diferentes valores de V_g. En la Figura 6.5 podemos ver que I_{ds} cambia más de tres órdenes de magnitud como consecuencia de los cambios en la barrera de grafeno/C_{60}. Si dicha interfaz se fuera a utilizar para la inyección de corrientes de espín, su gran capacidad de ajuste de resistencia podría ser muy útil en para superar el desajuste de conductividad.

Acknowledgements

This work bares the name of only one author, but it comes with the fingerprints of many others.

I would like to thank my supervisor Luis Hueso. Working in the Nanodevices group at Nanogune has been a tremendous opportunity, from resources to connections, neither of which I ever felt short of. I had a chance not only to learn about nanodevices, but also to design, make, image and operate them myself. I am especially thankful for the degree of autonomy you entrusted me with, allowing me to test my own ideas and make my (often not so original) mistakes, which have been a building block of this work. I also value how you have been so easily reachable all along these 3+ years, both in terms of professional and personal feedback, and how you have stubbornly tried to teach me scientific English writing, despite my fierce oppositions.

I also received the unofficial supervision of a few others, which have contributed to major steps in my understanding. I am most thankful for the scrupulously detailed supervision I received from Fèlix in building my knowledge of spintronics, for the vastness of fabrication knowledge I got from Fede, particularly in my first year, and to Roger for his patience with me while I was learning basic electronics, Labview ..or just how not to hurt myself in the lab. Pablo is also part of this group: I am doubly thankful here, not only for the source of knowledge you represented for me, but also for the sense of esteem you constantly transmit in our chats.

This experience was definitely shaped by my peer members in the nanodevices group, past and current ones, which I like to remember during a typical Friday meeting, sitting all in a single room so filled up that we often had to look for extra chairs. Around the table I would see the 2D-materials team with Wenjing, Oihana, Saül and Mario, to whom I am most thankful for sharing the needy greedy challenges of fabricating and measuring (and coping with) such extremely delicate devices. Roughly in front of the screen, I would find the spin valve masters Estitxu (aka, fraking ez) and Miren, invariably side by side, while Libe, Subir, Ainhoa and Edurne would be scattered here and there. Most

interestingly, I like to imagine this table with Xiagnan giving his presentation, Amilcar somehow always finding a question to ask, David making a *soft* comment and Marco radiating a happy smile at the general picture. To this group of people I am thankful for shaping such a happy and welcoming atmosphere in the group, which constitutes the backbone of every day in nanogune, day in and day out.

Mano deserves a special recognition from my side. I feel like we have been sharing everything this PhD has been about and is not written in this thesis, from partying to physics. I am very thankful for the trust and friendship we experienced: Ευχαριστώ, Mano ..and à tout à l'heure!!

As all Nanogune knows, the Italian gang is definitely a thing. Grazie mille a Nicolo', Lorenzo, Matteo, Michele, Andrea e Mario: le grasse risate sono state equiparabili solo alle grasse abbuffate ^^. Special thanks to Fabiano for baring with me in all my geekiest moments, be it movie marathons or quantum mechanics.

A characterizing part of my PhD experience has been the time I spent abroad, and I am most thankful to the Marie Skłodowska-Curie funding for making it possible. My thanks go to Hervé for managing the whole Q-NET project, to the researchers who made it happen, and particularly to those who have hosted me visiting their groups, Christopher Marrows, Klaus Ensslin and Jari Penttilä. The group of PhD students and post-docs is a formidable one and I am very happy we were able to connect quickly on an informal basis. I would specially like to mention here Robert and Pauline, with whom I felt as if we were members of the same group during my visits.

None of this would have happened had I not have the support, the trust and the caring of my family at home, for which I feel blessed.

Bibliography

[1]A. S. Mayorov et al., ”Micrometer-scale ballistic transport in encapsulated graphene at room temperature”, *Nano Lett.* **11**, 2396 (2011).

[2]C. Lee et al., ”Measurement of the elastic properties and intrinsic strength of monolayer graphene”, *Science* **321**, 385 (2008).

[3]J. S. Bunch et al., ”Impermeable atomic membranes from graphene sheets”, *Nano Lett.* **8**, 2458 (2008).

[4]A. A. Balandin, ”Thermal properties of graphene and nanostructured carbon materials”, *Nat Mater* **10**, 569 (2011).

[5]a K. Geim and K. S. Novoselov, ”The rise of graphene”, *Nat. Mater.* **6**, 183 (2007).

[6]S. Hembacher et al., ”Revealing the hidden atom in graphite by low-temperature atomic force microscopy”, *Proc. Natl. Acad. Sci. U. S. A.* **100**, 12539 (2003).

[7]K. S. Novoselov et al., ”Electric field effect in atomically thin carbon films”, *Science* **306**, 666 (2004).

[8]K. V. Emtsev et al., ”Towards wafer-size graphene layers by atmospheric pressure graphitization of silicon carbide”, *Nat. Mater.* **8**, 203 (2009).

[9]Y. Hernandez et al., ”High-yield production of graphene by liquid-phase exfoliation of graphite”, *Nat. Nanotechnol.* **3**, 563 (2008).

[10]P. Blake et al., ”Graphene-based liquid crystal device”, *Nano Lett.* **8**, 1704 (2008).

[11]X. Li et al., ”Large-area synthesis of high-quality and uniform graphene films on copper foils”, *Science* **324**, 1312 (2009).

[12]N. Mermin, ”Crystalline order in two dimensions”, *Phys. Rev.* **176**, 250 (1968).

[13]K. S. Novoselov et al., ”Two-dimensional atomic crystals”, *Proc. Natl. Acad. Sci. U. S. A.* **102**, 10451 (2005).

[14]A. Fasolino, J. H. Los, and M. I. Katsnelson, ”Intrinsic ripples in graphene”, *Nat. Mater.* **6**, 858 (2007).

[15]Y.-W. Son, M. L. Cohen, and S. G. Louie, ”Energy Gaps in Graphene Nanoribbons”, *Phys. Rev. Lett.* **97**, 1 (2006).

[16]S. Iijima, ”Helical microtubules of graphitic carbon”, *Nature* **354**, 56 (1991).

[17]M. Arndt et al., ”Wave-particle duality of C(60) molecules”, *Nature* **401**, 680 (1999).

[18]A. C. Ferrari et al., ”Science and technology roadmap for graphene, related two-dimensional crystals, and hybrid systems”, *Nanoscale* **7**, 4598 (2014).

[19]F. Bonaccorso et al., ”Production and processing of graphene and 2d crystals”, *Mater. Today* **15**, 564 (2012).

[20]Z. H. Ni et al., ”On resonant scatterers as a factor limiting carrier mobility in graphene”, *Nano Lett.* **10**, 3868 (2010).

[21]D. C. Elias et al., ”Dirac cones reshaped by interaction effects in suspended graphene”, *Nat. Phys.* **7**, 701 (2011).

[22]A. S. Mayorov et al., ”How Close Can One Approach the Dirac Point in Graphene”, *Nano Lett.* **12**, 4629 (2012).

[23]P. Neugebauer et al., ”How perfect can graphene be?”, *Phys. Rev. Lett.* **103**, 136403 (2009).

[24]T. Moldt et al., ”High-yield production and transfer of graphene flakes obtained by anodic bonding”, *ACS Nano* **5**, 7700 (2011).

[25]A. Shukla et al., ”Graphene made easy: High quality, large-area samples”, *Solid State Commun.* **149**, 718 (2009).

[26]S. Dhar et al., ”A new route to graphene layers by selective laser ablation”, *AIP Adv.* **1**, 1 (2011).

[27]S. Lee et al., ”Laser-synthesized epitaxial graphene”, *ACS Nano* **4**, (2010).

[28]M. Qian et al., ”Formation of graphene sheets through laser exfoliation of highly ordered pyrolytic graphite”, *Appl. Phys. Lett.* **98**, 98 (2011).

[29]M. Reininghaus et al., ”Laser induced non-thermal deposition of ultrathin graphite”, *Appl. Phys. Lett.* **100**, 22 (2012).

[30]O. M. Maragó et al., ”Brownian motion of graphene”, *ACS Nano* **4**, 7515 (2010).

[31]M. Lotya et al., ”Liquid Phase Production of Graphene by Exfoliation of Graphite in Surfactant / Water Solutions Liquid Phase Production of Graphene by Exfoliation of Graphite in Surfactant / Water Solutions”, *J. Am. Chem. Soc.* **131**, 3611 (2009).

[32]T. Hasan et al., ”Solution-phase exfoliation of graphite for ultrafast photonics”, *Phys. Status Solidi Basic Res.* **247**, 2953 (2010).

[33]M. Lotya et al., ”High-concentration, surfactant-stabilized graphene dispersions”, *ACS Nano* **4**, 3155 (2010).

[34]J. Hassoun et al., ”A lithium-ion battery based on a graphene nanoflakes ink anode and a lithium iron phosphate cathode”, *Nano Lett.* **14**, 4901 (2014).

[35]U. Khan et al., ”High-Concentration Solvent Exfoliation of Graphene”, *Small* **6**, 864 (2010).

[36]F. Torrisi et al., ”Inkjet-printed graphene electronics”, *ACS Nano* **6**, 2992 (2012).

[37]J. W. Williams et al., ”The theory of sedimentation analysis”, *Chem. Rev.* **58**, 715 (1958).

[38]A. O’Neill et al., ”Graphene dispersion and exfoliation in low boiling point solvents”, *J. Phys. Chem. C* **115**, 5422 (2011).

[39]C. Berger et al., ”Ultrathin epitaxial graphite: 2D electron gas properties and a route toward graphene-based nanoelectronics”, *J. Phys. Chem. B* **108**, 19912 (2004).

[40]A. Van Bommel, J. Crombeen, and A. Van Tooren, ”LEED and Auger electron observations of the SiC (0001) surface”, *Surf. Sci.* **48**, 463 (1975).

[41]I. Forbeaux et al., ”Solid-state graphitization mechanisms of silicon carbide 6H–SiC polar faces”, *Appl. Surf. Sci.* **162**, 406 (2000).

[42]A. Charrier et al., ”Solid-state decomposition of silicon carbide for growing ultra-thin heteroepitaxial graphite films”, *J. Appl. Phys.* **92**, 2479 (2002).

[43]E. G. Acheson, ”Manufacture of Graphite”, (1896).

[44]C. Riedl et al., ”Quasi-free-standing epitaxial graphene on SiC obtained by hydrogen intercalation”, *Phys. Rev. Lett.* **103**, 246804 (2009).

[45]K. V. Emtsev et al., ”Interaction, growth, and ordering of epitaxial graphene on SiC (0001) surfaces: A comparative photoelectron spectroscopy study”, *Phys. Rev. B - Condens. Matter Mater. Phys.* **77**, 155303 (2008).

[46]J. Hass et al., ”Highly ordered graphene for two dimensional electronics”, *Appl. Phys. Lett.* **89**, 23 (2006).

[47]J. Hass et al., ”Interface structure of epitaxial graphene grown on 4H-SiC(0001)”, *Phys. Rev. B - Condens. Matter Mater. Phys.* **78**, 1 (2008).

[48]W. a. de Heer et al., ”Large area and structured epitaxial graphene produced by confinement controlled sublimation of silicon carbide”, *Proc. Natl. Acad. Sci. U. S. A.* **108**, 16900 (2011).

[49]W. A. de Heer, ”The Development of Epitaxial Graphene For 21st Century Electronics”, *ArXiv Prepr. ArXiv1012.1644* (2010).

[50]J. Baringhaus et al., ”Exceptional ballistic transport in epitaxial graphene nanoribbons”, *Nature* **506**, 349 (2014).

[51]J. Kedzierski et al., ”Epitaxial graphene transistors on SiC substrates”, *Electron Devices, IEEE Trans.* **55**, 2078 (2008).

[52]Y.-M. Lin et al., ”100-GHz transistors from wafer-scale epitaxial graphene”, *Science* **327**, 662 (2010).

[53]K. S. A. Novoselov et al., ”Two-dimensional gas of massless Dirac fermions in graphene”, *Nature* **438**, 197 (2005).

[54]Y. Zhang et al., ”Experimental observation of the quantum Hall effect and Berry’s phase in graphene”, *Nature* **438**, 201 (2005).

[55]X. Du et al., ”Fractional quantum Hall effect and insulating phase of Dirac electrons in graphene”, *Nature* **462**, 192 (2009).

[56]T. J. B. M. Janssen et al., ”Quantum resistance metrology using graphene”, *Reports Prog. Physics.* **76**, 104501 (2013).

[57]T. J. McArdle et al., ”Multilayer epitaxial graphene formed by pyrolysis of polycrystalline silicon-carbide grown on c-plane sapphire substrates”, *Appl. Phys. Lett.* **98**, 132108 (2011).

[58]O. Alexander N., ”Making graphene on a large scale”, *Nat. Nanotechnol.* **4**, 212 (2009).

[59]W. Liu et al., ”Synthesis of High-Quality Monolayer and Bilayer Graphene on Copper using Chemical Vapor Deposition”, *Carbon N. Y.* **49**, 4122 (2011).

[60]G. Ruan et al., ”Growth of graphene from food, insects, and waste”, *ACS Nano* **5**, 7601 (2011).

[61]Z. Sun et al., ”Growth of graphene from solid carbon sources”, *Nature* **468**, 549 (2010).

[62]Y. Miyasaka, A. Nakamura, and J. Temmyo, ”Graphite thin films consisting of nanograins of multilayer graphene on sapphire substrates directly grown by alcohol chemical vapor deposition”, *Jpn. J. Appl. Phys.* **50**, (2011).

[63]A. Guermoune et al., ”Chemical vapor deposition synthesis of graphene on copper with methanol, ethanol, and propanol precursors”, *Carbon N. Y.* **49**, 4204 (2011).

[64]Y. Miyata et al., ”A simple alcohol-chemical vapor deposition synthesis of single-layer graphenes using flash cooling”, *Appl. Phys. Lett.* **96**, 263105 (2010).

[65]A. E. Karu and M. Beer, ”Pyrolytic formation of highly crystalline graphite films”, *J. Appl. Phys.* **37**, 2179 (1966).

[66]K.-R. Peters, ”Precise and reproducible deposition of thin and ultrathin carbon films by flash evaporation of carbon yarn in high vacuum”, *J. Microsc.* **133**, 17 (1984).

[67]H. Lipson and A. R. Stokes, ”The Structure of Graphite”, *Proc. R. Soc. London.* **181**, 101 (1942).

[68]J. Biscoe and B. E. Warren, ”An X-Ray Study of Carbon Black”, *J. Appl. Phys.* **13**, 364 (1942).

[69]G. L. S. Werner Kern, ”Low-Pressure Chemical Vapor Deposition for Very large-scale integration processing- A Review”, *Electron Devices, IEEE Trans.* **26**, 647 (1979).

[70]X. Li et al., ”Evolution of graphene growth on Ni and Cu by carbon isotope labeling”, *Nano Lett.* **9**, 4268 (2009).

[71]X. Li et al., ”Graphene films with large domain size by a two-step chemical vapor deposition process”, *Nano Lett.* **10**, 4328 (2010).

[72]N. Petrone et al., ”Chemical Vapor Deposition-Derived Graphene with Electrical Performance of Exfoliated Graphene”, *Nano Lett.* (2012).

[73]X. Li et al., ”Large-area graphene single crystals grown by low-pressure chemical vapor deposition of methane on copper”, *J. Am. Chem. Soc.* **133**, 2816 (2011).

[74]Y. Hao et al., "The role of surface oxygen in the growth of large single-crystal graphene on copper", *Science* **342**, 720 (2013).

[75]X. Li et al., "Transfer of large-area graphene films for high-performance transparent conductive electrodes", *Nano Lett.* **9**, 4359 (2009).

[76]Z. Yan et al., "Toward the synthesis of wafer-scale single-crystal graphene on copper foils", *ACS Nano* **6**, 9110 (2012).

[77]Z. Luo et al., "Effect of substrate roughness and feedstock concentration on growth of wafer-scale graphene at atmospheric pressure", *Chem. Mater.* **23**, 1441 (2011).

[78]B. Zhang et al., "Low-temperature chemical vapor deposition growth of graphene from toluene on electropolished copper foils", *ACS Nano* **6**, 2471 (2012).

[79]D. Yoon, Y. Son, and H. Cheong, "Negative Thermal Expansion Coefficient of Graphene Measured by Raman Spectroscopy", *Nano Lett.* **99**, 161103 (2011).

[80]R. Addou et al., "Monolayer graphene growth on Ni(111) by low temperature chemical vapor deposition", *Appl. Phys. Lett.* **100**, (2012).

[81]D. Kondo et al., "Low-temperature synthesis of graphene and fabrication of top-gated field effect transistors without using transfer processes", *Appl. Phys. Express* **3**, (2010).

[82]M.-y. Lin et al., "Low-temperature grown graphene films by using molecular beam epitaxy", *Appl. Phys. Lett.* **101**, (2012).

[83]W. Strupinski et al., "Graphene epitaxy by chemical vapor deposition on SiC", *Nano Lett.* **11**, 1786 (2011).

[84]M. a. Fanton et al., "Characterization of graphene films and transistors grown on sapphire by metal-free chemical vapor deposition", *ACS Nano* **5**, 8062 (2011).

[85]J. Sun et al., "Large-area uniform graphene-like thin films grown by chemical vapor deposition directly on silicon nitride", *Appl. Phys. Lett.* **98**, (2011).

[86]M. H. Rümmeli et al., "Direct Low Temperature Nano-Graphene Synthesis over a Dielectric Insulator", *ACS Nano* **4**, (2010).

[87]A. Scott et al., "The catalytic potential of high-κ dielectrics for graphene formation", *Appl. Phys. Lett.* **98**, (2011).

[88]X. Ding et al., "Direct growth of few layer graphene on hexagonal boron nitride by chemical vapor deposition", *Carbon N. Y.* **49**, 2522 (2011).

[89]L. Song et al., "Large scale growth and characterization of atomic hexagonal boron nitride layers", *Nano Lett.* **10**, 3209 (2010).

[90]Y. Shi et al., "Synthesis of few-layer hexagonal boron nitride thin film by chemical vapor deposition", *Nano Lett.* **10**, 4134 (2010).

[91]C. R. Dean et al., "Boron nitride substrates for high-quality graphene electronics", *Nat. Nanotechnol.* **5**, 722 (2010).

[92]J. Hackley et al., "Graphitic carbon growth on Si(111) using solid source molecular beam epitaxy", *Appl. Phys. Lett.* **95**, 1 (2009).

[93]J. Wu, W. Pisula, and K. Müllen, "Graphenes as potential material for electronics", *Chem. Rev.* **107**, 718 (2007).

[94]Q. H. Wang and M. C. Hersam, "Room-temperature molecular-resolution characterization of self-assembled organic monolayers on epitaxial graphene", *Nat Chem* **1**, 206 (2009).

[95]S. D. Sarma et al., "Electronic transport in two dimensional graphene", *Rev. Mod. Phys.* **83**, 69 (2010).

[96]D.-H. Chae et al., "Hot phonons in an electrically biased graphene constriction", *Nano Lett.* **10**, 466 (2010).

[97]A. a Balandin et al., "Superior thermal conductivity of single-layer graphene", *Nano Lett.* **8**, 902 (2008).

[98]A. Castro Neto et al., "The electronic properties of graphene", *Rev. Mod. Phys.* **81**, 109 (2009).

[99]M. Brandbyge, "Electronic properties and applications of Carbon nanomaterials", (Danish Technical University, Copenhagen, 2010).

[100]P. Wallace, "The band theory of graphite", *Phys. Rev.* **71**, 622 (1947).

[101]J. Appenzeller, S. Datta, and M. Lundstrom, "Colloquium on Graphene Physics and Devices", (2009).

[102]K. Bolotin et al., "Temperature-dependent transport in suspended graphene", *Phys. Rev. Lett.* **101**, 96802 (2008).

[103]J. Martin et al., "Observation of electron–hole puddles in graphene using a scanning single-electron transistor", *Nat. Phys.* **4**, 144 (2007).

[104]K. Nomura and a. H. MacDonald, "Quantum Transport of Massless Dirac Fermions", *Phys. Rev. Lett.* **98**, 1 (2007).

[105]E. Hwang, S. Adam, and S. Sarma, "Carrier Transport in Two-Dimensional Graphene Layers", *Phys. Rev. Lett.* **98**, 4 (2007).

[106]J.-H. Chen et al., "Charged-impurity scattering in graphene", *Nat. Phys.* **4**, 377 (2008).

[107]S. Adam et al., "A self-consistent theory for graphene transport", *Proc. Natl. Acad. Sci. U. S. A.* **104**, 18392 (2007).

[108]M. I. Katsnelson, "Zitterbewegung, chirality, and minimal conductivity in graphene", *Eur. Phys. J. B* **51**, 157 (2006).

[109]R. S. Shishir and D. K. Ferry, "Intrinsic mobility in graphene", *J. Phys. Condens. Matter* **21**, 232204 (2009).

[110]S. Kim et al., "Realization of a high mobility dual-gated graphene field-effect transistor with Al2O3 dielectric", *Appl. Phys. Lett.* **94**, 062107 (2009).

[111]A. Naeemi and J. D. Meindl, "Conductance modeling for graphene nanoribbon (GNR) interconnects", *Electron Device Lett. IEEE* **28**, 428 (2007).

[112]I. Meric et al., "Current saturation in zero-bandgap, top-gated graphene field-effect transistors", *Nat. Nanotechnol.* **3**, 654 (2008).

[113]Y.-M. Lin et al., "Operation of graphene transistors at gigahertz frequencies", *Nano Lett.* **9**, 422 (2009).

[114]M. Lemme and T. Echtermeyer, "A graphene field-effect device", *Electron Device Lett. IEEE* **28**, 282 (2007).

[115]D. B. Farmer et al., "Utilization of a buffered dielectric to achieve high field-effect carrier mobility in graphene transistors", *Nano Lett.* **9**, 4474 (2009).

[116]L. Liao et al., "High-κ oxide nanoribbons as gate dielectrics for high mobility top-gated graphene transistors", *Proc. Natl. Acad. Sci. U. S. A.* **107**, 6711 (2010).

[117]J. S. Moon et al., "Epitaxial-graphene RF field-effect transistors on Si-face 6H-SiC substrates", *Electron Device Lett. IEEE* **30**, 650 (2009).

[118]J. Kedzierski et al., "Graphene-on-insulator transistors made using C on Ni chemical-vapor deposition", *Electron Device Lett. IEEE* **30**, 745 (2009).

[119]S. L. Li et al., ”Low operating bias and matched input-output characteristics in graphene logic inverters”, *Nano Lett.* **10**, 2357 (2010).

[120]S. L. Li et al., ”Enhanced logic performance with semiconducting bilayer graphene channels”, *ACS Nano* **5**, 500 (2011).

[121]R. Cheng et al., ”High-frequency self-aligned graphene transistors with transferred gate stacks”, *Proc. Natl. Acad. Sci. U. S. A.* **109**, 11588 (2012).

[122]A. Reina et al., ”Transferring and identification of single- and few-layer graphene on arbitrary substrates”, *J. Phys. Chem. C* **112**, 17741 (2008).

[123]L. Wang et al., ”One-dimensional electrical contact to a two-dimensional material”, *Science* **342**, 614 (2013).

[124]J. Yan and M. S. Fuhrer, ”Correlated charged impurity scattering in graphene”, *Phys. Rev. Lett.* **107**, 206601 (2011).

[125]M. Lafkioti et al., ”Graphene on a hydrophobic substrate: doping reduction and hysteresis suppression under ambient conditions”, *Nano Lett.* **10**, 1149 (2010).

[126]U. of Leeds, ”Condensed Matter Physics group”, (n.d.).

[127]C. S. Wu, Y. Makiuchi, and C. Chen, in *Lithography*, edited by M. Wang (2010).

[128]J. Cai et al., ”Atomically precise bottom-up fabrication of graphene nanoribbons”, *Nature* **466**, 470 (2010).

[129]J. Hicks et al., ”A wide-bandgap metal–semiconductor–metal nanostructure made entirely from graphene”, *Nat. Phys.* **8**, 1 (2012).

[130]J. Alden, ”McEuen research group - wiki”, (2008).

[131]S. H. Gage, ”Modern dark-field microscopy and the history of its development”, *Trans. Am. Microsc. Soc.* **39**, 95 (1920).

[132]D. Misell and C. Stolinski, ”Scanning electron microscopy and X-ray microanalysis A text for biologists, material scientists and geologists”, (Plenum Publishing Corporation, 1983), p. 293.

[133]M. Amman et al., ”Atomic force microscopy study of electron beam written contamination structures”, *J. Vac. Sci. Technol. B Microelectron. Nanom. Struct.* **14**, 54 (1996).

[134]P. F. Bernath, ”Spectra of Atoms and Molecules”, (Oxford University Press, 2005).

[135]a. C. Ferrari et al., ”Raman Spectrum of Graphene and Graphene Layers”, *Phys. Rev. Lett.* **97**, 1 (2006).

[136]F. Tuinstra and L. Koenig, ”Raman Spectrum of Graphite”, *J. Chem. Phys.* **53**, 1126 (1970).

[137]R. J. Nemanich and S. a Solin, ”First- and second-order Raman Scattering from finite-sized crystals of graphite”, *Phys. Rev. B - Condens. Matter Mater. Phys.* **20**, 392 (1979).

[138]R. Vidano et al., ”Observation of Raman band shifting with excitation wavelength for carbons and graphites”, *Solid State Commun.* **39**, 341 (1981).

[139]C. Casiraghi et al., ”Raman fingerprint of charged impurities in graphene”, *Appl. Phys. Lett.* **91**, 10 (2007).

[140]A. Das et al., ”Monitoring dopants by Raman scattering in an electrochemically top-gated graphene transistor”, *Nat. Nanotechnol.* **3**, 210 (2008).

[141]Y.-C. Lin et al., ”Graphene annealing: How clean can it be?”, *Nano Lett.* (2011).

[142]a C. F. Hoole, M. E. Welland, and a N. Broers, ”Negative PMMA as a high-resolution resist - the limits and possibilities”, *Semicond. Sci. Technol.* **12**, 1166 (1999).

[143]R. Manual and R. B. June, ”Model 6220 DC Current Source Model 6221 AC and DC Current Source User ’ s Manual”, Second Pri (Keithley Instruments, Inc., Cleveland, Ohio, U.S.A., 2005).

[144]N. F. Mott, ”The Electrical Conductivity of Transition Metals”, *Proc. R. Soc. A Math. Phys. Eng. Sci.* **153**, 699 (1936).

[145]T. Valet and A. Fert, ”Theory of the perpendicular magnetoresistance in magnetic multilayers”, *Phys. Rev. B - Condens. Matter Mater. Phys.* **48**, (1993).

[146]J. Bass and W. P. Pratt, ”Spin-diffusion lengths in metals and alloys, and spin-flipping at metal/metal interfaces: an experimentalist’s critical review”, *J. Phys. Condens. Matter* **19**, 183201 (2007).

[147]T. Maassen, Electron Spin Transport in Graphene-based Devices, PhD thesis, University of Groningen, 2013.

[148]a. Fert and H. Jaffrès, ”Conditions for efficient spin injection from a ferromagnetic metal into a semiconductor”, *Phys. Rev. B - Condens. Matter Mater. Phys.* **64**, 184420 (2001).

[149]F. J. Jedema et al., ”Electrical detection of spin precession in a metallic mesoscopic spin valve”, *Nature* **416**, 713 (2002).

[150]E. I. Rashba, ”Theory of electrical spin injection: Tunnel contacts as a solution of the conductivity mismatch problem”, *Phys. Rev. B - Condens. Matter Mater. Phys.* **62**, 267 (2000).

[151]G. Schmidt et al., ”Fundamental obstacle for electrical spin injection from a ferromagnetic metal into a diffusive semiconductor”, *Phys. Rev. B - Condens. Matter Mater. Phys.* **62**, (2000).

[152]M. Popinciuc et al., ”Electronic spin transport in graphene field-effect transistors”, *Phys. Rev. B - Condens. Matter Mater. Phys.* **80**, 1 (2009).

[153]Q. Wu et al., ”Efficient Spin Injection into Graphene through a Tunnel Barrier: Overcoming the Spin-Conductance Mismatch”, *Phys. Rev. Appl.* **2**, 044008 (2014).

[154]S. Dubois et al., ”Evidence for a short spin diffusion length in permalloy from the giant magnetoresistance of multilayered nanowires”, *Phys. Rev. B - Condens. Matter Mater. Phys.* **60**, 477 (1999).

[155]R. Elliott, ”Theory of the effect of spin-orbit coupling on magnetic resonance in some semiconductors”, **689**, (1954).

[156]Y. Yafet, ”g Factors and Spin-Lattice Relaxation of Conduction Electrons”, *Solid State Phys. - Adv. Res. Appl.* **14**, 1 (1963).

[157]M. I. Dyakonov and V. I. Perel, ”Spin relaxation of conduction electrons in noncentrosymmetric semiconductors”, *Sov. Phys. Solid State* **13**, 3023 (1971).

[158]E. Y. Tsymbal and I. Zutic, ”Handbook of spin transport and magnetism”, (CRC press, 2011).

[159]N. Tombros et al., ”Electronic spin transport and spin precession in single graphene layers at room temperature”, *Nature* **448**, 571 (2007).

[160]F. Jedema et al., ”Spin Injection and Spin Accumulation in Permalloy–Copper Mesoscopic Spin Valves”, *J. Supercond. Inc. Nov. Magn.* **15**, 27 (2002).

[161]S. Takahashi and S. Maekawa, ”Spin Injection and Detection in Magnetic Nanostructures”, *Phys. Rev. B - Condens. Matter Mater. Phys.* **67**, 4 (2003).

[162]T. Maassen et al., ”Contact-induced spin relaxation in Hanle spin precession measurements”, *Phys. Rev. B - Condens. Matter Mater. Phys.* **86**, 235408 (2012).

[163]H. Idzuchi et al., ”Effect of anisotropic spin absorption on the Hanle effect in lateral spin valves”, *Phys. Rev. B - Condens. Matter Mater. Phys.* **89**, 081308 (2014).

[164]M. Wojtaszek, I. J. Vera-Marun, and B. J. van Wees, ”Transition between one-dimensional and zero-dimensional spin transport studied by Hanle precession”, *Phys. Rev. B - Condens. Matter Mater. Phys.* **89**, 245427 (2014).

[165]E. Hill et al., ”Graphene spin valve devices”, *Magn. IEEE Trans.* **42**, 2694 (2006).

[166]H. Idzuchi, Y. Fukuma, and Y. Otani, ”Spin transport in non-magnetic nanostructures induced by non-local spin injection”, *Phys. E Low-Dimensional Syst. Nanostructures* **68**, 239 (2015).

[167]B. Dlubak, Transport dépendant du spin dans le graphène, PhD thesis, Universite Paris-Sud, 2011.

[168]M. Ohishi et al., ”Spin Injection into a Graphene Thin Film at Room Temperature”, *Jpn. J. Appl. Phys.* **46**, (2007).

[169]M. Nishioka and A. M. Goldman, ”Spin transport through multilayer graphene”, *Appl. Phys. Lett.* **90**, (2007).

[170]S. Cho, Y.-F. Chen, and M. S. Fuhrer, ”Gate-tunable graphene spin valve”, *Appl. Phys. Lett.* **91**, 123105 (2007).

[171]W. H. Wang et al., ”Magnetotransport properties of mesoscopic graphite spin valves”, *Phys. Rev. B - Condens. Matter Mater. Phys.* **77**, 20402 (2008).

[172]H. Goto et al., ”Gate control of spin transport in multilayer graphene”, *Appl. Phys. Lett.* **92**, 212110 (2008).

[173]A. Avsar et al., ”Toward wafer scale fabrication of graphene based spin valve devices”, *Nano Lett.* **11**, 2363 (2011).

[174]I. Neumann et al., ”Electrical detection of spin precession in freely suspended graphene spin valves on cross-linked poly(methyl methacrylate)”, *Small* **9**, 156 (2013).

[175]A. G. Swartz et al., "Integrating MBE materials with graphene to induce novel spin-based phenomena", *J. Vac. Sci. Technol. B Microelectron. Nanom. Struct.* **31**, 17 (2013).

[176]W. Han et al., "Spin Relaxation in Single Layer Graphene with Tunable Mobility", *Nano Lett.* **12**, 3443 (2012).

[177]M. V. Kamalakar et al., "Enhanced Tunnel Spin Injection into Graphene using Chemical Vapor Deposited Hexagonal Boron Nitride", *Sci. Rep.* **4**, 1 (2014).

[178]P. J. Zomer et al., "Long Distance Spin Transport in High Mobility Graphene on Hexagonal Boron Nitride", *Phys. Rev. B - Condens. Matter Mater. Phys.* **86**, 1 (2012).

[179]M. H. D. Guimarães et al., "Spin Transport in High-Quality Suspended Graphene Devices", *Nano Lett.* **12**, 3512 (2012).

[180]T. Yamaguchi et al., "Spin Relaxation in Weak Localization Regime in Multilayer Graphene Spin Valves", *Jpn. J. Appl. Phys.* **52**, 1 (2013).

[181]B. Dlubak et al., "Highly efficient spin transport in epitaxial graphene on SiC", *Nat. Phys.* **8**, 1 (2012).

[182]T. Maassen et al., "Long Spin Relaxation Times in Wafer Scale Epitaxial Graphene on SiC(0001)", *Nano Lett.* **2**, 5 (2012).

[183]Y. Lu et al., "High-on/off-ratio graphene nanoconstriction field-effect transistor", *Small* **6**, 2748 (2010).

[184]N. Tombros et al., "Large yield production of high mobility freely suspended graphene electronic devices on a polydimethylglutarimide based organic polymer", *J. Appl. Phys.* **109**, 093702 (2011).

[185]E. R. Mucciolo, A. H. C. Neto, and C. H. Lewenkopf, "Conductance quantization and transport gaps in disordered graphene nanoribbons", *Phys. Rev. B - Condens. Matter Mater. Phys.* **79**, 75407 (2009).

[186]A. Lherbier et al., "Transport length scales in disordered graphene-based materials: strong localization regimes and dimensionality effects", *Phys. Rev. Lett.* **100**, 36803 (2008).

[187]E. Villamor, Injection , transport and manipulation of pure spin currents in metallic lateral spin valves, PhD thesis, 2014.

[188]T. Yamaguchi et al., "Tunnel spin injection into graphene using Al2O3 barrier grown by atomic layer deposition on functionalized graphene surface", *J.*

Magn. Magn. Mater. **324**, 849 (2012).

[189]W. Han et al., "Tunneling spin injection into single layer graphene", *Phys. Rev. Lett.* **105**, (2010).

[190]Y. P. Liu et al., "Spin injection properties in trilayer graphene lateral spin valves", *Appl. Phys. Lett.* **102**, 2013 (2013).

[191]I. Neumann et al., "Enhanced spin accumulation at room temperature in graphene spin valves with amorphous carbon interfacial layers", *Appl. Phys. Lett.* **103**, 112401 (2013).

[192]A. Dankert et al., "Spin transport and precession in graphene measured by nonlocal and three-terminal methods", *Appl. Phys. Lett.* **104**, 4 (2014).

[193]N. Tombros, Electron spin transport in graphene and carbon nanotubes, PhD thesis, University of Groningen, 2008.

[194]X. Wang, S. Tabakman, and H. Dai, "Atomic Layer Deposition of Metal Oxides on Pristine and Functionalized Graphene", *J. Am. Chem. Soc.* 8152 (2008).

[195]K. Zou et al., "Deposition of High-Quality HfO_{2} on Graphene and the Effect of Remote Oxide Phonon Scattering", *Phys. Rev. Lett.* **105**, 126601 (2010).

[196]E. Villamor et al., "Modulation of pure spin currents with a ferromagnetic insulator", *Phys. Rev. B* **91**, 020403 (2015).

[197]M. Erekhinsky et al., "Spin-dependent Seebeck effect in non-local spin valve devices", *Appl. Phys. Lett.* **100**, (2012).

[198]M. Erekhinsky et al., "Surface enhanced spin-flip scattering in lateral spin valves", *Appl. Phys. Lett.* **96**, (2010).

[199]M. Isasa et al., "Temperature dependence of spin diffusion length and spin Hall angle in Au and Pt", *Phys. Rev. B - Condens. Matter Mater. Phys.* **91**, 24402 (2015).

[200]E. Villamor et al., "Temperature dependence of spin polarization in ferromagnetic metals using lateral spin valves", *Phys. Rev. B - Condens. Matter Mater. Phys.* **88**, 184411 (2013).

[201]Y.-W. Son, M. L. Cohen, and S. G. Louie, "Half-metallic graphene nanoribbons", *Nature* **444**, 347 (2006).

[202]G. Han et al., "Influence of Copper Morphology in Forming Nucleation Seeds for Graphene Growth", *Nano Lett.* (2011).

[203]E. Villamor et al., "Contribution of defects to the spin relaxation in copper nanowires", *Phys. Rev. B - Condens. Matter Mater. Phys.* **87**, 94417 (2013).

[204]S. O. Valenzuela et al., "Spin Polarized Tunneling at Finite Bias", *Phys. Rev. Lett.* **94**, 196601 (2005).

[205]F. J. Jedema, A. T. Filip, and B. J. van Wees, "Electrical spin injection and accumulation at room temperature in an all-metal mesoscopic spin valve", *Nature* **410**, 345 (2001).

[206]Q. Yang et al., "Spin flip diffusion length and giant magnetoresistance at low temperatures", *Phys. Rev. Lett.* **72**, 3274 (1994).

[207]G. Mihajlović et al., "Surface Spin Flip Probability of Mesoscopic Ag Wires", *Phys. Rev. Lett.* **104**, 237202 (2010).

[208]H. Idzuchi et al., "Spin relaxation mechanism in silver nanowires covered with MgO protection layer", *Appl. Phys. Lett.* **101**, (2012).

[209]A. Van Staa et al., "Spin precession in lateral all-metal spin valves: Experimental observation and theoretical description", *Phys. Rev. B - Condens. Matter Mater. Phys.* **77**, 1 (2008).

[210]M. Johnson and R. H. Silsbee, "Interfacial charge-spin coupling: Injection and detection of spin magnetization in metals", *Phys. Rev. Lett.* **55**, 1790 (1985).

[211]J. Balakrishnan et al., "Giant spin Hall effect in graphene grown by chemical vapour deposition", *Nat. Commun.* **5**, 4748 (2014).

[212]B. Trauzettel et al., "Spin qubits in graphene quantum dots", *Nat. Phys.* **3**, 192 (2007).

[213]S. Singh et al., "Spin pumping in permalloy/graphene and permalloy/graphite interfaces", *IEEE Trans. Magn.* **49**, 3147 (2013).

[214]Z. Tang et al., "Dynamically generated pure spin current in single-layer graphene", *Phys. Rev. B - Condens. Matter Mater. Phys.* **87**, 1 (2013).

[215]W. J. Kaiser and L. D. Bell, "Direct investigation of subsurface interface electronic structure by ballistic-electron-emission microscopy", *Phys. Rev. Lett.* **60**, 1406 (1988).

[216]L. D. Bell and W. J. Kaiser, "Observation of Interface Band Structure by Ballistic-Electron-Emission Microscopy", *Phys. Rev. Lett.* **61**, 2368 (1988).

[217]C. R. Crowell et al., "Attenuation length measurements of hot electrons in metal films", *Phys. Rev.* **127**, 2006 (1962).

[218]J. Hwang, A. Wan, and A. Kahn, "Energetics of metal-organic interfaces: New experiments and assessment of the field", *Mater. Sci. Eng. R Reports* **64**, 1 (2009).

[219]S. Braun, W. R. Salaneck, and M. Fahlman, "Energy-level alignment at organic/metal and organic/organic interfaces", *Adv. Mater.* **21**, 1450 (2009).

[220]C. Troadec, L. Kunardi, and N. Chandrasekhar, "Ballistic emission spectroscopy and imaging of a buried metalorganic interface", *Appl. Phys. Lett.* **86**, 1 (2005).

[221]W. Li et al., "Ballistic electron emission microscopy studies of Au/molecule/n-GaAs diodes", *J. Phys. Chem. B* **109**, 6252 (2005).

[222]I. Appelbaum, B. Huang, and D. J. Monsma, "Electronic measurement and control of spin transport in silicon", *Nature* **447**, 295 (2007).

[223]B. Huang, D. Monsma, and I. Appelbaum, "Coherent Spin Transport through a 350 Micron Thick Silicon Wafer", *Phys. Rev. Lett.* **99**, 1 (2007).

[224]S. Vaziri et al., "A graphene-based hot electron transistor", *Nano Lett.* **13**, 1435 (2013).

[225]C. Zeng et al., "Vertical graphene-base hot-electron transistor", *Nano Lett.* **13**, 2370 (2013).

[226]M. Gobbi et al., "Determination of energy level alignment at metal/molecule interfaces by in-device electrical spectroscopy", *Nat. Commun.* **5**, 4161 (2014).

[227]H. Bruus and K. Flensberg, "Introduction to Many-body quantum theory in condensed matter physics", *Physics (College. Park. Md).* **38**, 1829 (2002).

[228]J. G. Simmons, "Generalized Formula for the Electric Tunnel Effect between Similar Electrodes Separated by a Thin Insulating Film", *J. Appl. Phys.* **34**, 1793 (1963).

[229]M. Baldo and S. Forrest, "Interface-limited injection in amorphous organic semiconductors", *Phys. Rev. B - Condens. Matter Mater. Phys.* **64**, 1 (2001).

[230]R. G. Parr and R. G. Pearson, "Absolute hardness: companion parameter to absolute electronegativity", *J. Am. Chem. Soc.* **105**, 7512 (1983).

[231]X. Crispin et al., "Characterization of the interface dipole at organic/ metal interfaces", *J. Am. Chem. Soc.* **124**, 8131 (2002).

[232]S. van Dijken, X. Jiang, and S. S. P. Parkin, "Nonmonotonic bias voltage dependence of the magnetocurrent in GaAs-based magnetic tunnel transistors", *Phys. Rev. Lett.* **90**, 197203 (2003).

[233]S. Parui et al., "Gate-Controlled Energy Barrier at a Graphene/Molecular Semiconductor Junction", *Adv. Funct. Mater.* (2015).

[234]H. Haugen, D. Huertas-Hernando, and A. Brataas, "Spin transport in proximity-induced ferromagnetic graphene", *Phys. Rev. B - Condens. Matter Mater. Phys.* **77**, 115406 (2008).

[235]H. Yang et al., "Proximity Effects Induced in Graphene by Magnetic Insulators: First-Principles Calculations on Spin Filtering and Exchange-Splitting Gaps", *Phys. Rev. Lett.* **110**, 046603 (2013).

[236]Z. Wang et al., "Proximity-Induced Ferromagnetism in Graphene Revealed by the Anomalous Hall Effect", *Phys. Rev. Lett.* **114**, 016603 (2015).

[237]T. Yokoyama, "Controllable spin transport in ferromagnetic graphene junctions", *Phys. Rev. B - Condens. Matter Mater. Phys.* **77**, 7 (2008).

[238]T. Yokoyama and J. Linder, "Anomalous magnetic transport in ferromagnetic graphene junctions", *Phys. Rev. B - Condens. Matter Mater. Phys.* **83**, 81418 (2011).

[239]P. Michetti, P. Recher, and G. Iannaccone, "Electric field control of spin rotation in bilayer graphene", *Nano Lett.* **10**, 4463 (2010).

[240]C. Harmans and F. der T. N. TU Delft, "Mesoscopic Physics: An Introduction : TN385 [dictaat Behorende Bij College TN3853]", (TU Delft, 2003).

[241]C. B. Craus, Magnetic properties of nanocrystalline materials for high frequency applications - Chapter 6, PhD thesis, University of Groningen, 2003.

[242]A. Gurevich and G. Melkov, "Magnetization oscillations and waves", (1996), p. 464.

[243]W. X. Xia et al., "Investigation of magnetic structure and magnetization process of yttrium iron garnet film by Lorentz microscopy and electron holography", *J. Appl. Phys.* **108**, 123919 (2010).

[244]S. B. Ubizskii, ”Orientational states of magnetization in epitaxial (111)-oriented iron garnet films”, *J. Magn. Magn. Mater.* **195**, 575 (1999).

[245]S. B. Ubizskii, ”Magnetization reversal modelling for (1 1 1)-oriented epitaxial films of iron garnets with mixed anisotropy”, *J. Magn. Magn. Mater.* **219**, 127 (2000).

[246]M. Lang et al., ”Proximity Induced High-Temperature Magnetic Order in Topological Insulator - Ferrimagnetic Insulator Heterostructure”, *Nano Lett.* **14**, 3459 (2014).

[247]F. V. Tikhonenko et al., ”Weak Localization in Graphene Flakes”, *Phys. Rev. Lett.* **100**, 056802 (2008).

[248]J. Han et al., ”Room-temperature observations of the weak localization in low-mobility graphene films”, *J. Appl. Phys.* **114**, 214502 (2013).

[249]E. McCann et al., ”Weak-Localization Magnetoresistance and Valley Symmetry in Graphene”, *Phys. Rev. Lett.* **97**, 146805 (2006).

[250]H. J. G. Draaisma and W. J. M. de Jonge, ”Magnetization curves of Pd/Co multilayers with perpendicular anisotropy”, *J. Appl. Phys.* **62**, 3318 (1987).

[251]F. V. Tikhonenko et al., ”Transition between Electron Localization and Antilocalization in Graphene”, *Phys. Rev. Lett.* **103**, 226801 (2009).

[252]J. Lindemuth and B. Dodrill, ”Measurement of the magnetic properties of double-layered PMRM using an AHE magnetometer”, *IEEE Trans. Magn.* **40**, 2191 (2004).

[253]M. Guyot and A. Globus, ”Determination of the Domain Wall Energy and the Exchange Constant From Hysteresis in Ferrimagnetic Polycrystals”, *Le J. Phys. Colloq.* **38**, 157 (1977).